6

Transport Properties

S. Roche, E. Akkermans, O. Chauvet, F. Hekking, J.-P. Issi, R. Martel, G. Montambaux and Ph. Poncharal

Abstract. In this chapter, we first review the fundamental theoretical concepts of mesoscopic transport for low-dimensional systems and disordered materials. Emphasis is put on the Landauer formulation of electronic transmission, weak localization and Aharonov-Bohm phenomena, as well as Coulomb interactions through screening effects and Luttinger liquid model. A pedagogical effort is made to present the currently established physics of quantum conduction in some analytical detail, enabling the reader to further deepen the understanding of more specialized literature. In a subsequent part, the main theoretical features of quantum transport in carbon nanotubes are elaborated, mostly within the non-interacting electron regime, that is to date less controversial. The experimental part starts with a discussion of the commonly employed measurement techniques. Several transport experiments are then analyzed, with a particular focus on device-oriented aspects (field effect, Schottky barriers, etc). Finally, the main physical properties of nanotube-based composites are outlined, followed by a presentation of our current understanding of thermal properties of carbon tubules.

6.1 Quantum Transport in Low-dimensional Materials

6.1.1 Ballistic Conduction and Quantized Conductance

Drude-Sommerfeld Theory of Metals

Conductivity and Conductance

In ordinary metals, transport is conveniently described using Drude-Sommerfeld theory [1]. In this theory, the conduction electrons (mass m, charge $-e$) form a degenerate Fermi gas (Fermi energy E_F). Momentum relaxation occurs with a rate $1/\tau$, where τ is the *mean time* between successive scattering events. The mean free path ℓ_e is the average distance over which electrons propagate *ballistically*, i.e., without being scattered. It is given by $\ell_e = v_F\tau$, where $v_F = \sqrt{2E_F/m}$ is the Fermi velocity.

S. Roche et al.: *Transport Properties*, Lect. Notes Phys. **677**, 335–437 (2006)
www.springerlink.com

In metals, the mean free path is usually long compared to the Fermi wavelength $\lambda_F = 2\pi\hbar/(mv_F)$. Hence the electron motion is quasi-classical on the scale ℓ_e and can be described by Newton's laws. In particular, an applied electric field $\boldsymbol{E}$ will accelerate the electrons up to a time τ. Beyond this time, scattering events completely randomize the electron momentum and destroy all (quantum-mechanical) correlations. This is the central assumption of the Drude-Sommerfeld theory. As a result the acquired momentum is on average $\boldsymbol{p} = m\boldsymbol{v} = -e\boldsymbol{E}\tau$. Introducing the current density $\boldsymbol{j} = -n_0 e\boldsymbol{v}$, where n_0 is the electron density, we immediately obtain Ohm's law $\boldsymbol{j} = \sigma_D \boldsymbol{E}$ where

$$\sigma_D = \frac{n_0 e^2 \tau}{m} \tag{6.1}$$

is the Drude conductivity. Equation (6.1) constitutes a local relation between $\boldsymbol{j}$ and $\boldsymbol{E}$: the current density at position $\boldsymbol{r}$ is determined by the value of $\boldsymbol{E}$ at the same position $\boldsymbol{r}$.

The Drude conductivity is a material parameter: it does not depend on the geometry of the sample. Often we write Ohm's law as $I = \mathcal{G}V$, where I is the total current, V the applied voltage, and $\mathcal{G}$ the conductance. This is a non-local relation: the total current I through the sample is determined by the voltage difference applied to the sample boundaries. For a wire of length L and cross-section S, we have $\mathcal{G} = \sigma_D S/L$. This implies that the resistance $R = 1/\mathcal{G}$ scales linearly with L, and is inversely proportional to S, in agreement with the usual rules for series and parallel addition of resistances, respectively.

Momentum Relaxation; Residual Conductivity

Momentum relaxation occurs due to the fact that the electrons undergo scattering events [2]. The most important mechanisms contributing to momentum relaxation are electron-phonon scattering, electron-electron scattering and scattering off static impurities. The first two mechanisms are inelastic: they involve a change in both energy and momentum. Scattering off static impurities is purely elastic: only the direction of the momentum changes.

At room temperature, inelastic phonon scattering dominates. The energy acquired by the electron during the acceleration in an electric field is dissipated during collisions to the phonons, leading to heating of the sample. As the temperature T is lowered, phonons become less effective; the mean free time and hence the conductivity rapidly grow, $\sigma_D \sim 1/T^5$. The temperature dependence changes at low temperatures, where in principle inelastic electron-electron collisions dominate (although this is often masked by impurity scattering). According to Fermi liquid theory (see Sect. 6.1.2 below), $\tau \sim 1/T^2$ such that the conductivity increases more slowly with decreasing temperature, $\sigma_D \sim 1/T^2$.

The inelastic scattering time τ diverges as $T \to 0$. Nevertheless, at the lowest temperatures, the conductivity approaches a constant value $\sigma_D = \sigma_0 = n_0 e^2 \tau_e/m$. This is the so-called residual conductivity of the metal, and it is

due to elastic scattering off static impurities. The elastic mean free time τ_e defines the elastic mean free path $\ell_e = v_F \tau_e$. On length scales larger than ℓ_e, the electron motion is *diffusive*, with a diffusion coefficient $D = v_F \ell_e / d$, where d is the dimension of the sample. Inelastic scattering still occurs, but on longer time scales $\tau \gg \tau_e$. The associated inelastic length is then defined by the diffusive result $L_{in} = \sqrt{D\tau} \gg \ell_e$. As we have seen above, at the lowest temperatures, this length is determined by electron-electron scattering events.

Mesoscopic Phenomena in Metals

In a mesoscopic sample [3,4], i.e. a sample whose characteristic size L is large compared to the elastic mean free path ℓ_e, but small compared to the inelastic length L_{in}, electrons undergo elastic scattering only. The central assumption of the Drude-Sommerfeld theory, stating that quantum correlations are lost as a a result of scattering, becomes clearly questionable in this limit. In fact, as long as the scattering is elastic, the electron phase memory is conserved and the electron motion should be described quasi-classically on length scales up to L_{in}. For a mesoscopic sample this means in particular that the electron follows classical trajectories through the entire sample, supplemented with a quantum mechanical phase. As a result, quantum-interference phenomena can occur involving two or more trajectories with different phases. These interference phenomena lead to corrections to transport properties; examples are the weak-localization correction to the conductivity, the occurrence of Aharonov-Bohm oscillations in small metallic rings and the universal sample-to-sample fluctuations of the conductance.

In what follows, we will discuss a general approach, based on ideas due to Landauer, that enables one to formulate the problem of phase-coherent transport. We will express the conductance of a phase-coherent sample in terms of its quantum-mechanical transmission properties [3,4]. This approach can then be used to obtain the conductance in specific cases of interest. We will see that conductance in the quantum limit obeys rules that are very different from those known from Drude-Sommerfeld theory. The Landauer approach also provides answers to important additional questions. For instance, if there is elastic scattering only in the sample, one may ask where the dissipation arises. We will also see what happens in clean phase-coherent samples with $L < \ell_e, L_{in}$. It turns out that even these ballistic conductors are still characterized by a finite resistance. In Sect. 6.2, quantum-interference phenomena will be analyzed in more details by means of an analytical description.

The Scattering Approach to Quantum Transport

Multi-Mode Quantum Wire

In order to set the stage, we start our discussion by considering a two-dimensional quantum wire of width W (Fig. 6.1) in the ballistic conduction

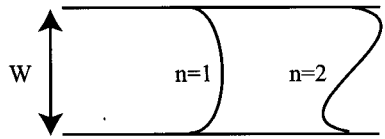

Fig. 6.1. Clean quantum wire of width W with two propagating modes

regime. Electrons in such a wire obey the two-dimensional Schrödinger equation

$$\left[-\frac{\hbar^2}{2m}\left(\frac{\partial^2}{\partial x^2}+\frac{\partial^2}{\partial y^2}\right)+U(x,y)\right]\Psi(x,y)=E\Psi(x,y) \tag{6.2}$$

Here $U(x,y)$ is the potential confining the electrons to the wire. Supposing free propagation in x-direction and an infinite square well confining potential in y-direction, we can write the solution

$$\Psi(x,y)=\Psi_{nk}(x,y)=\mathrm{e}^{\mathrm{i}kx}\chi_n(y) \tag{6.3}$$

where $\chi_n(y)=\sqrt{2/W}\sin[n\pi(y+W/2)/W]$ with $n=1,2,3,\ldots$ These wave functions vanish at the edges of the wire, i.e. for $y=\pm W/2$. The dispersion of these electrons is $E=E_n(k)=\hbar^2k^2/2m+\epsilon_n$, where $\epsilon_n=\hbar^2n^2\pi^2/(2mW^2)$ is the discrete spectrum due to confinement in the y-direction. From this we see: for a given energy $E<\epsilon_1$, k is purely imaginary and no propagating modes are available in the wire. For $\epsilon_1<E<\epsilon_2$, we find one propagating mode, corresponding to $n=1$; generally speaking, for $\epsilon_N<E<\epsilon_{N+1}$, N propagating modes are found.

The group velocity of an electron in a given mode is obtained from the energy dispersion in the usual way,

$$v_{n,\pm}(E)=\pm v_n(E)\equiv\pm\frac{1}{\hbar}\left.\frac{\mathrm{d}E_n(k)}{\mathrm{d}k}\right|_E=\pm\sqrt{2(E-\epsilon_n)/m} \tag{6.4}$$

Here + (−) refers to a right-moving (left-moving) electron, respectively. The *density of states* per unit length (for one spin direction) for a given mode and a given direction of propagation is

$$\rho_n(E)=\frac{1}{2\pi}\left.\frac{1}{\mathrm{d}E_{nk}/\mathrm{d}k}\right|_E=\frac{1}{2\pi\hbar v_n(E)} \tag{6.5}$$

This means in particular that the product $\rho_n(E)v_n(E)=1/(2\pi\hbar)$ is a constant. The electric current (per unit energy), carried by a given mode n in a given direction at energy E is then given by

$$I_{n,\pm}(E)=-e\rho_n(E)v_{n,\pm}(E)=\mp e/(2\pi\hbar) \tag{6.6}$$

independent of energy E and mode index n. This equipartition rule is due to the cancellation of the one-dimensional density of states and group velocity.

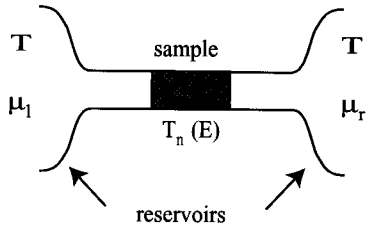

Fig. 6.2. Generic two-terminal set-up

Landauer Formula

We now formulate the quantum transport problem using the generic set-up depicted in Fig. 6.2 for a typical two-terminal transport measurement.

We distinguish three parts:

1. *Reservoirs.* The two terminals or reservoirs are the electron source and drain. They are massive electrodes at thermodynamic equilibrium, kept at temperature T and electro-chemical potential μ_i ($i = l, r$ refers to the left and right reservoir, respectively). The electrons that are injected into the sample from a reservoir i are distributed over energy E according to the Fermi-function
$$f_i(E) = \frac{1}{e^{\beta(E-\mu_i)} + 1} \tag{6.7}$$
where $\beta = 1/k_B T$ is the inverse temperature. The reservoirs absorb all incoming electrons, regardless of their energy. For a given reservoir, there is no correlation between absorbed and subsequently re-injected electrons.
2. *Perfect leads.* Between the reservoirs and the sample, electrons propagate along perfect leads, which are multi-mode quantum wires.
3. *Sample.* The sample contains only elastic scattering. It transmits an incoming electron with energy E in mode n of one of the perfect leads with quantum-mechanical transmission amplitude $t_{n,n'}(E)$ into mode n' of the other perfect lead (at the same energy E). The corresponding transmission probability is $T_{n,n'}(E) = |t_{n,n'}(E)|^2$. As a result, the total probability that an incoming mode n is transmitted is given by $T_n(E) = \sum_{n'} T_{n,n'}(E)$.

In view of the above, the total current from left to right can be written as

$$I_{\ell r} = 2 \int \mathrm{d}E \sum_n f_\ell(E) I_{n,+}(E) T_n(E) \tag{6.8}$$

and similarly for $I_{r\ell}$. Here, a factor 2 is included to account for the electron spin. As a result, the total current can be written as $I = I_{\ell r} - I_{r\ell}$,

$$I = -\frac{e}{\pi\hbar} \int \mathrm{d}E \sum_n [f_\ell(E) - f_r(E)] T_n(E) \tag{6.9}$$

We write $\mu_\ell = E_F + eV/2$ and $\mu_r = E_F - eV/2$, where eV is the bias voltage applied between the two terminals. Assuming eV is small, we can expand the Fermi functions and obtain, in the low-temperature limit,

$$I = \frac{e^2}{\pi\hbar} V \sum_n T_n(E_F) = \mathcal{G}V \tag{6.10}$$

where the conductance $\mathcal{G}$ is given by

$$\mathcal{G} = \frac{e^2}{\pi\hbar} \sum_n T_n(E_F) \tag{6.11}$$

This is the well-known Landauer formula that relates the conductance of a sample to its elastic quantum mechanical transmission probability. Some implications of this important result in various examples will be presented in the next section.

Quantum Resistance Properties

Conductance of a Multi-Mode Quantum Wire

We start our discussion of quantum resistance properties by considering a multi-mode quantum wire of width W, connected to two reservoirs with $\mu_\ell = E_F + eV/2$ and $\mu_r = E_F - eV/2$. Let $E_N < E_F < E_{N+1}$ such that there are N propagating modes at the Fermi energy E_F. Since there is no obstacle in the channel, $T_n(E_F) = 1$ for $n \leq N$. For $n > N$, there are no propagating modes, $T_n(E_F) = 0$. Therefore, at small bias,

$$I = \frac{e^2}{\pi\hbar} V \sum_n T_n(E_F) = \frac{Ne^2}{\pi\hbar} V \tag{6.12}$$

and $\mathcal{G} = Ne^2/\pi\hbar$. A few remarks are in order here:

1. Each mode contributes an amount $e^2V/(\pi\hbar)$ to the current: this is a direct consequence of the aforementioned equipartition rule.
2. The total conductance is $Ne^2/(\pi\hbar)$, i.e. $e^2/(2\pi\hbar)$ per mode and per spin direction. This so-called unitary conductance is usually referred to as the *conductance quantum* $\mathcal{G}_K = e^2/(2\pi\hbar) = e^2/h$. We see that even a perfectly transmitted mode is characterized by a finite conductance.
3. The total conductance of the quantum wire is independent of the length L of the wire. Thus the classical result $\mathcal{G} \propto 1/L$, implying the usual rules for series addition of resistances, is violated for a quantum conductor.

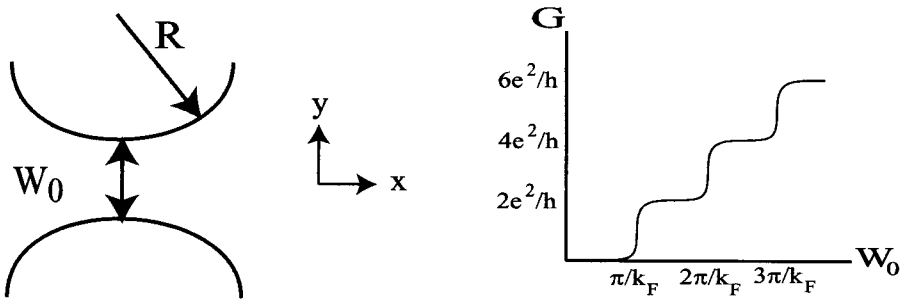

Fig. 6.3. *Left*: Quantum point contact. *Right*: Conductance quantization as a function of W_0

Conductance of an Adiabatic Quantum Point Contact

We next turn our attention to the set-up shown in Fig. 6.3. A narrow, two-dimensional constriction or quantum point contact of width W_0 at the narrowest point is defined in a two-dimensional electron gas (2DEG). We are interested in the behavior of the conductance of the constriction as a function of W_0.

We assume that the width $W(x)$ of the constriction varies slowly with x, on a scale $R \gg W_0$. Furthermore the constriction is narrow: at most a few propagating modes are present, meaning that $W_0 \sim \lambda_F$. This implies that the electron motion along the x-direction can be treated quasi-classically and scattering between modes can be neglected. We are thus faced with a number of independent modes, each obeying the one-dimensional, effective Schrödinger equation

$$\left(-\frac{\hbar^2}{2m}\frac{\mathrm{d}^2}{\mathrm{d}x^2} + U_n(x)\right)\psi_n(x) = E\psi_n(x) \tag{6.13}$$

where $U_n(x) = \epsilon_n(x)$ is a slowly varying potential: the discrete spectrum due to confinement in the y-direction $\epsilon_n(x) = \hbar^2 n^2 \pi^2/(2mW(x)^2)$ is x-dependent due to the slow variation of the width $W(x)$ along the channel. Whether or not a given mode n is transmitted depends on the position of the Fermi energy with respect to the maximum of $U_n(x)$, reached at $x = 0$ where $W(x = 0) = W_0$. For $W_0 = 0$, this maximum exceeds E_F for any n: all modes are reflected. Increasing W_0 from zero, we gradually lower the energy $U_n(0)$. When W_0 approaches the value $n\pi/k_F$, the maximum $U_n(0)$ of the mode n approaches E_F; tunneling can occur through the effective barrier $U_n(x)$. At these values, the corresponding transmission probability $T_n(E_F)$ increases rapidly from zero to unity: tunneling occurs only within the narrow interval $\sqrt{W_0/k_F^2 R}$ around $n\pi/k_F$. The fact that the increase is rapid means that a given mode is either completely transmitted or completely reflected. This is in accordance with the physics of the quasi-classical limit $R \gg \lambda_F$: classically,

there is no tunneling and an electron either passes the constriction or is reflected. Increasing W_0, we thus increase the number of propagating modes one by one, at $W_0 = \pi/k_F$, $2\pi/k_F$, $3\pi/k_F \ldots$. Therefore, the total transmission $\sum_n T_n(E_F)$ is expected to increase stepwise with W_0. The conductance also increases stepwise, in units $2e^2/h$, see Fig. 6.3. This *conductance quantization* has indeed been experimentally observed, see [5]. It corresponds to another violation of Ohm's law: changing the cross-section of a small conductor leads to a stepwise, rather than a linear, increase of the conductance.

Conductance of an Aharonov-Bohm Loop

As it is well-known, for an electron in a magnetic field $\boldsymbol{B}$, the canonical momentum is given by the replacement $\boldsymbol{p} \to (\boldsymbol{p} + e\boldsymbol{A}/c)$, where $\boldsymbol{A}$ is the vector potential with $\boldsymbol{B} = \mathrm{rot}\ \boldsymbol{A}$. An electron propagating in a magnetic field thus acquires an additional phase-factor: $\psi_k(\boldsymbol{r}) = \exp(\mathrm{i}(\boldsymbol{k}\cdot\boldsymbol{r} + \int^{\boldsymbol{r}} e\boldsymbol{A}.\mathrm{d}\boldsymbol{r}'/\hbar c))$. Let us consider a clean one-mode quantum wire, forming a loop of area S, threaded by a flux $\phi = BS$ (see Fig. 6.4).

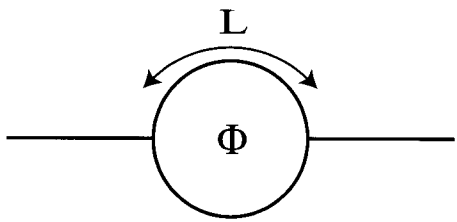

Fig. 6.4. Aharonov-Bohm loop

For an electron propagating around the loop, the additional phase factor is

$$\frac{e}{\hbar c}\oint_{loop} \boldsymbol{A}\cdot\mathrm{d}\boldsymbol{r} = \frac{e}{\hbar c}\int \mathrm{rot}\ \boldsymbol{A}\cdot\mathrm{d}\boldsymbol{S} = \frac{e}{\hbar c}\int \boldsymbol{B}\cdot\mathrm{d}\boldsymbol{S} = 2\pi\phi/\phi_0 \qquad (6.14)$$

where $\phi_0 = hc/e$ is the *flux quantum*. Hence, the total phase for an electron propagating from left to right along the upper arm (length L) is given by $kL - \pi\phi/\phi_0$, whereas an electron propagating along the lower arm (same length L) acquires a phase $kL + \pi\phi/\phi_0$. The transmission amplitude for propagation from left to right is thus given by

$$t_{\ell r}(E_F) = (\mathrm{e}^{\mathrm{i}(k_F L + \pi\phi/\phi_0)} + \mathrm{e}^{\mathrm{i}(k_F L - \pi\phi/\phi_0)})/2 \qquad (6.15)$$

where $k_F = mv_F/\hbar$ is the Fermi wave vector. As a result, $T(E_F) = |t_{\ell r}(E_F)|^2 = |\mathrm{e}^{\mathrm{i}(k_F L+\pi\phi/\phi_0)} + \mathrm{e}^{\mathrm{i}(k_F L-\pi\phi/\phi_0)}|^2/4 = (1 + \cos 2\pi\phi/\phi_0)/2$. This is a *periodic function* of the applied flux ϕ, with period ϕ_0. Therefore, the conductance of the loop, $\mathcal{G} = (2e^2/h)T(E_F)$, will be characterized by periodic oscillations as a function of flux: these are the so-called Aharonov-Bohm oscillations.

Diffusive Quantum Wire

So far we have considered quantum ballistic conductors, with a total length L smaller than the elastic mean free path l_e. Consider now a two-dimensional diffusive quantum wire longer than the elastic mean free path ℓ_e, but still smaller than the inelastic length L_{in}, and connected to two reservoirs. We assume that there are many modes, $N = k_F W/\pi \gg 1$, which guarantees that the electron states are not localized [3]. As we have seen in the previous section, we expect such a wire to be characterized by its residual conductivity. In terms of the conductance this means that we should find $\mathcal{G} = \sigma_0 W/L$ in this case. In order to verify this, we need to know the transmission coefficients $T_n(E_F)$ for a diffusive wire. Let us present the expected residual conductance $\mathcal{G}$ as

$$\mathcal{G} = \frac{n_0 e^2 \tau_e}{m} \frac{W}{L} \tag{6.16}$$

Using the fact that the two-dimensional electron density $n_0 = k_F^2/(2\pi^2)$, we obtain

$$\mathcal{G} = N \frac{e^2}{\pi\hbar} \frac{\ell_e}{2L} \tag{6.17}$$

Naively, one thus expects that $T_n(E_F) = \ell_e/(2L)$: each mode is transmitted with a small probability $\propto \ell_e/L$. In fact this is incorrect; a more detailed analysis shows that the transmission probabilities of a disordered wire are random numbers, distributed according to a bimodal distribution [6]

$$p(T) = \frac{\ell_e}{\pi L} \frac{1}{\sqrt{T(1-T)}} \tag{6.18}$$

The distribution is maximal for $T = 0$ or $T = 1$, other values of T are in fact very improbable. In other words, a given mode has either transmission 1 or 0. This is, once more, a quasi-classical result: a particle is either transmitted or reflected. The average transmission per channel, however, $\langle T \rangle = \int \mathrm{d}T T p(T) = \ell_e/(2L)$ is small. Unfortunately, no information concerning the bimodal character of the distribution $p(T)$ is contained in the conductance as the latter depends on the average value of T_n only. In order to obtain more information on $p(T)$, one could measure the fluctuations of the current around its average value, i.e. the current noise [7].

We have seen that quantum transport in a phase-coherent conductor (typical size L smaller than the inelastic length L_{in}) can be formulated in terms of a scattering problem. The formulation is essentially non-local: the total current I across the sample is found as a function of the bias applied to the terminals. As a result we find the nonlocal conductance rather than the local conductivity. This reflects the fact that quantum-mechanical correlations are maintained throughout a phase-coherent sample.

The conductance is determined by the elastic transmission coefficient. As long as scattering within the sample is elastic, it is clear that the dissipation associated with electric transport cannot occur in the sample itself. Indeed, the excess energy due to a finite applied bias voltage is dissipated in the reservoirs. The elastic transmission probability is phase-sensitive, which opens up the possibility of quantum-interference phenomena. As an example we discussed the single-mode, ballistic Aharonov-Bohm loop; for the diffusive multi-mode case, see Sect. 6.2. The various examples showed that simple, classical rules concerning parallel or series addition of resistances do not apply in the quantum limit. We also saw that ballistic samples, i.e. samples without any elastic impurity scattering ($L < \ell_e$) are still resistive.

So far we have treated electrons as if they were non-interacting particles. In reality electrons interact through Coulomb repulsion. According to the Landau Fermi-liquid theory, the non-interacting picture remains correct under certain conditions, even in the presence of interactions. We will review these ideas briefly below, and then discuss that the conditions for Landau Fermi-liquid theory to hold are sometimes violated in low-dimensional systems.

6.1.2 Coulomb Interactions

Fermi Liquid

Non-Interacting Electrons

As it is well-known, the ground state of a non-interacting Fermi gas is a filled Fermi sea: all states are occupied up to the Fermi energy E_F, which is a function of the electron density n_0. Adding or removing particles therefore simply leads to a shift of E_F. Excitations are induced by creating particle-hole pairs: an electron of wave vector $\boldsymbol{k}$ is taken from the Fermi sea and put to an empty state $\boldsymbol{k}'$ outside. We have created two quasi-particles: a particle with wave vector $\boldsymbol{k}'$ and a hole with wave vector $\boldsymbol{k}$. These particle-hole pairs form a continuum of states that carry a momentum $\boldsymbol{p} = \hbar(\boldsymbol{k}' - \boldsymbol{k})$ and an energy $E = \frac{\hbar^2}{2m}(k'^2 - k^2)$.

At finite temperature T, these excitations are created thermally, which leads to the characteristic smearing of the Fermi distribution over a width proportional to T. However, the smearing is in typical metals always small compared to the Fermi energy: this is why even at finite temperature the physics of non-interacting electrons is determined by *Fermi surface properties* only. An example is the specific heat of the three-dimensional non-interacting electron gas, given by $c_V = \pi^2 k_B^2 T \rho(E_F)/3$, which is determined by the density of states at the Fermi level, $\rho(E_F) = m k_F/(\hbar^2 \pi^2)$. Another example is the Landauer conductance $\mathcal{G} = 2(e^2/h)\sum_n T_n(E_F)$, which is determined by the transmission probabilities $T_n(E_F)$ at the Fermi level.

According to Landau, in the presence of repulsive interactions, the above description remains largely intact as long as the interactions are weak and short-ranged [1, 2]. More precisely: *there exists a one-to-one correspondence between the eigenstates of the non-interacting and the interacting Fermi gas.*

This hypothesis means that:

(1) The filled Fermi sea as a ground state persists in the interacting case;
(2) The concept of quasi-particles (particles and holes) persists in the interacting case.

How do interactions manifest themselves? Consider a filled Fermi sea with zero total momentum and one additional quasi-particle of momentum $\hbar\boldsymbol{k}$ close to the Fermi surface, $k \sim k_{\mathrm{F}}$. Now, let us switch on the interactions between electrons. Since interactions conserve the total momentum, the quantity $\hbar\boldsymbol{k}$ cannot change. Moreover, by continuity, the minimum momentum $\hbar k_{\mathrm{F}}$ needed to create a quasi-particle cannot change either. Consequently, the energy has to change following

$$E(\boldsymbol{k}) - E_{\mathrm{F}} \simeq \frac{\hbar^2}{2m} k_{\mathrm{F}}(k - k_{\mathrm{F}}) \to \frac{\hbar^2}{2m^*} k_{\mathrm{F}}(k - k_{\mathrm{F}}) \tag{6.19}$$

We see that interactions renormalize the electron mass $m \to m^*$. More generally speaking, interactions lead to parameter renormalization, but the structure of the theory, and hence the behavior of various physical quantities remains unchanged. An example is the electronic specific heat of the interacting electron gas $c_V = \pi^2 k_{\mathrm{B}}^2 T \rho^*(E_{\mathrm{F}})/3$: its temperature dependence is unchanged but it is determined by the renormalized density of states $\rho^* = m^* k_{\mathrm{F}}/(\hbar^2\pi^2)$ at the Fermi level.

As already stated above, in order for Fermi-liquid theory to hold, electron-electron interactions must be weak and short-ranged. Coulomb interactions are, generally speaking, strong and long ranged. In free space, a positive test charge q induces a potential $\varphi(r) = q/r$. In metals it is the *screening* of this potential by conduction electrons that makes the potential effectively short-ranged. In fact, in a metal, a positive test charge q will attract a screening cloud of negatively charged electrons around it, such that the potential drops rapidly over a short distance. According to the quasiclassical Thomas-Fermi theory [1,2], the resulting potential follows $\varphi(r) = q\mathrm{e}^{-r/r_0}/r$, where $r_0 \sim \lambda_{\mathrm{F}}$ is the *screening length.* Screening is very effective in an ordinary bulk metal: the electrons are relatively free and fast and will screen any charge inhomogeneity from all sides on a short scale $\sim\lambda_{\mathrm{F}}$. This is why Fermi liquid theory works quite well for ordinary (clean) metals.

For weak, short-ranged interactions, a simple perturbative calculation enables us to show that quasi-particles close to the Fermi surface are indeed long-lived objects [1, 2]. Consider the interaction between an electron outside the

Fermi sphere (wave vector $\boldsymbol{k}_1$) with an electron within the Fermi sea (wave vector $\boldsymbol{k}_2$); these particles scatter into two states outside the Fermi sphere (wave vectors $\boldsymbol{k}_3$ and $\boldsymbol{k}_4$). Momentum conservation implies that $\boldsymbol{k}_1 + \boldsymbol{k}_2 = \boldsymbol{k}_3 + \boldsymbol{k}_4$. With the help of Fermi golden rule, the inverse scattering time $1/\tau$ of this process is derived

$$\frac{1}{\tau} = \frac{2\pi}{\hbar} \sum_{\boldsymbol{k}_2, \boldsymbol{k}_3} |U(|\boldsymbol{k}_3 - \boldsymbol{k}_1|)|^2 \delta(E_{k_1} + E_{k_2} - E_{k_3} - E_{k_1+k_2-k_3}) \tag{6.20}$$

Here $\boldsymbol{k}_3 - \boldsymbol{k}_1 \equiv \boldsymbol{q}$ is the wave vector transferred between the particles by the interaction; the corresponding matrix element is the Fourier transform of the screened Coulomb interaction, $U(q) = e^2/[q^2 + (2\pi/r_0)^2]$. Note that, due to screening on distances beyond r_0, this matrix element remains finite for small values of $q < 1/r_0$, such that $U(q = 0) \sim e^2 r_0^2 \sim e^2 \lambda_F^2 \sim e^2/k_F^2$. Further calculations use energy conservation and the fact that the first electron is close to the Fermi surface, $k_1 \sim k_F$. As a result we have $k_{2,3} \sim k_F$ and $q \approx 0$, so that

$$\frac{1}{\tau} \sim |U(0)|^2 (E_{k_1} - E_F)^2 \sim \left(\frac{k_B T}{E_F}\right)^2 \tag{6.21}$$

Here we used the fact that at finite temperatures, $E_{k_1} - E_F \sim k_B T$. We finally obtain the temperature-dependent lifetime for Fermi liquid quasi-particles, $\tau \sim 1/T^2$, as anticipated in Sect. 6.1.1. Interaction effects can be described by Fermi-liquid theory at sufficiently low temperatures, where this lifetime (and the corresponding inelastic length) is long enough.

Weakened Screening in Low-Dimensional Systems

There are various situations in which the screening phenomenon is less effective and interactions become strong:

1. *Metals of low dimensionality.* In a two-dimensional electron system for instance, electrons are confined to a plane. The screening cloud forms only within this plane: there are no electrons perpendicular to the plane. As a result, electric field lines can escape in this direction and give rise, within the plane, to a residual long-range component of the interaction.
2. *Low density systems.* In order to understand when Coulomb interactions between electrons are weak, the average Coulomb energy U has to be compared with the average kinetic energy E_F. The average separation between electrons being λ_F, $U \sim e^2/\lambda_F$, and the ratio U/E_F is thus given by $U/E_F \sim e^2/(\hbar v_F)$. The Fermi velocity decreases with decreasing electron density n_0, hence the ratio U/E_F increases as n_0 is reduced. If the density is so low that $U \sim E_F$, interactions can no longer be considered as weak and Fermi-liquid theory usually breaks down.
3. *Presence of impurities.* As we have seen, impurities cause diffusive electron motion on scales beyond the elastic mean free path. Diffusion is slower than ballistic propagation, hence the formation of the screening cloud around

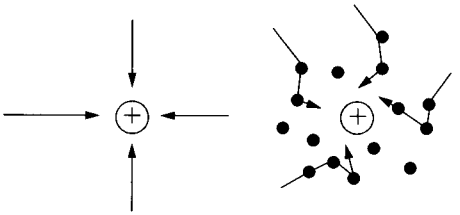

Fig. 6.5. Formation of the screening cloud in ballistic and diffusive systems

a charged inhomogeneity will take place on longer time scales in diffusive systems than in ballistic systems (see Fig. 6.5). This reduces the efficiency of screening in diffusive systems [8].

In these situations, the simple perturbative analysis presented in the previous paragraph is not correct and the Fermi-liquid description may cease to be valid. Generally, this implies that interaction effects do not lead to simple parameter renormalization; the entire structure of the theory changes and new phenomena can occur. Below, two important examples are analyzed, namely charging effects in tunnel junction systems and interaction effects in clean, single-mode quantum wires.

Tunnel Junctions and Coulomb Blockade

Coulomb Effects in Tunnel Junctions

Let us consider a *tunnel junction*, as depicted in Fig. 6.6. It consists of two diffusive multi-mode quantum wires (electrodes), separated by a tunnel barrier. The transport through such a junction is achieved through the phenomenon of quantum tunneling: in order for a charge to pass from one wire to the other, it must tunnel through the barrier separating them. If the conductance of the wires is large, the total conductance $\mathcal{G}_T$ of the system will be determined entirely by properties of the tunnel barrier:

$$\mathcal{G}_T = \frac{2e^2}{h} N T_B(E_F) \tag{6.22}$$

where N is the number of modes in the diffusive wires and T_B is the transmission coefficient of the barrier at the Fermi energy. Since tunneling is a rare

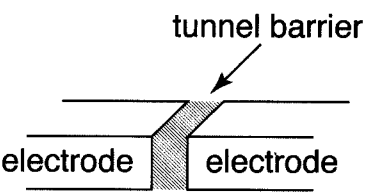

Fig. 6.6. Tunnel junction

event, $T_B(E_F) \ll 1$. In principle, apart from the conductance, we can also assign a capacitance, C, to the tunnel junction. As long as the dimensions of the tunnel junction are large, this capacitance will also be large, and its effects on the transport can be neglected. However, as the size of the junction is decreased, C decreases as well, and interesting new phenomena may arise [9].

Consider a single tunnel junction, biased by a voltage V. In view of the above discussion, the junction will be polarized by a charge $Q = CV$. Transport is achieved by tunneling of individual electrons with charge $-e$. Consider such a tunneling phenomenon, which leads to a change of the polarization charge by an amount $-e$. As a result, the difference ΔE in energy before and after the tunneling event is given by

$$\Delta E = \frac{Q^2}{2C} - \frac{(Q-e)^2}{2C} = \frac{e(Q-e/2)}{C} \tag{6.23}$$

We see that ΔE is positive if $Q > e/2$, i.e. if $eV > E_c \equiv e^2/2C$, where E_c is the *charging energy*. In other words, at low temperatures $k_B T \ll E_c$, we expect transport to be blocked if the bias voltage is smaller than E_c. This is the so-called *Coulomb blockade of tunneling*.

In order to observe this phenomenon in practice, a few conditions should be satisfied. Obviously, any energy scale entering the problem (voltage, temperature, ...) should be small compared to E_c. This implies working at low temperatures, or, alternatively, with small junctions such that the capacitance is small and the charging energy is large. Moreover, in order to observe the charging effect, the charge imbalance $Q - e$ with respect to Q must survive for sufficiently long a time. This implies a sufficiently opaque barrier, i.e. $\mathcal{G}_T \ll e^2/h$, such that a second tunneling event will not restore the charge Q. In addition, if the electrodes are good metals, screening is effective and a fast redistribution of the charge will inhibit the Coulomb blockade. Thus, not only the barrier but also its direct environment must be sufficiently resistive in order to observe the effect. Below we will study the effect of a resistive environment in some detail.

Single Junction in a Resistive Environment

Consider a single junction, embedded in a circuit, as depicted in Fig. 6.7. The tunnel junction 'sees' its capacitance C in parallel. Furthermore, the circuit contains a resistor R, representing the metallic electrodes or any other additional external resistance close to the junction. The junction is voltage biased by an ideal voltage source, kept at a voltage V_x. We can readily understand the effect of R on Coulomb blockade using a simple argument based on the uncertainty principle. Placing a resistor close to a junction with capacitance C introduces a charge redistribution time of the order of the time constant RC. According to the uncertainty principle, in order to observe Coulomb blockade, charges should not redistribute on scales shorter than $\hbar/E_c$. Thus, in order to observe the Coulomb blockade, $RC > \hbar/E_c$, which yields $R > h/e^2$ as the condition on R.

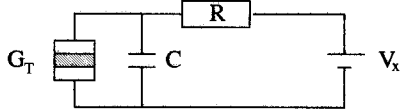

Fig. 6.7. Single junction embedded in a circuit

This simple estimate can be put on firmer ground, using a theoretical description of the environment, see [9]. The central idea in this theory is that, in the presence of a resistor, the voltage V across the junction does not equal V_x but fluctuates, $V(t) = V_x + \delta V(t)$, the fluctuating part being due to the Johnson-Nyquist noise induced by the resistor. In other words, the spectrum of the fluctuations is given by the fluctuation-dissipation theorem [10]

$$\langle \delta V(t) \delta V(t') \rangle_\omega = \hbar\omega \Re\mathrm{e}\,[Z_t(\omega)] \coth\left(\frac{\hbar\omega}{2k_\mathrm{B}T}\right) \tag{6.24}$$

where $Z_t(\omega)$ is the total impedance seen by the junction,

$$Z_t(\omega) = \frac{R}{1 + \mathrm{i}\omega RC}$$

The electrons which tunnel through the barrier interact *inelastically* with these fluctuations. The inelastic transmission through the barrier is characterized by the function $P(E)$: the probability to pass the barrier, thereby transferring an amount of energy E to the environment. In general, the current through the junction will be given by

$$I(V) = \frac{\mathcal{G}_T}{e}\left(1 - \mathrm{e}^{-\beta eV}\right) \int \mathrm{d}E \frac{E}{1 - \mathrm{e}^{-\beta E}} P(eV - E) \tag{6.25}$$

where $\beta = 1/k_\mathrm{B}T$. The probability $P(E)$ is determined essentially by the above spectrum (6.24). A detailed discussion of this function can be found in [9]. Here we will discuss the limiting case $T = 0$ only. In this case, $P(E) \sim E^{(2R/R_K - 1)}$ at low energies. Here $R_K = 1/\mathcal{G}_K = h/e^2$ is the *quantum resistance*. As a result, according to (6.25), we expect a non-linear $I - V$ characteristic, $I \sim V^{2R/R_K + 1}$. In the absence of any resistance ($R = 0$) the usual result $I = \mathcal{G}_T V$ is recovered with no hint of Coulomb blockade. As R is increased, a gap develops in the $I - V$ curve. In the limiting case $R \gg R_K$, one finds $P(E) \sim \delta(E - E_\mathrm{c})$, leading to a complete blockade of transport, $I = 0$, at voltages below E_c/e.

It is not so easy to experimentally verify the presence of Coulomb blockade in a single junction connected to a resistive environment. Diffusive quantum wires are in general not resistive enough: their resistance is typically small, $R = 1/\mathcal{G} = h/(2Ne^2) \ll R_K$. The corresponding gap in the $I - V$ curve is difficult to measure. It is not so easy to insert an additional big resistance close to the junction. An elegant way to circumvent this problem consists of using a second tunnel junction, as we discuss in the next section.

SET Transistor

In order to prevent fast charge redistribution close to the tunnel junction, one usually simply inserts a second tunnel junction. The so-called double junction device obtained this way, and depicted in Fig. 6.8, is known as the *single electron tunneling transistor* (SET transistor), a device pioneered by Fulton and Dolan [9].

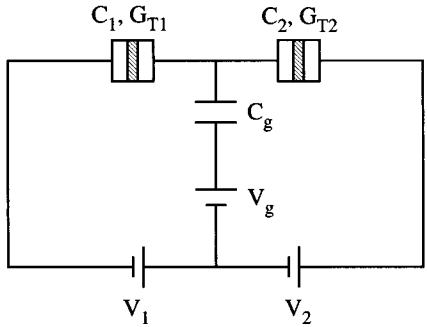

Fig. 6.8. The SET transistor

If the conductance of both junctions is sufficiently weak, $\mathcal{G}_{T,i} \ll e^2/h$ for $i = 1, 2$, the discrete number M of electrons inside the island between the junctions is well-defined. This number can be controlled by an additional gate-voltage V_g, capacitively coupled to the central island. Indeed, the electrostatic energy of the central island containing M electrons is given by

$$U(M) = \frac{(C_g V_g - Me)^2}{2C_\sigma} \tag{6.26}$$

where $C_\sigma = C_1 + C_2 + C_g$, see Fig. 6.9a. At low temperatures and for small enough bias voltages, the number of electrons inside the island remains fixed (Coulomb blockade) unless V_g is tuned to one of a set of special values such that $U(M) = U(M+1)$. This happens for $C_g V_g/e = M + 1/2$. At these values of V_g, the charge of the island can be changed from M to $M+1$, leading to a finite value of the linear conductance $\mathcal{G}$. This leads to the so-called Coulomb oscillations, see Fig. 6.9b. Note in particular the periodicity of these oscillations: if plotted as a function of $eN_g = C_g V_g$, they are separated by the electron charge e.

The SET transistor is an extremely useful device, which is not only used in fundamental research, but has also found applications in various fields of interest such as metrology (accurate electron pumps used as current or capacitance standards) and applied physics (the SET as an electrometer or as a thermometer).

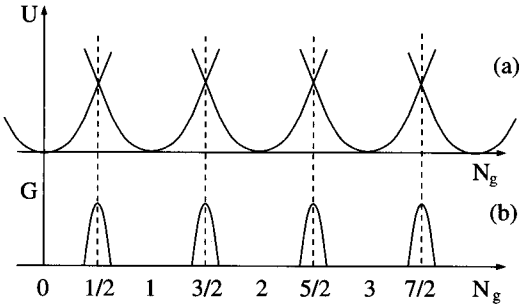

Fig. 6.9. (**a**) Charging energy of the central island as a function of $N_g = C_g V_g/e$. (**b**) Coulomb oscillations

Interactions in One-dimensional Systems

Peculiarities in One Dimension

The ground state of the non-interacting one-dimensional (1D) electron gas has quite remarkable properties. The Fermi surface is peculiar: it consists of two points only, at $-k_F$ and k_F. This implies that the particle-hole spectrum is very different from its higher dimensional counterpart. Rather than a continuum of particle-hole states, the low energy excitations occur in sectors, located around wave vectors 0 and $\pm 2k_F$, see Fig. 6.10. No low-energy excitations exist around $\pm k_F$, as this implies particles far from the Fermi surface, which costs an energy of the order of at least E_F.

Here we are interested in *long-wavelength excitations*, involving particle-hole pairs with small total momentum $p \equiv \hbar q = \hbar(k' - k)$. We then find a linear dependence of the energy on momentum:

$$E = \frac{\hbar^2}{2m}(k'^2 - k^2) = \hbar|k' - k|\hbar k_F/m = \hbar v_F|q| \tag{6.27}$$

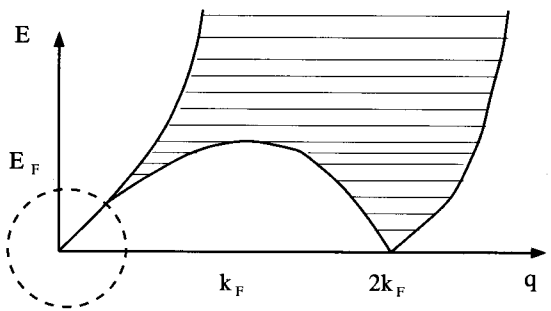

Fig. 6.10. Particle-hole spectrum of a one-dimensional Fermi gas. The *dotted circle* is the low-energy region of interest, where the dispersion is linear

The nature of a particle-hole pair, which consists of two fermions, is bosonic. It is therefore natural to write down the following effective bosonic Hamiltonian describing the low-energy, long-wavelength excitations of the 1D electron gas [11]:

$$\hat{H} = \sum_q \hbar v_F |q| \hat{b}_q^\dagger \hat{b}_q \tag{6.28}$$

Here the operators $\hat{b}_q^\dagger$ and $\hat{b}_q$ satisfy standard bosonic commutation rules like $[\hat{b}_q, \hat{b}_{q'}^\dagger] = \delta_{q,q'}$. This Hamiltonian describes the low-lying excitations of the 1D electron gas in terms of an ensemble of harmonic oscillators, each with a frequency $\omega_q = v_F|q|$. Below, rather than formally analyzing this bosonized Hamiltonian, we will proceed in a more transparent way. We will understand what the oscillating modes correspond to physically and see how interactions affect them.

Form of the Interaction

We consider a single-mode clean quantum wire of length L, located at a distance D_0 from a metallic substrate (see Fig. 6.11). We ignore the reservoirs for the moment and consider spinless electrons for simplicity. As discussed above, screening is ineffective in one dimension, hence the Coulomb repulsion between electrons is, in principle, long-ranged. The presence of the substrate provides screening of the interactions at distances larger than D_0. We assume that $\lambda_F \ll D_0 \ll L$: the interaction potential $U(x)$ is short-ranged on the scale L, but long-ranged on the scale λ_F. The latter condition means that we can ignore exchange effects, and restrict ourselves to a density-density interaction energy of the form $U_{int} = (1/2) \int dx dx' n(x) U(x-x') n(x')$, where $n(x)$ is the electron density in the wire at the point x. On the scale L, $U(x)$ is short-ranged, and we approximate $U(x) = U_0 \delta(x)$. As a result $U_{int} = (U_0/2) \int dx n^2(x)$.

Charge Density Waves

We next consider fluctuations of the electron density in the wire. To this end, the total density is written as $n(x,t) = n_0 + \delta n(x,t)$, where $n_0 = k_F/\pi$ is the 1D homogeneous equilibrium spinless electron density and δn the fluctuating part. It is a common practice to introduce the associated displacement field

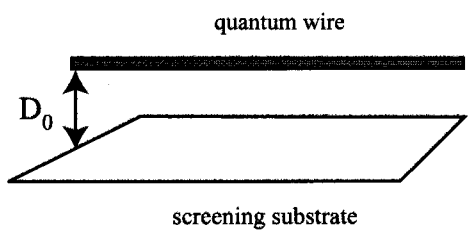

Fig. 6.11. Interacting quantum wire with a screening substrate

$u(x,t)$ such that $\delta n(x,t) = -n_0 \partial u/\partial x$. We also introduce the velocity $v = \partial u/\partial t$, such that the 1D electric current density can be written as $j = -n_0 ev$. We seek the (classical) equation of motion of the field u.

If the density of the 1D electron gas is locally increased by an amount δn with respect to n_0, a force will try to restore the equilibrium value n_0. As long as δn is small, the force will be harmonic, i.e. $\propto \delta n$. The origin of the restoring force is two-fold: the pressure in the gas and the Coulomb repulsion. For fermions, the pressure is given by $P = \hbar^2 \pi n^3/3m$; the associated restoring force is

$$-\partial P/\partial x = -\frac{\hbar^2 \pi^2 n_0^2}{m} \frac{\partial \delta n}{\partial x} = \frac{\hbar^2 \pi^2 n_0^3}{m} \frac{\partial^2 u}{\partial x^2} \tag{6.29}$$

The Coulomb repulsion leads to the restoring force

$$-U_0 \frac{\partial \delta n}{\partial x} = n_0 \frac{\partial^2 u}{\partial x^2} \tag{6.30}$$

Therefore, the equation of motion reads

$$m n_0 \frac{\partial^2 u}{\partial t^2} = \left[U_0 + \frac{\hbar^2 \pi^2 n_0}{m} \right] n_0^2 \frac{\partial^2 u}{\partial x^2} \tag{6.31}$$

We seek wave-like solutions of the form $u \sim \mathrm{e}^{\mathrm{i}(qx - \omega t)}$, that correspond to *charge density waves* of the form $\delta n \sim \mathrm{e}^{\mathrm{i}(qx - \omega t)}$. The dispersion relation of these waves is obtained immediately from (6.31),

$$\omega^2 = \left[\frac{n_0 U_0}{m} + \left(\frac{\hbar \pi n_0}{m} \right)^2 \right] q^2 \tag{6.32}$$

We see that the dispersion is *linear*, $\omega_q = s|q|$, characterized by a *velocity*

$$s = v_\mathrm{F} \sqrt{1 + \frac{U_0}{\pi \hbar v_\mathrm{F}}} \equiv v_\mathrm{F}/g \tag{6.33}$$

Here we used $n_0 = k_\mathrm{F}/\pi$ and introduced the *interaction parameter* $g = 1/\sqrt{1 + U_0/(\pi \hbar v_\mathrm{F})}$. For non-interacting electrons, $U_0 = 0$, we have $g = 1$; repulsive interactions decrease g such that $g < 1$. In the absence of interactions, $g = 1$, we find $s = v_\mathrm{F}$. This corresponds to the results obtained at the beginning of this section for the non-interacting 1D electron gas. A comparison with those results shows that the particle-hole excitations of momentum $p = \hbar q$ and energy $\hbar v_\mathrm{F}|q|$ in fact correspond to charge density waves with a linear dispersion $\omega_q = v_\mathrm{F}|q|$. They propagate along the wire at the Fermi velocity v_F. We thus identified the physical origin of the bosonized oscillator modes. In the presence of interactions, the charge-density wave picture remains largely intact. Interactions mainly will renormalize the velocity $v_\mathrm{F} \to s = v_\mathrm{F}/g$. As a result, charge density waves propagate faster in a repulsively interacting electron gas.

Electrical Transport without Reservoirs

In order to study the effect of interactions on the transport properties of a one-mode quantum wire, we first consider the response of the 1D interacting Fermi gas (Luttinger liquid) without reservoirs to an external electric field $\mathcal{E}(x,t) = \mathcal{E}_{k,\omega} e^{i(kx-\omega t)}$. This leads to an additional force $-e\mathcal{E}(x,t)$, that should be added to the right hand side of the equation of motion (6.31). The solution can be written as $u_{k,\omega} e^{i(kx-\omega t)}$, with

$$u_{k,\omega} = -\frac{e\mathcal{E}_{k,\omega}}{m} \frac{1}{s^2k^2 - (\omega + i\eta)^2} \tag{6.34}$$

where the small imaginary part $i\eta$ has been added to ensure convergence. We conclude that the current density obeys the relation $j_{k,\omega} = i\omega e n_0 u_{k,\omega} = \sigma_{k,\omega}\mathcal{E}_{k,\omega}$ with the conductivity [12]

$$\sigma_{k,\omega} = -\frac{e^2 n_0}{m} \frac{i\omega}{s^2k^2 - (\omega + i\eta)^2} \tag{6.35}$$

The conductivity is a non-local quantity: it depends not only on frequency but also on the wave vector. The non-local nature of transport is clearly seen upon Fourier transformation to real space: we find $j(x) = \int dx' \sigma(x - x', \omega) E(x')$ meaning that the current at x generally depends on the values of the electric field at different points x'. The scale for non-locality is determined by the conductivity; as can be seen from (6.35), typical contributions come from $k \sim \omega/s$, hence the scale is given by $L_\omega \sim 1/k \sim s/\omega$. In the zero-frequency limit, $L_\omega \to \infty$, and non-locality persists over the entire length L of the wire. We are interested in the real part of the conductivity, in the zero-frequency limit,

$$\Re e\, [\sigma_{k,\omega}]_{\omega\to 0} = \frac{\pi e^2 n_0}{ms} \delta(k) \tag{6.36}$$

Then, upon Fourier transformation,

$$\mathcal{G} = \int \frac{dk}{2\pi} e^{-ikx} \Re e\, [\sigma_{k,\omega}]_{\omega\to 0} = ge^2/h \tag{6.37}$$

For $g = 1$ we recover the familiar Landauer result $\mathcal{G} = e^2/h$ for a non-interacting, single-mode quantum wire with spinless electrons. However, according to the result (6.37), the conductance of an interacting quantum wire is suppressed in the presence of repulsive interactions.

Role of the Reservoirs

It is important to realize that the above result has been obtained in the absence of electron reservoirs. In the presence of reservoirs, a different result is found.

According to the Landauer formulation, for a conductor coupled to reservoirs, the conductance is proportional to the electron transmission coefficient of the wire. As long as the transmission is perfect, i.e. in the absence of any backscattering, we expect that $T(E_F) = 1$, and $\mathcal{G} = e^2/h$ for a spinless single-mode quantum wire. In the presence of Coulomb interactions this result should not change: Coulomb interactions conserve momentum, and thus cannot induce any backscattering. Therefore, we expect that $T(E_F) = 1$ even in the interacting case; hence $\mathcal{G}$ should be *unaffected by interactions*, $\mathcal{G} = e^2/h$. These statements can be substantiated by more detailed calculations, see [12–14].

We conclude that a DC transport measurement on a clean interacting quantum wire, well-connected to reservoirs such that the transmission coefficient is unity, will not reveal any interaction effects. Below we will discuss two possible ways to make interactions in the wire visible in a transport measurement.

Transport at Finite Frequency

If a time-dependent bias voltage is applied at a finite frequency ω, the electrons perform an oscillatory motion within the quantum wire over a distance $L_\omega = s/\omega$. If ω is large enough, such that L_ω is smaller than the length L of the wire, the oscillating electrons are confined to the wire and do not 'feel' the reservoirs anymore. At these frequencies, the presence of reservoirs can be ignored and the conductivity is given by the result (6.35), which depends on the interaction strength through the renormalized velocity $s = v_F/g$.

There is a practical problem, though. The frequencies needed to achieve the conditions $L_\omega < L$ are rather high; for $L \sim 1$ μm and a Fermi velocity $\sim 10^5$ m/s, we have $\omega > 10^{11}$ radian/s. It is difficult to perform transport experiments at such high frequencies.

Alternatively, if the wire is capacitively connected to a side-gate, frequency-dependent three-terminal measurements can be performed [15]. It turns out that even at low frequencies, such that $L < L_\omega$, the frequency-dependent side-gate conductance is modified by interactions. It has been shown that a measurement of the frequency-dependent, out-of-phase part of the side-gate conductance at low frequencies can be used to determine the interaction constant g directly.

Tunneling in an Interacting Quantum Wire

As we have seen in Sect. 6.1.2 in the case of Coulomb blockade, tunnel junctions can be used to make interactions visible in transport phenomena at zero frequency. As we will see, this is also true for interacting quantum wires. Indeed, in the presence of a tunnel barrier, momentum is no longer conserved, and the transmission coefficient will be suppressed, $T(E_F) < 1$, even in the absence of interactions. It turns out that in the presence of interactions, $T(E_F)$ becomes strongly energy-dependent and is further suppressed [16]. The

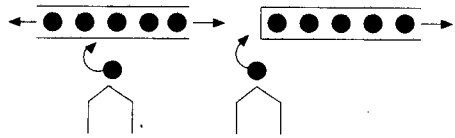

Fig. 6.12. Tunneling into a one-dimensional quantum wire

physical origin of this effect is that the tunneling electron has to overcome a Coulomb barrier in order to enter the interacting wire but the other electrons in the wire have to be displaced first.

The theoretical analysis of this phenomenon is quite complicated, and will not be discussed here. The main idea is similar to the one discussed in Sect. 6.1.2. We introduce the transmission probability $T(\epsilon)$ for an electron to tunnel into the quantum wire at energy $E = E_F + \epsilon$ close to the Fermi energy, thereby interacting with the charge-density excitations. It turns out that this probability also shows a power-law behavior at low energies, $T(\epsilon) \sim \epsilon^{\alpha}$, where the power exponent α depends on the interaction constant g and on the precise set-up. This generally leads to a non-linear $I-V$ characteristic such as $I \sim V^{\alpha+1}$. We will illustrate this below with some relevant examples.

We first consider tunneling from a Fermi liquid metallic reservoir to an interacting quantum wire [17], see Fig. 6.12. In the left panel, tunneling occurs in the middle of the wire and electrons can be displaced both to the left and to the right to accommodate the incoming electron. Detailed calculations show that $T(\epsilon) \sim \epsilon^{\alpha_m}$ where $\alpha_m = (1/g + g - 2)/8$. In the absence of interactions, $g = 1$ and the power α_m vanishes. The transmission coefficient is a constant and the current is given by $I = \mathcal{G}_T V$. Increasing the interaction strength such that $g < 1$, the exponent α_m grows, and tunneling is strongly suppressed at low energies. This leads to a non-linear $I-V$ characteristic with $I \sim V^{\alpha_m+1}$. In the right panel, tunneling occurs at the end of the wire, so electrons can be displaced only in one direction in order to accommodate the incoming particle. Indeed, the tunneling is more strongly suppressed in this case, $T(\epsilon) \sim \epsilon^{\alpha_e}$ where $\alpha_e = (1/g - 1)/4$. We see that $\alpha_e > \alpha_m$ in the interacting case $g < 1$.

We finally consider the case where the tunneling occurs within the quantum wire itself, due to the presence of an impurity. In this case $T(\epsilon) = \epsilon^{1/g-1}$, and $\alpha = 1/g - 1$. In particular, this means that the wire becomes insulating at the Fermi energy, i.e. for $\epsilon = 0$, which is a direct consequence of the repulsive interactions. This effect is a possible explanation for the suppression of conductance at low temperatures, experimentally found in disordered quantum wires [13].

6.2 Quantum Transport in Disordered Conductors

6.2.1 Introduction: Phase Coherence, Mesoscopic Regime, Physical Length Scales

This tutorial part describes in more detail some consequences of phase coherence in disordered conductors in the diffusive regime, i.e. when the length of the system is much larger than the elastic mean free path ℓ_e. It will be shown how physical properties of phase-coherent conductors can be simply related to the classical return probability for a diffusive particle. We shall mainly focus on weak-localization corrections, universal conductance fluctuations and the density-of-states anomaly. We consider weakly disordered conductors, for which the mean free path ℓ_e is much larger than the distance between electrons: $k_F \ell_e \gg 1$, where k_F is the Fermi wave vector. More details about this topic will be available at [18].

Length Scales

A disordered conductor is described by four length scales: the sample[1] size L, the mean free path ℓ_e which describes the elastic collisions, the Fermi wave length λ_F which depends on the density of electrons and the coherence length L_ϕ. This latter scale is very important because the effects we aim to describe result from the phase coherent interferences of the wave functions and thus disappear beyond L_ϕ. Smaller distances define *the mesoscopic regime.* Here, we shall mostly consider an electron gas in the following limits

$$\lambda_F \ll \ell_e \ll L \ll L_\phi \tag{6.38}$$

which correspond to a *weakly disordered* ($\lambda_F \ll \ell_e$), *mesoscopic* ($L \ll L_\phi$) metal in the *diffusive regime* ($\ell_e \ll L$). When the disorder strength becomes such that $\ell_e \sim \lambda_F$, the wave functions become localized on a typical scale ξ called the localization length [19]. Here, we shall restrict the discussion to the diffusive regime where $\xi \to \infty$. In this regime, an electron propagates diffusively because it experiences many elastic collisions while moving through the sample. The typical distance covered by the diffusive particle in a time t varies as $r^2(t) \simeq Dt$. The diffusion coefficient D is given by

$$D = \frac{v_F^2 \tau_e}{d} = \frac{v_F \ell_e}{d}. \tag{6.39}$$

$\tau_e = \ell_e / v_F$ is the elastic collision time and v_F is the Fermi velocity. The diffusive motion is thus characterized by a new time scale τ_D, called the *Thouless time*, which is the typical time for an electron to travel through the sample. It is defined as $\tau_D = L^2/D$. This time scale corresponds to a new energy scale E_c named the *Thouless energy*:

[1] If the shape is anisotropic, we define L_x, L_y and L_z.

$$E_c = \frac{\hbar}{\tau_D} = \frac{\hbar D}{L^2}. \tag{6.40}$$

This energy plays a very important role in the description of transport and spectral properties (see for example [20]). Finally, in the diffusive regime, the phase coherence length L_ϕ is related to the phase coherence time τ_ϕ, which accounts for the breaking of the phase coherence $L_\phi^2 = D\tau_\phi$.

Classical Transport

Although electrons behave like waves, physical properties like conductivity can be calculated, in a first approximation, assuming that interferences between electronic waves can be neglected. For the conductance, this leads to the classical expression $\sigma_0 = se^2 D\rho_0$, which is known as the Einstein relation [1]. ρ_0 is the average density of states per spin direction and $s = 2$ is the spin degeneracy. For free electrons where $\epsilon = \hbar^2 k^2/2m$, the density of states ρ_0 at the Fermi level can be written in any dimension d as a function of the electronic density n

$$\rho_0 = \frac{nd}{2s\epsilon_F} \tag{6.41}$$

so that, from Einstein relation and (6.41), one recovers the usual expression of the Drude conductivity [1][2]:

$$\sigma_0 = \frac{ne^2\tau_e}{m} \tag{6.42}$$

For a sample of length L and section S, Ohm's law relates the conductance $\mathcal{G}$ to the conductivity through: $\mathcal{G} = \sigma_0 S/L$. More generally, for an isotropic system in dimension d: $\mathcal{G} = \sigma_0 L^{d-2}$. The conductance has the dimension of e^2/h, and it is convenient to define a dimensionless conductance $g = \mathcal{G}/(e^2/h)$. Using Ohm's law and the Einstein relation, the dimensionless conductance can be rewritten as

[2]Remember that the density of states ρ_0 at the Fermi level can be written as

$$\rho_0 = \frac{dA_d}{(2\pi)^d} \frac{mk_F^{d-2}}{\hbar^2} \propto \frac{1}{\hbar\lambda_F^{d-1} v_F}$$

where $k_F = \sqrt{2m\epsilon_F}/\hbar$ and where A_d is the volume of the unit sphere in dimension d:

$$A_d = \frac{\pi^{d/2}}{\Gamma(1+d/2)} \qquad A_3 = \frac{4\pi}{3} \qquad A_2 = \pi \qquad A_1 = 2$$

Thus from Einstein relation, the conductivity and the conductance can be rewritten as

$$\sigma_0 = sA_d \frac{e^2}{h} \left(\frac{k_F}{2\pi}\right)^{d-1} \ell_e \qquad \mathcal{G}_0 = s\frac{A_d}{(2\pi)^{d-1}} \frac{e^2}{h} (k_F L)^{d-2} k_F \ell_e$$

$$g = \frac{\mathcal{G}}{e^2/h} = \frac{\sigma_0 L^{d-2}}{e^2/h} = 2\pi s \frac{E_c}{\Delta} \tag{6.43}$$

We have introduced the average spacing between energy levels, which is simply related to the inverse of the density of states: $\Delta = 1/(\rho_0 L^d)$. Thus, the dimensionless conductance measures the ratio between the Thouless energy and the interlevel spacing. Finally, one notes that the dimensionless conductance can also be written as the ratio of two volumes

$$g = sdA_d \frac{\Omega}{\lambda_F^{d-1} v_F \tau_D} \tag{6.44}$$

Ω is the volume of the system and the significance of the volume $\lambda_F^{d-1} v_F \tau_D$ will become clear in Sect. 6.2.3.

Quantum Transport: Outline

Deviations from the classical Drude transport arise because of phase coherence. In the following sections, we explain why phase-coherent effects are small in the limit $k_F \ell_e \gg 1$. Their influence is most important when the system size is smaller than the phase coherence length L_ϕ, which corresponds to the mesoscopic regime. In the next section, the conductance is demonstrated to be related to the probability for an electron to diffuse through the sample. By looking at the structure of this probability, which is the product of two quantum amplitudes, we study the conditions under which deviations from classical transport may appear, using an intuitive trajectory approach. We introduce the notion of quantum crossing which is the source of the quantum behavior. In Sect. 6.2.4, the weak-localization correction is related to the trajectories with one quantum-crossing and a loop. In Sect. 6.2.5, some relevant solutions of the diffusion equation are presented, and used to calculate the weak-localization correction in a few specific geometries. In Sect. 6.2.7, the origin of the universal conductance fluctuations in the mesoscopic regime is explained as being related to trajectories with two quantum crossings. Finally, Sect. 6.3 concludes by a brief discussion on the role of the electron-electron interactions for understanding the anomaly of the density of states appearing at the Fermi level in a diffusive system.

6.2.2 Diffusive Electronic Transport, Transmission Coefficient and Conductance

Classical Probability

One aims at describing the propagation of a particle of energy ϵ from a point $\boldsymbol{r}$ to a point $\boldsymbol{r}'$. In quantum mechanics, this propagation is inferred from a probability amplitude, which is commonly expressed through a Green's function $G_\epsilon(\boldsymbol{r}, \boldsymbol{r}')$. We do not aim to develop the theory of Green's functions. For our

purpose here, it is sufficient to note that there are many possible scattering trajectories from $\boldsymbol{r}$ to $\boldsymbol{r}'$. Thus a Green function has the following structure: it is the sum of the probability amplitudes corresponding to various multiple scattering trajectories from $\boldsymbol{r}$ to $\boldsymbol{r}'$, each trajectory being characterized by an amplitude and a phase proportional to its action [21]

$$G(\boldsymbol{r},\boldsymbol{r}') = \sum_j A_j(\boldsymbol{r},\boldsymbol{r}') \tag{6.45}$$

Now, one asks about the probability to find a particle at point $\boldsymbol{r}'$ if it was initially injected at point $\boldsymbol{r}$. Such probability to go from $\boldsymbol{r}$ to $\boldsymbol{r}'$ is given by the squared modulus of the amplitude. From (6.45), this probability appears as the sum of amplitude squared terms, plus interference terms which pair different trajectories j and j'

$$|G(\boldsymbol{r},\boldsymbol{r}')|^2 = \sum_{j,j'} A_j(\boldsymbol{r},\boldsymbol{r}')A_{j'}(\boldsymbol{r},\boldsymbol{r}') = \sum_j |A_j(\boldsymbol{r},\boldsymbol{r}')|^2 + \sum_{j'\neq j} A_j(\boldsymbol{r},\boldsymbol{r}')A^*_{j'}(\boldsymbol{r},\boldsymbol{r}') \tag{6.46}$$

Since it is well known that in quantum mechanics, one must add amplitudes instead of intensities, the interference term (the second term in (6.46)) cannot be a priori neglected. However this second term describes interferences between different trajectories j and j'. Each of the contributions in this sum has a random phase which depends on the detail of the impurity configuration. After disorder averaging, the second term cancels and the probability is essentially given by the sum of intensities

$$\overline{|G(\boldsymbol{r},\boldsymbol{r}')|^2} = \sum_j \overline{|A_j(\boldsymbol{r},\boldsymbol{r}')|^2} \tag{6.47}$$

Since all phase factors have disappeared, the remaining term is completely classical. Indeed, let us assume that some event changes the phase of the amplitude A_j. The complex amplitude A_j^* gets the opposite phase, leaving the probability unchanged. The quantity $\overline{|G(\boldsymbol{r},\boldsymbol{r}')|^2} = \sum_j \overline{|A_j(\boldsymbol{r},\boldsymbol{r}')|^2}$ ressembles the classical probability and is the solution of a diffusion equation. We call it a 'diffuson'. To be more precise, but without any proof, we define the probability $P(\boldsymbol{r},\boldsymbol{r}',\omega)$ as

$$P(\mathbf{r},\mathbf{r}',\omega) = \frac{1}{2\pi\rho_0}\overline{G_\epsilon(\mathbf{r},\mathbf{r}')G^*_{\epsilon-\omega}(\mathbf{r}',\mathbf{r})}. \tag{6.48}$$

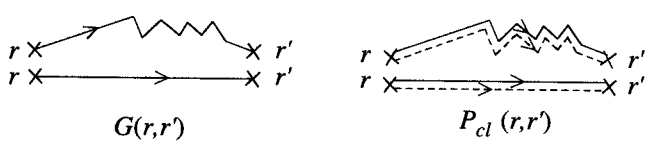

Fig. 6.13. Schematic representations of a Green's function $G(\boldsymbol{r},\boldsymbol{r}')$ and of the classical probability $P_{\rm cl}(\boldsymbol{r},\boldsymbol{r}') \propto \sum_j \overline{|A_j(\boldsymbol{r},\boldsymbol{r}')|^2}$. The upper diagrams exhibit a few collision events. They are not represented on the lower diagrams

The Green's function and its complex conjugate are taken at different frequencies. One can check that this probability is correctly normalized, that is $\int_0^\infty P(\boldsymbol{r},\boldsymbol{r}',t)\mathrm{d}\boldsymbol{r}' = 1$, where $P(\boldsymbol{r},\boldsymbol{r}',t)$ is the Fourier transform of $P(\boldsymbol{r},\boldsymbol{r}',\omega)$. Starting from the Schrödinger equation in a random potential and after disorder averaging, it is possible to demonstrate that in the limit $k_\mathrm{F}\ell_\mathrm{e} \gg 1$ and for slow variations, the probability $P(\boldsymbol{r},\boldsymbol{r}',\omega)$ defined by (6.48) is the solution of a classical diffusion equation

$$(-\mathrm{i}\omega - D\Delta)\, P_\mathrm{cl}(\boldsymbol{r},\boldsymbol{r}',\omega) = \delta(\boldsymbol{r}-\boldsymbol{r}') \tag{6.49}$$

where D stands for the diffusion coefficient defined by (6.39). Doing this, we have only considered classical contributions to the average. We will study later the corrections to this classical probability.

Conductance

Our starting point to describe electric transport is the Landauer formalism. We stay at a very qualitative level but this formalism is quite natural since it expresses the *conductance as a transmission coefficient* through the disordered sample. Consider a disordered conductor of length L and section $S = W^{d-1}$. It is connected to perfect conductors (Fig. 6.14) which can be considered as wave guides where free electronic waves propagate. In this geometry, the transverse wave vectors of the eigenmodes (also called channels) are quantized by transverse boundary conditions. One can define a transmission coefficient T_{ab} from an incoming channel a (ingoing wave vector $\boldsymbol{k}_a$) to an outgoing channel b (wave vector $\boldsymbol{k}_b$). The Landauer formula is written as

$$\mathcal{G} = s\frac{e^2}{h}\sum_{a,b} T_{ab}\,. \tag{6.50}$$

To calculate the number of transverse channels, one considers that electrons are injected at the Fermi energy, i.e. such that $|\boldsymbol{k}_a| = |\boldsymbol{k}_b| = k_\mathrm{F}$. The transverse component is quantized in units of $2\pi/W$, which imposes the number of channels. In $d = 2$ and $d = 3$, their number is given by

$$N_\perp^{(d=2)} = \frac{2\pi k_\mathrm{F}}{2\pi/W} = k_\mathrm{F}W \qquad N_\perp^{(d=3)} = \frac{\pi k_\mathrm{F}^2}{4\pi^2/W^2} = \frac{k_\mathrm{F}^2 S}{4\pi} \tag{6.51}$$

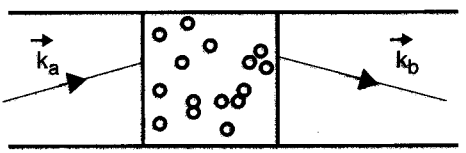

Fig. 6.14. In the Landauer formalism, the conductance is related to the transmission coefficient between different incoming and outgoing channels

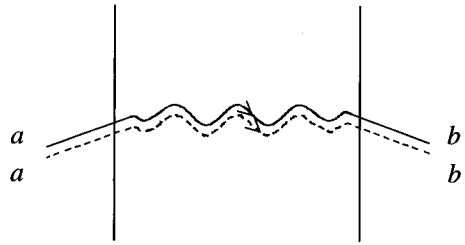

Fig. 6.15. The conductance is proportional to the classical probability to transmit a channel a to a channel b (summed over channels). The object (called diffuson) which represents this probability is the sum of contributions of paired trajectories

Now let us consider the structure of the transmission coefficient T_{ab}. It is the square of an amplitude and it has, with minor differences, the same structure as the probability $P(\boldsymbol{r}, \boldsymbol{r}', \omega)$. The main difference is the following: instead of injecting a particle at a point $\boldsymbol{r}$ inside the sample, a plane wave $\boldsymbol{k}_a$ is injected from outside the sample. In particular, the boundary conditions have to be properly treated. But, without entering into the details, it may be easily understood that, after disorder averaging, the average transmission coefficient and consequently the conductance can be related to the probability to cross the sample. More precisely for a $3d$ sample, one can show that the dimensionless conductance reads

$$g = \frac{4}{9} N_\perp v_\mathrm{F} P(0, L) \tag{6.52}$$

where $P(0, L)$ is the solution of the diffusion equation (6.49) with appropriate boundary conditions. It is given by $P(0, L) = \ell_\mathrm{e}^2 / DL$ so that

$$g = \frac{4}{3} N_\perp \frac{\ell_\mathrm{e}}{L} \tag{6.53}$$

which is equivalent to the Drude result (6.42–6.44). To obtain these results quantitatively, there are some technicalities that are not described here [18]. What should be remembered is the message of Fig. 6.15: the conductance is proportional to the classical probability to cross the sample. This is enough to understand how coherence effects appear and develop.

6.2.3 Deviations From Classical Transport: Quantum Interferences

The diffuson is a classical object. It does not depend on the phases of the complex amplitudes, and in the diffusive regime, it is the solution of a diffusion equation. However, we may have to check whether no additional effects have been left aside, when throwing out all the interference terms in relation (6.46). It turns out that some of these terms have quite interesting consequences.

Indeed, quantum effets can appear when two diffusons cross, or when a diffuson crosses with itself. The notion of quantum crossing is extremely important because it is the source of quantum effects. The diffuson being a

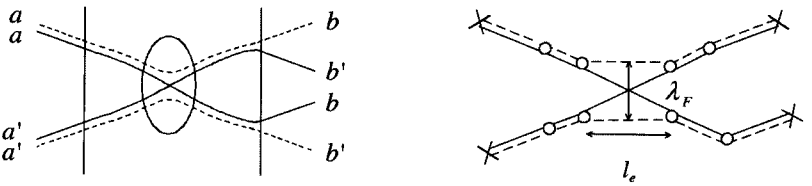

Fig. 6.16. *Left*: Crossing of two diffusons. *Right*: Detail showing that the volume of the intersection region is proportional to $\lambda_F^{d-1} l_e$

classical object, coherence effects can only appear because of these quantum crossings. They are at the origin of the weak-localization correction and of universal conductance fluctuations. Let us try to get some intuition about these crossing events.

Figure 6.16-Left illustrates that a crossing mixes four complex amplitudes which belong to two incoming diffusons and pair them differently. The two emerging diffusons are built with amplitudes A_j and $A_{j'}$ coming respectively from each of the incoming diffusons. They have the same phase since they follow the same path. The quantum crossing[3] is thus an object whose role is to permute the quantum amplitudes. It is necessarily short range, because trajectories have to be as close as possible to each other to avoid dephasing (Fig. 6.16-Right). Since it appears between two successive collisions on impurities, and since the phase mismatch between trajectories has to be smaller than 2π, one sees that the volume of this object is of order $\lambda_F^{d-1}\ell_e$.

It is important to evaluate the probability of occurrence of such quantum crossings. This probability will be a measure of the contribution of quantum effects. Since the volume of a quantum crossing is of order $\lambda_F^{d-1}\ell_e$, a diffuson propagating during a time t can be seen as an effective object of length $\mathcal{L} = v_F t$ and of 'cross-section' λ_F^{d-1}. Thus, it has a finite volume $v_F \lambda_F^{d-1} t$. The probability of crossing of two diffusons after a time dt in a volume $\Omega = L^d$ is thus proportional to the ratio between the volume of a diffuson and the volume of the system. As a result, the probability $\mathrm{d}p_\times(t)$ of the occurrence of a quantum crossing for two diffusons after a time $\mathrm{d}t$ writes

$$\mathrm{d}p_\times(t) = \frac{\lambda_F^{d-1} v_F \mathrm{d}t}{\Omega} \propto \frac{1}{g}\frac{\mathrm{d}t}{\tau_D} \tag{6.54}$$

where (6.44) has been used to introduce the dimensionless conductance g. Consider now an open system coupled to reservoirs. The time needed to travel throughout the sample is the Thouless time $\tau_D = L^2/D$. The probability of crossing during this time is given by

$$p_\times(\tau_D) = \int_0^{\tau_D} \mathrm{d}p_\times(t) = \frac{\lambda_F^{d-1} v_F \tau_D}{\Omega} \simeq \frac{1}{g}\,. \tag{6.55}$$

[3]Such a quantum crossing is often called a Hikami box.

This probability is the ratio of two volumes and it is proportional to the inverse dimensionless conductance (6.44). Thus the probability of crossing scales like $1/g$. Since, in the weak-disorder limit $k_F l_e \gg 1$, g is large, phase-coherent effects are small. The ratio $1/g$ being a small number in a metal, this explains why phase-coherent effects are weak.

There is also a very important feature to notice: when amplitudes are interchanged at a quantum crossing, the paired amplitudes belong to *different* channels. It is not at all obvious that they will stay in phase: assume that some event changes the phase of the amplitude A_j. As seen above, the complex conjugate A_j^* gets the opposite phase so that nothing happens. The same for the $A_{j'}$ and $A_{j'}^*$. However, after the crossing, since A_j and $A_{j'}^*$ follow the same path, they have the same action, except if some perturbation has changed the phase of one of them. So the new object formed after the quantum crossing looks like a diffuson but it is more *fragile*: it is sensitive to dephasing and its lifetime τ_ϕ is finite.

6.2.4 Weak Localization

We have seen that the classical probability $P(\boldsymbol{r}, \boldsymbol{r}', \omega)$ and the conductance can be expressed as a sum of contributions of pairs of complex conjugated trajectories. Since trajectories can have quantum crossings, they can form closed loops (Fig. 6.17). It turns out that in such a loop (whose contribution is not included in (6.47)), the trajectories are *time reversed*. One trajectory j and its time reversed j^T go in opposite directions. However, if there is time-reversal symmetry, they have the same action and thus they have exactly the same phase. This phase can be quite complicated because it depends on the disorder configuration but it is the same for both trajectories. The contribution of these loops do not cancel on average. If the end points are far away like in Fig. 6.17, the contribution of these new trajectories is small, of order $1/g$, but it leads to an experimentally observable effect: the weak-localization correction to the conductance. This is a phase-coherent effect because only trajectories of a size smaller than the phase coherence length L_ϕ will contribute to this additional term. Using the same type of argument as in the previous section, let us evaluate the probability to have a loop for a trajectory which travels through the sample. Since there is a quantum crossing, the probability is small, of order $1/g$. Moreover, it depends on the distribution of loops in the disordered system. Let us call it $P_{\rm int}(t)$. The probability of traversing the sample with a loop then reads

$$p_0(\tau_D) = \int_0^{\tau_D} P_{\rm int}(t)\, \mathrm{d}p_\times(t) = \frac{1}{g} \int_0^{\tau_D} P_{\rm int}(t) \frac{\mathrm{d}t}{\tau_D} \,. \tag{6.56}$$

We also have to remember that because of decoherence in the loop, only those with time t smaller that τ_ϕ contribute. The resulting probability of having trajectories with loops of time smaller than τ_ϕ is

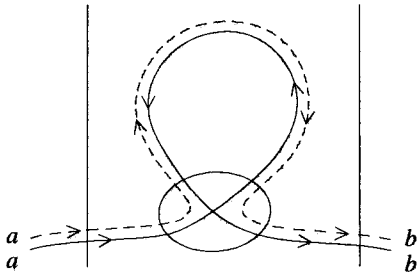

Fig. 6.17. Trajectory with a quantum crossing and a loop. In the loop, the two propagations are time reversed

$$p_0(\tau_\phi) = \int_0^{\min(\tau_D,\tau_\phi)} P_{\rm int}(t) \mathrm{d}p_\times(t) = \frac{1}{g} \int_0^{\min(\tau_D,\tau_\phi)} P_{\rm int}(t) \frac{\mathrm{d}t}{\tau_D} \tag{6.57}$$

where $P_{\rm int}(t)$ is the probability to have loops of time t. This leads to a relative correction to the conductivity (or to the conductance) given by

$$\frac{\Delta\sigma}{\sigma_0} = \frac{\Delta\mathcal{G}}{\mathcal{G}_0} = -p_0(\tau_\phi) \,. \tag{6.58}$$

The sign of the correction is negative because the trajectories j and j^T have opposite momenta. This quantum correction to the classical Drude conductivity is called the *weak-localization* correction [22,23]. The phase coherence is broken by inelastic events due to the coupling of the electrons to other degrees of freedom or due to electron-electron interactions. Such coherence breakdown is temperature dependent and can be phenomenologically described by a temperature dependent phase coherence length $L_\phi(T) = \sqrt{D\tau_\phi(T)}$: trajectories larger than L_ϕ do not contribute to the weak-localization corrections.

As we have seen above, the amplitude of the correction is proportional to $P_{\rm int}(t)$, the distribution of loops. The number of loops of time t is precisely given by the return probability, solution of the diffusion equation. We calculate this quantity in the next section. Moreover (6.57) and (6.58) have a meaning only in the diffusive regime for which $t > \tau_{\rm e}$ (otherwise a loop cannot be formed). The contribution of the return probability has thus to be integrated between $\tau_{\rm e}$, the smallest time for diffusion, and the phase coherence time τ_ϕ. Replacing the bounds by exponential cut-offs, the weak-localization correction can be cast in the form

$$\Delta\mathcal{G} = -2s\frac{e^2}{h} \int_0^\infty P_{\rm int}(t) \, (\mathrm{e}^{-t/\tau_\phi} - \mathrm{e}^{-t/\tau_{\rm e}}) \frac{\mathrm{d}t}{\tau_D} \tag{6.59}$$

In order to evaluate $\Delta\mathcal{G}$ in various situations, we now study the diffusion equation and its solutions.

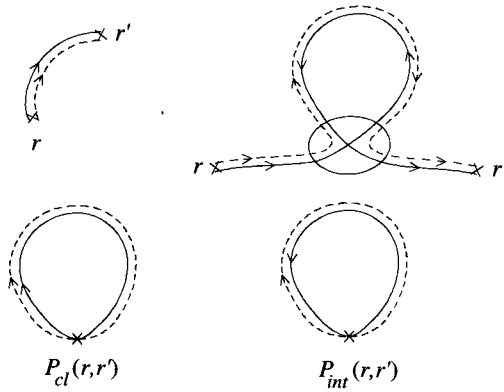

Fig. 6.18. Classical probability $P_{\rm cl}(\boldsymbol{r},\boldsymbol{r}',t)$ and the quantum correction $P_{\rm int}(\boldsymbol{r},\boldsymbol{r}',t)$. When $\boldsymbol{r}\neq\boldsymbol{r}'$, the correction is small because the probability of quantum crossing is small. When $\boldsymbol{r}=\boldsymbol{r}'$, the two contributions are equal so that the return probability is twice its classical value. The pair of time reversed trajectories is called a cooperon

6.2.5 Diffusion Equation

Explicit calculation of the probability $P_{\rm int}(t)$ requires the solution of the diffusion equation. We now open a parenthesis devoted to the derivation of some relevant solutions of this equation. As seen on Fig. 6.18, the probability $P(\boldsymbol{r},\boldsymbol{r}',t)$ has two contributions, a classical one, $P_{\rm cl}(\boldsymbol{r},\boldsymbol{r}',t)$, and a additional contribution, $P_{\rm int}(\boldsymbol{r},\boldsymbol{r}',t)$, which contains a loop. The total number of loops in (6.59) is precisely the integrated return probability

$$P_{\rm int}(t)=\int P_{\rm int}(\boldsymbol{r},\boldsymbol{r},t)\mathrm{d}\boldsymbol{r} \tag{6.60}$$

Classical Diffusion and Quantum Correction

In Sect. 6.2.2, we have seen that the classical probability has been derived as the solution of a classical diffusion equation (written here for the Fourier transform):

$$\left(\frac{\partial}{\partial t}-D\Delta\right)P_{\rm cl}(\boldsymbol{r},\boldsymbol{r}',t)=\delta(\boldsymbol{r}-\boldsymbol{r}')\delta(t)\;. \tag{6.61}$$

However, we have seen that the probability has another component which results from trajectories with loops $P_{\rm int}(\boldsymbol{r},\boldsymbol{r}',t)$. When $\boldsymbol{r}\neq\boldsymbol{r}'$ this second contribution is very small, in the order $1/g$. When $\boldsymbol{r}=\boldsymbol{r}'$, Fig. 6.18 shows that it has exactly the same structure as the classical term. Thus the return probability is *doubled*. The interference term is *not* a solution of a diffusion equation (it is negligible when $\boldsymbol{r}'\neq\boldsymbol{r}$), but can be easily calculated when $\boldsymbol{r}'=\boldsymbol{r}$. In this case, and if there is time-reversal symmetry, we have $P_{\rm int}(\boldsymbol{r},\boldsymbol{r},t)=$

$P_{\rm cl}(\boldsymbol{r},\boldsymbol{r},t)$. However $P_{\rm int}(\boldsymbol{r},\boldsymbol{r},t)$ is phase sensitive. For example, it is modified by a magnetic field. It can be shown that it obeys the following 'diffusion-like' equation [22,23]:

$$\left[\frac{1}{\tau_\phi}+\frac{\partial}{\partial t}-D\left(\nabla+\frac{2ie\boldsymbol{A}}{\hbar c}\right)^2\right]P_{\rm int}(\boldsymbol{r},\boldsymbol{r}',t)=\delta(\boldsymbol{r}-\boldsymbol{r}')\delta(t) \tag{6.62}$$

whose solution has to be taken at $\boldsymbol{r}'=\boldsymbol{r}$. The effect of the magnetic field is described by a covariant derivative where the charge coupled to the vector potential $\boldsymbol{A}$ is $-2e$. The doubling of the charge reflects the fact that the time reversed amplitudes entering $P_{\rm int}$ accumulate *opposite* phases. The scattering rate $1/\tau_\phi$ describes the breaking of phase coherence. We now consider a few solutions of (6.61) and (6.62).

Solutions of the Diffusion Equation

The discussion of physical quantities like weak-localization correction requires the solution of the diffusion equation in some simple cases. Thus a useful quantity is the space integrated (dimensionless) return probability:

$$P(t)=\int P(\boldsymbol{r},\boldsymbol{r},t)\mathrm{d}\boldsymbol{r}\ . \tag{6.63}$$

Free Diffusion

The solution of equation (6.61) in the free space of dimension d is a gaussian function. To obtain it, one starts from the Fourier transform $P(\boldsymbol{q},t)$ of (6.61) which obeys the equation

$$\left(\frac{\partial}{\partial t}+Dq^2\right)P(\boldsymbol{q},t)=\delta(t) \tag{6.64}$$

whose solution is

$$P(\boldsymbol{q},t)=\theta(t)\mathrm{e}^{-Dq^2t} \tag{6.65}$$

so that the inverse Fourier transform $P(\boldsymbol{r},\boldsymbol{r}',t)=\int\frac{\mathrm{d}\boldsymbol{q}}{(2\pi)^d}P(\boldsymbol{q},t)\mathrm{e}^{\mathrm{i}\boldsymbol{q}\cdot(\boldsymbol{r}-\boldsymbol{r}')}$ is

$$P(\boldsymbol{r},\boldsymbol{r}',t)=\frac{1}{(4\pi Dt)^{d/2}}\mathrm{e}^{-|\boldsymbol{r}-\boldsymbol{r}'|^2/4Dt} \tag{6.66}$$

As a result, the typical distance reached by diffusion after a time t is given by $\left\langle R^2(t)\right\rangle=2dDt$, and the return probability to the origin after a time t is obtained from (6.66) by taking $\boldsymbol{r}=\boldsymbol{r}'$. Precisely one gets $P(\boldsymbol{r},\boldsymbol{r},t)=1/(4\pi Dt)^{d/2}$, so that the integrated return probability $P(t)$ in a volume Ω, as defined by (6.63), is

$$P_{\rm cl}(t)=P_{\rm int}(t)=\frac{\Omega}{(4\pi Dt)^{d/2}} \tag{6.67}$$

2d Diffusion in a Magnetic Field

Consider the diffusion of an electron in a infinite plane placed in a perpendicular magnetic field B. The classical probability $P_{\rm cl}(\boldsymbol{r},\boldsymbol{r}',t)$ is not affected by the field. To obtain its effect on the interference part $P_{\rm int}(\boldsymbol{r},\boldsymbol{r},t)$, one has to solve the covariant diffusion equation (6.62). To that purpose, we first remark that $P_{\rm int}(\boldsymbol{r},\boldsymbol{r}',t)$ does not need to be calculated, but instead $P_{\rm int}(t)$. To evaluate directly this quantity, one notes that the general solution of the diffusion equation (6.62) has the form

$$P(\boldsymbol{r},\boldsymbol{r}',t)=\theta(t)\sum_n \psi_n^*(\boldsymbol{r})\psi_n(\boldsymbol{r}')\mathrm{e}^{-E_n t} \tag{6.68}$$

where $\theta(t)$ is the step function and $\{E_n,\psi_n\}$ are the eigenvalues and eigenfunctions of the eigenvalue equation associated to (6.62)

$$-D\left(\nabla_{\boldsymbol{r}}+\frac{2\mathrm{i}e\boldsymbol{A}}{\hbar c}\right)^2\psi_n(\boldsymbol{r})=E_n\psi_n(\boldsymbol{r}) \tag{6.69}$$

From (6.68), we find that the integrated probability $P(t)$ has the simple form

$$P(t)=\theta(t)\sum_n \mathrm{e}^{-E_n t} \tag{6.70}$$

This relation is quite useful to calculate $P_{\rm int}(t)$ in a magnetic field. The eigenvalues E_n are solutions of an effective Schrödinger equation for a free particle of mass $m=\hbar/2D$ and charge $-2e$ in a uniform field B. They are precisely the Landau levels, namely

$$E_n=\left(n+\frac{1}{2}\right)\frac{4eDB}{\hbar} \tag{6.71}$$

where n is an integer. The degeneracy of these levels for an area S is $g_n=\frac{2eB}{h}S$, while the integrated return probability $P_{\rm int}(t)$ is simply related to $\sum_n g_n\mathrm{e}^{-E_n t}$, that is

$$P_{\rm int}(t,B)=\frac{BS/\phi_0}{\sinh(4\pi BDt/\phi_0)} \tag{6.72}$$

where $\phi_0=h/e$ is the flux quantum. In the limit $B\to 0$, one recovers the solution of free diffusion: $S/(4\pi Dt)$. For large times, $P_{\rm int}(t,B)$ decreases exponentially with a characteristic time $\tau_B=\phi_0/4\pi BD$, which describes the dephasing of time reversed trajectories, and can be associated to a characteristic length $L_B=\sqrt{\hbar/2eB}$ (magnetic length).

Diffusion on a Ring or on a Cylinder

Consider now a ring of perimeter L pierced by an Aharonov-Bohm flux ϕ. The solution of (6.62) on such a ring is quite easy to guess. Starting from (6.66),

one sees that the return probability on a ring is the probability to return to the original point without making a loop around the ring plus the probability of return after one loop, two loops, etc. Then one should take (6.66) with $|\boldsymbol{r} - \boldsymbol{r}'| = mL$, and sum over all possible values of m. Moreover each turn around the loop accumulates a phase $2 \times 2\pi\phi/\phi_0$. We obtain

$$P_{\rm int}(t,\phi) = \frac{L}{\sqrt{4\pi Dt}} \sum_{m=-\infty}^{+\infty} {\rm e}^{-m^2L^2/4Dt} \cos 4\pi m\phi/\phi_0 \tag{6.73}$$

Each harmonic of this expansion represents the return probability after m loops around the ring. For a cylinder of height L_z, the diffusion is free along the z direction of the cylinder axis. The same argument as for the ring gives immediately

$$P_{\rm int}(t,\phi) = \frac{LL_z}{4\pi Dt} \sum_{m=-\infty}^{+\infty} {\rm e}^{-m^2L^2/4Dt} \cos 4\pi m\phi/\phi_0 \tag{6.74}$$

6.2.6 Back to Weak-Localization

The weak-localization correction is now computed in various situations.

Dependence on the Dimensionality

The weak-localization correction is proportional to the integrated return probability $P_{\rm int}(t)$. As a result it depends on space dimensionality d. Consider a sample whose typical size $L = \Omega^{1/d}$ is larger than L_ϕ. For time scales smaller than τ_ϕ, diffusion is like in an infinite medium and the return probability is given by (6.67), that is $P_{\rm int}(t) = \Omega/(4\pi Dt)^{d/2}$. Using the integral (6.94), one obtains the conductivity correction expressed in units of the quantum of conductance e^2/h, in the limit $L_\phi \gg \ell_{\rm e}$, namely for quasi-1D systems: $\Delta\mathcal{G} = -s\dfrac{e^2}{h}L_\phi$, whereas for $d = 2$ (or $d = 3$), $\Delta\mathcal{G} = -s\dfrac{e^2}{\pi h}\ln\dfrac{L_\phi}{\ell_{\rm e}}$ (or $\Delta\mathcal{G} = -s\dfrac{e^2}{2\pi h}\dfrac{L}{\ell_{\rm e}}$) [18,24]. The strictly $1D$ case is not considered here because the diffusion approximation does not apply in this case. Instead, we consider the case of a *quasi one-dimensional* wire of finite section S, in which the diffusive motion is $1D$ but which is $3d$ in the sense that its section is larger than the Fermi wavelength, so that many transverse channels are opened to conduction. Then one uses the relation (6.59) with $\Omega = LS$ and $P_{\rm int}(t) = L/\sqrt{4\pi Dt}$. The $2d$ result corresponds to a strictly $2d$ gas. For a quasi-2D system with a finite width a, the conductivity has to be divided by a.

Magnetoresistance

A very convenient way to measure the weak-localization correction is to study its magnetic field dependence. Indeed, the magnetic field breaks time-reversal

symmetry and suppresses the weak-localization correction. Since this correction is negative, its suppression leads to a increase of conductance or a negative magnetoresistance, which is amongst the most spectacular signature of weak-localization[4]. In a magnetic field, the weak-localization correction is still given by (6.59) where $P_{\rm int}(t,B)$ is the return probability in a magnetic field given by (6.72). The weak-localization correction is then

$$\Delta\mathcal{G}(B) = -2s\frac{e^2D}{h}\int_0^\infty \frac{B/\phi_0}{\sinh 4\pi BDt/\phi_0}\left(\mathrm{e}^{-t/\tau_\phi} - \mathrm{e}^{-t/\tau_{\rm e}}\right)\mathrm{d}t \tag{6.75}$$

Using (6.95), the integral gives

$$\Delta\mathcal{G}(B) = -s\frac{e^2}{2\pi h}\left[\Psi\left(\frac{1}{2}+\frac{\hbar}{4eDB\tau_{\rm e}}\right) - \Psi\left(\frac{1}{2}+\frac{\hbar}{4eDB\tau_\phi}\right)\right] \tag{6.76}$$

where $\Psi(x)$ is the digamma function. This expression involves a characteristic field B_ϕ defined by $B_\phi = \phi_0/8\pi L_\phi^2$, corresponding to one flux quantum through an area L_ϕ^2. The weak-localization correction disappears beyond this field (i.e. when the time τ_B is smaller than τ_ϕ) which is in order of 10^{-3} Tesla for $L_\phi \simeq 1\,\mu$m. The magnetoconductance $\mathcal{G}(B) - \mathcal{G}(0)$ is the difference between the weak-localization corrections $\Delta\mathcal{G}(B) - \Delta\mathcal{G}(0)$ and it is given by

$$-s\frac{e^2}{2\pi h}\left[\ln\left(\frac{\hbar}{4eDB\tau_\phi}\right) - \Psi\left(\frac{1}{2}+\frac{\hbar}{4eDB\tau_\phi}\right)\right] \tag{6.77}$$

The magnetoresistance $\Delta R(B) \propto -\Delta\mathcal{G}(B)/\mathcal{G}_0^2$ is thus *negative*. In the limit $B \ll B_\phi$, the expansion (6.96) gives

$$\Delta\mathcal{G}(B) - \Delta\mathcal{G}(0) \simeq \frac{s}{96\pi^2}\frac{e^2}{\hbar}\left(\frac{B}{B_\phi}\right)^2. \tag{6.78}$$

The field dependence of the weak-localization correction has been studied very carefully, in particular in metallic films as shown on Fig. 6.19 on a famous example [25]. It is a way commonly used to obtain a precise determination of the dependence $\tau_\phi(T)$.

Altshuler-Aronov-Spivak Oscillations on a Cylinder

One of the most famous experiments showing phase-coherence effect on transport is the one performed by Sharvin and Sharvin [26] who measured the magnetoresistance of a cylinder threaded by a magnetic flux ϕ. In this case the return probability $P_{\rm int}(t,\phi)$ is modulated by the flux through the cylinder and is given by (6.73). Using the integral (6.98), one obtains the flux dependence of the conductance $\Delta\mathcal{G}$ of the cylinder of length L_z:

[4]There is an additional contribution to the conductivity which results from electron-electron interaction. It does not depend on the magnetic field.

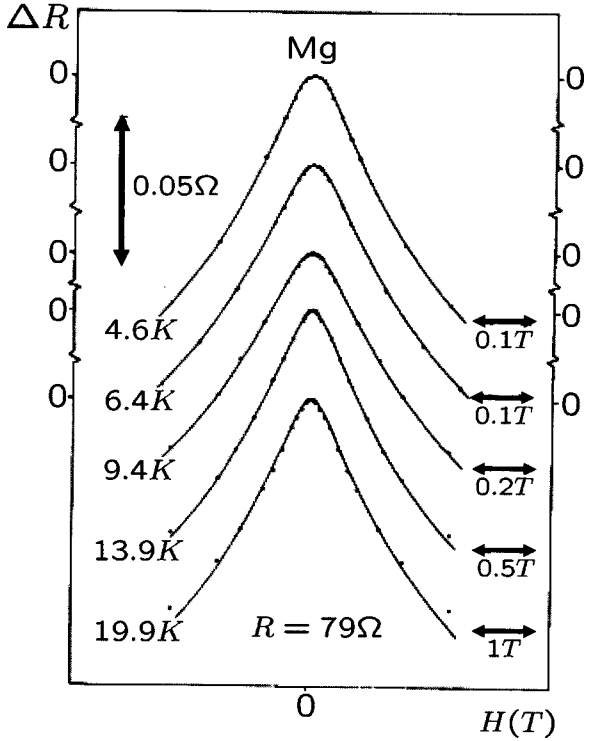

Fig. 6.19. Magnetoresistance of a Mg film, as a function of the applied field, for several temperatures. The dots are experimental data, while the curves correspond to (6.77). The time τ_ϕ is an adjustable parameter [25]

$$\Delta\mathcal{G}(\phi) = -s\frac{e^2}{\pi h}\frac{L}{L_z}\left[\ln\frac{L_\phi}{\ell_e} + 2\sum_{m=1}^{+\infty} \mathrm{K}_0(mL/L_\phi)\,\cos 4\pi m\phi/\phi_0\right] \qquad (6.79)$$

where K_0 is the modified Bessel function. The amplitude of the oscillations of period $\phi_0/2$ decreases exponentially with the perimeter L of the cylinder and becomes negligible when $L \gg L_\phi$.

These oscillations have been predicted by Altshuler, Aronov and Spivak [27]. As shown on Fig. 6.20, the agreement between theory and experiment is excellent (note the presence of negative magnetoresistance). Similar oscillations have been observed in multiwalled nanotubes (MWNT) in a parallel magnetic field [28]. This strongly suggests that the MWNT are diffusive.

6.2.7 Universal Conductance Fluctuations

Another important signature of the coherent nature of quantum transport is the phenomenon of *Universal Conductance Fluctuations* [29, 30]. When a physical parameter is varied, such as the Fermi energy, the magnetic field (Fig. 6.21) or the disorder configuration, the conductance fluctuates around its

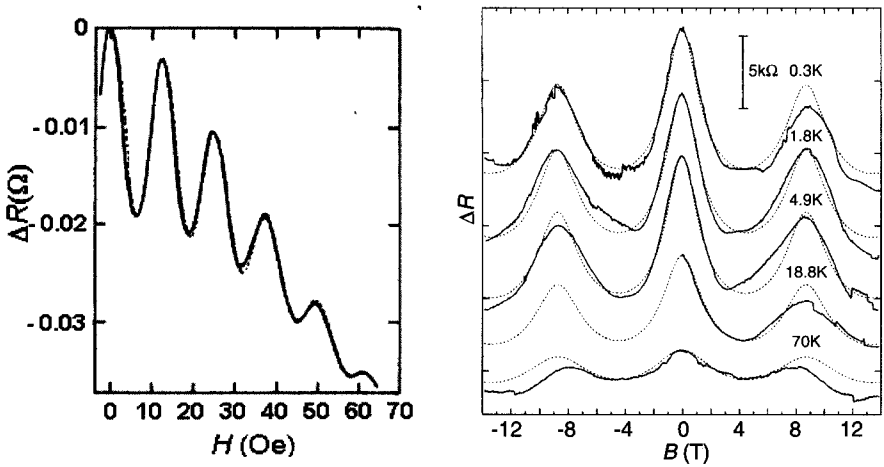

Fig. 6.20. *Left*: Magnetoresistance $\Delta R(B)$ of a lithium film on a cylinder quartz compared with (6.79) (*dashed line*) [26]. *Right*: Magnetoresistance of a MWNT in a parallel field [28]

average value. In the mesoscopic regime, these fluctuations are reproducible and provide the signature of the interference pattern associated to a given impurity configuration. The width of the distribution is universal and of the order of e^2/h [29,30]

$$\delta\mathcal{G}^2 = \langle\mathcal{G}^2\rangle - \langle\mathcal{G}\rangle^2 \sim \left(\frac{e^2}{h}\right)^2 . \tag{6.80}$$

Here we aim to understand qualitatively why the fluctuations are universal, using our picture of quantum crossings. The quantity $\delta\mathcal{G}^2$ implies the correlation between pairs of diffusive trajectories, with quantum crossings (otherwise $\delta\mathcal{G} = 0$). As each crossing has a weight $1/g$, terms with one crossing would give a correlation $\delta\mathcal{G}^2 = \mathcal{G}^2/g \propto \mathcal{G}e^2/h$. However, when summing the Landauer formula over all outgoing channels, it can be shown that the contribution with one crossing turns out to be negligible. The main contribution has *two crossings*, as shown in Fig. 6.22. The variance $\delta\mathcal{G}^2$ is thus proportional to $\mathcal{G}^2/g^2 = (e^2/h)^2$ and is therefore universal.

Let us be more precise and try to estimate the variance of the fluctuations. It is related to the probability to have two diffusons crossing the sample, with two quantum crossings. The probability $\mathrm{d}p_{\times\times}$ to have two quantum crossings in the time interval $[t, t+\mathrm{d}t]$ resembles the probability $\mathrm{d}p_0(t)$ to have a loop, because the two crossings indeed form a loop. But the relative position of the two crossings which has still to be chosen, gives an additional factor t (Fig. 6.22):

$$dp_{\times\times}(t) = \left(\frac{\lambda_{\mathrm{F}}^{d-1} v_{\mathrm{F}}}{\Omega}\right)^2 t\, P(t)\mathrm{d}t \simeq \frac{1}{g^2} P(t) \frac{t\,\mathrm{d}t}{\tau_D^2} \tag{6.81}$$

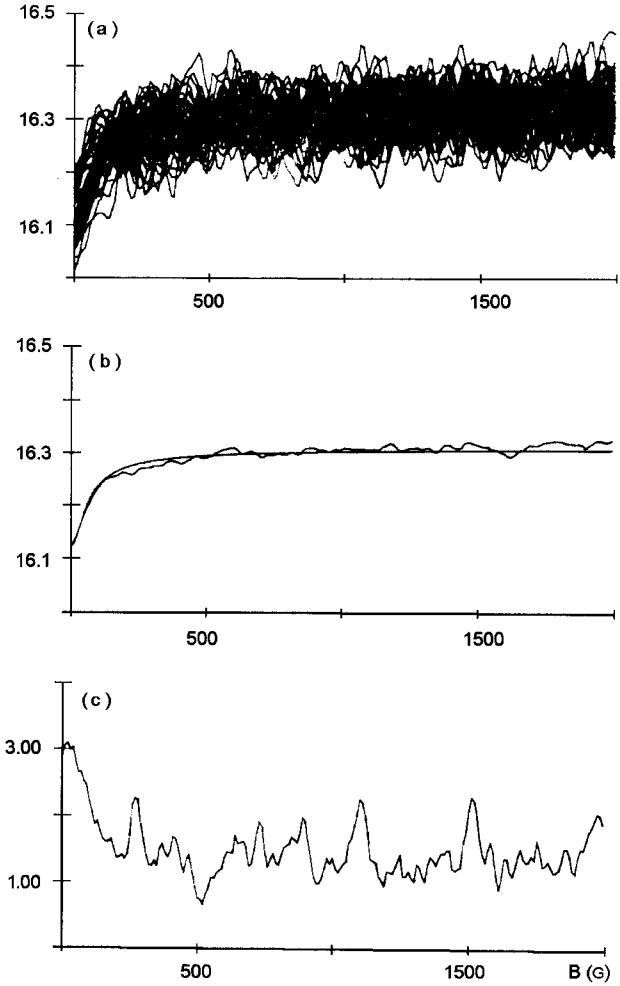

Fig. 6.21. Reproducible fluctuations of the magnetoconductance in units of e^2/h, at T = 45 mK for Si doped GaAs. Top panel shows 46 plots as function of the magnetic field, for the same sample after successive annealing. Each plot corresponds to a disorder configuration and is called a *magnetofingerprint.* Middle panel presents the average conductance versus field. The weak-localization correction disappears beyond a characteristic field. Above the same field, the variance of the fluctuations is divided by a factor 2 (*bottom panel*), corresponding to the destruction of the cooperon [31]

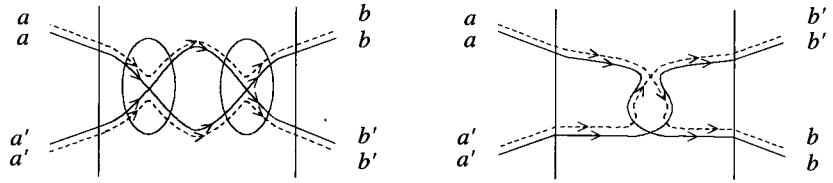

Fig. 6.22. The correlation function of the conductance implies the correlation of two diffusons, with two quantum crossings. *Left*: A contribution where the loop forms two diffusons. *Right*: A contribution where the loop forms two cooperons. The latter contribution is suppressed by a magnetic field

and the relative fluctuation is proportional to the probability of having two quantum crossings during the time τ_ϕ:

$$\frac{\delta\mathcal{G}^2}{\mathcal{G}^2} \simeq p_{\times\times}(\tau_\phi) = \frac{1}{g^2}\int_0^{\min(\tau_D,\tau_\phi)} P(t)\frac{t\mathrm{d}t}{\tau_D^2} \tag{6.82}$$

There are several ways to arrange quantum crossings (see Fig. 6.22). A careful calculation gives:

$$\delta\mathcal{G}^2 = 6s^2\left(\frac{e^2}{h}\right)^2\int_0^\infty t\,[P_{\mathrm{cl}}(t)+P_{\mathrm{int}}(t)]\mathrm{e}^{-t/\tau_\phi}\frac{\mathrm{d}t}{\tau_D^2} \tag{6.83}$$

There is an equal contribution of loops with diffusons or cooperons. In a magnetic field, the cooperon contribution is suppressed so that the variance is reduced by a factor 2, as seen on Fig. 6.21c.

Universal Conductance Fluctuations in a Quasi-1D Wire

As an example, consider a quasi-1D wire of length L connected to leads. First let us assume that the system is mesoscopic, i.e. $L \ll L_\phi$. The return probability in this case is $P_{\mathrm{int}}(t) = P_{\mathrm{cl}}(t) = \sum_q \mathrm{e}^{-Dq^2t}$ where the modes are quantized as $q = n\pi/L$, with $n > 0$. Equation (6.83) gives

$$\delta\mathcal{G}^2 = \frac{12s^2}{\pi^4}\left(\frac{e^2}{h}\right)^2\sum_{n>0}\frac{1}{n^4} \tag{6.84}$$

so that the fluctuation of the conductance is given by a universal quantity, namely independent of disorder [30]:

$$\delta\mathcal{G}^2 = \frac{2s^2}{15}\left(\frac{e^2}{h}\right)^2.$$

In the opposite limit of a macroscopic system, i.e. for $L \gg L_\phi$, $P(t)$ can be replaced by its expression (6.67) for an infinite system and one gets

$$\langle \delta \mathcal{G}^2 \rangle = 3s^2 \left(\frac{e^2}{h}\right)^2 \left(\frac{L_\phi}{L}\right)^3 .$$

In d dimensions, this result is easily generalized to obtain: $\langle \delta \mathcal{G}^2 \rangle \propto (L_\phi/L)^{4-d}$.

6.3 An Interaction Effect: the Density-of-States Anomaly

Up to now, we have neglected the interactions between electrons. In a metal the Coulomb interaction leads to modifications in some physical properties and the diffusive nature of the electronic motion plays an important role, increasing the interaction effect. This can be understood qualitatively in the following manner. The probability that two electrons interact is increased because electrons have a diffusive and not ballistic motion. The effective interaction between electrons is thus enhanced, since the probability to stay in the interaction region is increased. The change in the related physical quantities $X(E)$ at energy scale E is proportional to the time spent in the interaction region. Namely, it is proportional to the return probability in the interaction region during the time $\hbar/E$:

$$\frac{\delta X(E)}{X} \propto \frac{\lambda_F^{d-1} v_F}{\Omega} \int_0^{\hbar/E} P(t) \mathrm{d}t \, . \tag{6.85}$$

For instance, there is a correction to the conductance, of the same order as the weak-localization correction, but independent of the magnetic field, at low fields. There is also an anomaly in the density of states which can be measured by tunneling measurements. Here we briefly discuss the origin of this anomaly. To that purpose, we use the Hartree-Fock approximation (for details, see [1]). In this approximation the Schrödinger equation writes

$$\epsilon_i \phi_i(\boldsymbol{r}) = -\frac{1}{2m} \Delta \phi_i(\boldsymbol{r}) + V(\boldsymbol{r}) \phi_i(\boldsymbol{r}) - \sum_j^{\mathrm{occ}} \int U(\boldsymbol{r} - \boldsymbol{r}') \phi_j^*(\boldsymbol{r}') \phi_j(\boldsymbol{r}) \phi_i(\boldsymbol{r}') \mathrm{d}\boldsymbol{r}' \tag{6.86}$$

Here, only the exchange term are considered. $U(\boldsymbol{r}-\boldsymbol{r}')$ is the screened Coulomb potential. This non-linear equation should be solved self-consistently, but we treat it as a perturbation. First of all, we evaluate the correction to the density of states by calculating the shift of energy levels $\Delta\epsilon_i$. The average shift of a level i at energy ϵ is given by

$$\Delta\epsilon = -\sum_j^{\mathrm{occ}} \int U(\boldsymbol{r} - \boldsymbol{r}') \overline{\phi_j^*(\boldsymbol{r}') \phi_j(\boldsymbol{r}) \phi_i^*(\boldsymbol{r}) \phi_i(\boldsymbol{r}')} \mathrm{d}\boldsymbol{r} \mathrm{d}\boldsymbol{r}' \tag{6.87}$$

where $U(\boldsymbol{r})$ is the screened Coulomb interactions $U(\boldsymbol{r}) = \frac{e^2}{R} \mathrm{e}^{-\kappa R}$ with the inverse screening length κ given by $\kappa^2 = 8\pi e^2 \rho_0$. The ϕ_i are the eigenfunctions of the non-interacting Hamiltonian. One can show that the average of the

product of four wave functions can be related to the classical probability [18,32]:

$$\overline{\phi_j^*(\boldsymbol{r}')\phi_j(\boldsymbol{r})\phi_i^*(\boldsymbol{r})\phi_i(\boldsymbol{r}')} = \frac{1}{\pi\rho_0\Omega^2} P_{\rm cl}(\boldsymbol{r},\boldsymbol{r}',\epsilon-\epsilon') \tag{6.88}$$

for two levels i and j at respective energies ϵ and ϵ'. The demonstration is beyond the scope of this chapter. Replacing the sum over occupied states by an integral over energy ($\sum_j^{\rm occ} = \rho_0 \int_{-\infty}^{0} {\rm d}\epsilon'$), one finds (the origin of energies is taken at the Fermi level):

$$\Delta_\epsilon = -\frac{1}{\pi\Omega^2}\int_{-\infty}^{0} {\rm d}\epsilon' \int U(\boldsymbol{r}-\boldsymbol{r}'){\rm Re}P_{\rm cl}(\epsilon-\epsilon'){\rm d}\boldsymbol{r}{\rm d}\boldsymbol{r}' \tag{6.89}$$

The interaction term varies on a length κ^{-1} much shorter than $\ell_{\rm e}$, so that in (6.89), the spatial integration can be factorized to obtain $\int U(\boldsymbol{r}){\rm d}\boldsymbol{r} = 1/2\rho_0$, so that the average energy shift is

$$\Delta_\epsilon = -\frac{1}{2\pi\rho_0}\int_{-\infty}^{0} {\rm d}\epsilon' {\rm Re}P_{\rm cl}(\boldsymbol{r},\boldsymbol{r},\epsilon-\epsilon') \tag{6.90}$$

Since, on the average, each energy ϵ is changed into $\epsilon + \Delta_\epsilon$, the distance between two levels ϵ_1 and ϵ_2 becomes $(\epsilon_2 - \epsilon_1)\,[1 + \partial\Delta_\epsilon/\partial\epsilon]$. This shift leads to a change in the density of states given by $\frac{\delta\rho}{\rho_0} = -\frac{\partial\Delta_\epsilon}{\partial\epsilon}$ so that the correction to the density of states due to interactions is related to the return probability

$$\delta\rho(\epsilon) = -\frac{1}{2\pi}{\rm Re}P_{\rm cl}(\boldsymbol{r},\boldsymbol{r},\epsilon) = -\frac{1}{2\pi\Omega}\int_0^\infty P_{\rm cl}(t)\cos\epsilon t\ {\rm d}t \tag{6.91}$$

This correction depends on the diffusive nature of the electronic motion and therefore on the dimensionality, through the dependence $P_{\rm cl}(t)$ given by (6.67). From (6.97), one obtains

$$\delta\rho(\epsilon) \propto (d-2)\frac{\epsilon^{d/2-1}}{D^{d/2}} \qquad \text{for} \qquad d = 1,3 \tag{6.92}$$

$$\delta\rho(\epsilon) \propto \frac{1}{D}\ln\epsilon\tau_{\rm e} \qquad \text{for} \quad d = 2 \tag{6.93}$$

6.3.1 Some Useful Formulas

$$\int_0^\infty \frac{1}{t^{d/2}}({\rm e}^{-\gamma t} - {\rm e}^{-\delta t}){\rm d}t = \Gamma\left(1-\frac{d}{2}\right)[\gamma^{\frac{d}{2}-1} - \delta^{\frac{d}{2}-1}] \quad \text{for } d<4 \tag{6.94}$$

$$\frac{1}{2}\int_0^\infty \frac{{\rm e}^{-yt} - {\rm e}^{-zt}}{\sinh(t/2)}{\rm d}t = \Psi\left(z+\frac{1}{2}\right) - \Psi\left(y+\frac{1}{2}\right) \tag{6.95}$$

$$\Psi\left(\frac{1}{2}+x\right) \simeq \ln x + \frac{1}{24x^2} + \cdots \qquad \text{for} \quad x\to\infty \tag{6.96}$$

$$\int_0^\infty \frac{1}{t^{d/2}} \mathrm{e}^{-\mathrm{i}\omega t} \mathrm{d}t = \Gamma\left(1 - \frac{d}{2}\right) (\mathrm{i}\omega)^{\frac{d}{2}-1} \quad \text{for } d < 4 \tag{6.97}$$

$$\int_0^\infty \mathrm{e}^{-\frac{\beta}{x} - \frac{\gamma x}{x}} \mathrm{d}x = 2\mathrm{K}_0(2\sqrt{\beta\gamma}) \tag{6.98}$$

6.4 Theory of Quantum Transport in Nanotubes

Electronic transport in carbon nanotubes has many different manifestations, from the 1D ballistic behavior for metallic or even doped semiconducting SWNTs, to quasi-2D fingerprints in weakly disordered MWNTs. Most of the universal properties presented in Sect. 6.1 and Sect. 6.2 have been found in experiments, demonstrating the richness of the field. However, in addition to such quantum properties, common to other mesoscopic systems or nanowires, carbon nanotubes also manifest unique transport features, such as upscaling of the mean free path with nanotube diameter or anomalous conductance scaling in defect-free incommensurate MWNTs. This section is aimed at reviewing both aspects, on the basis of recent analytical or numerical results.

6.4.1 Ballistic Conduction in Single-walled and Multiwalled Carbon Nanotubes

Bandstructure and Conducting Channels

The conduction regime in nanotubes is said to be ballistic whenever the measured conductance does not scale with the system length, but rather depend on the number of available quantum channels at a given energy (Sect. 6.1.1). This occurs in case of perfect or ohmic contacts between and a metallic nanotube and metallic electrodes with similar work functions. In this regime, the electronic conductance writes

$$\mathcal{G}(E) = \frac{2e^2}{h} \times N_\perp(E)$$

with $N_\perp(E)$ is the number of channels at energy E. Band structure calculations allows to extrapolate on the expected energy-dependent conductance spectrum. For all metallic nanotubes (especially armchairs), two quantum channels are available in the vicinity of Fermi energy $E_\mathrm{F} = 0$ (for undoped tubes), resulting in $\mathcal{G}(E_\mathrm{F}) = 2\mathcal{G}_0$ (with $\mathcal{G}_0 = \frac{2e^2}{h}$ the quantum conductance) [33]. At higher energies, the conductance increases as more channels become available to conduction, but it still remains quantized. As an illustration the electronic bands and conductance of the (5,5) metallic tube are displayed on Fig. 6.23.

These values are the highest that can be expected in an experiment for such a nanotube. Usually lower values are found since transmission at the interface

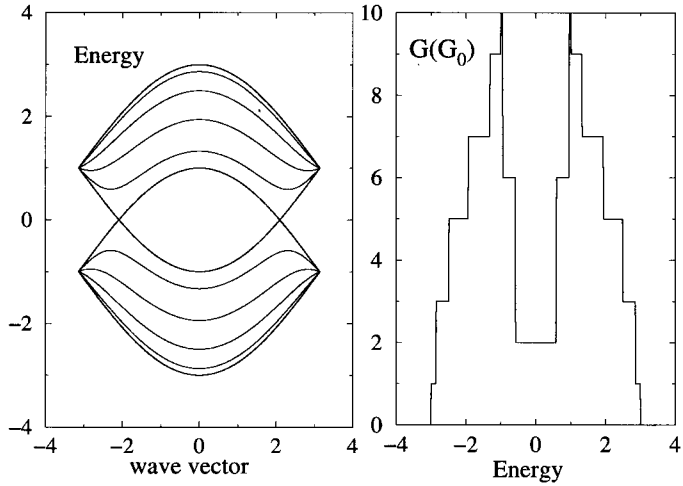

Fig. 6.23. Energy dispersion of bands (*left*) and quantum conductance as a function of energy (*right*) for the (5,5) metallic nanotube

between the voltage probes and the nanotubes are not perfectly reflectionless and partial backscattering along the tube axis (due to some topological or chemical disorder) also reduces the conductance. Generally, one introduces $T_n(E)$, the transmission amplitude for a given channel, at energy E (Landauer formula, see Sect. 6.1.1):

$$\mathcal{G}(E) = \frac{2e^2}{h} \sum_{n=1,N_\perp} T_n(E) .$$

Quantized conductance is associated with a ballistic conduction of electronic wavepackets in between voltage probe. To follow simultaneously the intrinsic conduction mechanism, together with the corresponding conductance scaling, the Kubo formulation of the problem is appropriate. The Kubo conductance of a nanotube of length $L_{\rm tube}$ can be written as [34]

$$\mathcal{G}(E, L_{\rm tube}) = \frac{2e^2}{L_{\rm tube}} \lim_{t\to\tau} {\rm Tr}[\delta(E-\mathcal{H})\hat{\mathcal{D}}(t)]$$

where $\delta(E-\mathcal{H})$ is the spectral operator (whose trace gives the density of states) and $\hat{\mathcal{D}}(t) = (\hat{\mathcal{X}}(t) - \hat{\mathcal{X}}(0))^2/t$ is the diffusion operator ($\hat{\mathcal{X}}$ is the position operator along the tube axis). The voltage-probe separation is in this case given by $L_{\rm tube}$, and τ is the associated relevant time scale that fixes the value of the conductance. In such an approach, spurious effects of the contacts are fully discarded. The ballistic regime denotes that the electronic displacement scales linearly with time. The slope of the diffusion coefficient evaluated at Fermi level $\langle\hat{\mathcal{D}}(t)\rangle_{E_{\rm F}} = (\hat{\mathcal{X}}(t) - \hat{\mathcal{X}}(0))^2/t$ gives the square of the Fermi velocity

$v_F = 3a_{cc}\gamma_0/2\hbar$ ($a_{cc} = 1.44\mathring{A}$ and $\gamma_0 = 2.7 - 2.9\,\mathrm{eV}$). In the previous formula, with $L_{tube} = v_F\tau$, a linear time scaling of the diffusion coefficient is found, i.e. $\mathcal{D}(t) \simeq v_F^2 t$, and owing to the value of the density of states is $N_\perp/2\pi\hbar v_F$, the conductance is then recovered to be length independent

$$\mathcal{G} = 2N_\perp e^2/h$$

The Kubo formula thus enables to demonstrate directly that the ballistic regime yields quantization of electronic conductance whenever metal-nanotube contacts are reflectionless.

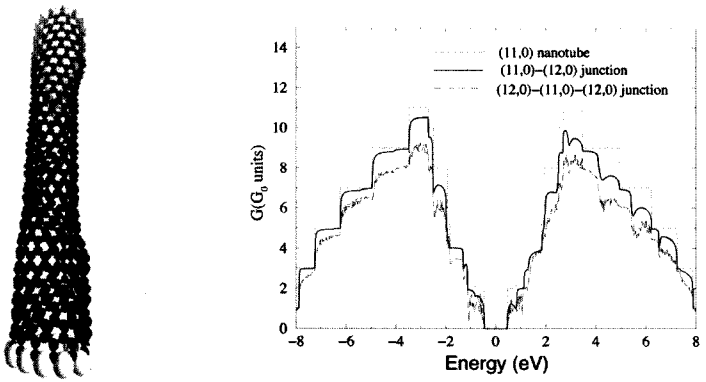

Fig. 6.24. *Left*: Illustration of a nanotube-based metal (12,0)-semiconductor (11,0)-metal (12,0) heterojunction. *Right*: Corresponding conductance spectra for the single nanotube (11,0) showing the exact number of conduction channels, together with the conductance of the double-junction (12,0)-(11,0)-(12,0)

One should note that in most cases, the contact effects yield lowering of the transmission coefficient across the interface. Indeed, even in the most favorable case, as shown in Fig. 6.24 for a nanotube based heterojunction, the symmetry mismatch between electronic states of nanotubes with different helicities reduces the transmission probability [35]. This is general to all realistic nanoscale junction between a nanotube and a metallic electrode.

6.4.2 Effects of Disorder and Doping

Conduction Regimes

To account for the effect of disorder on electronic transport of carbon nanotubes one must first notice that there is a subtle change of conduction dimensionality as the diameter of individual shells or the number of inner shells is increased. A typical instance is to consider a single vacancy (removing one carbon atom within the unit cell) and study its effect on the conductance pattern. For a (4,4) tube, a tight-binding simulation (or an effective

mass description) finds a broad dip around the charge neutrality point, which corresponds to a transition from two to one quantum channels [36]. As the diameter of the tube is increased the dip is narrowed until the modification of conductance with energy becomes single valued. This corresponds to a change of dimensionality. Whenever disorder within the tube (topological, dopants, ...) is encountered, the conduction regime departs from the ballistic regime. In the coherent regime, the presence of disorder produces elastic scattering which eventually yield a *diffusive regime*. Expressed in our language, the diffusive regime is related to a saturation of the diffusion coefficient of electronic wavepackets

$$\mathcal{D}(t \geq \tau_e) = \ell_e v_F$$

where the mean free path ℓ_e is introduced, while τ_e is the corresponding elastic mean free time ($\tau_e = \ell_e / v_F$). The conductance in the diffusive regime thus writes $\mathcal{G} \simeq N_\perp e^2/h(\ell_e/L_{\text{tube}})$(see Sect. 6.2.2). Such a formula, however, completely neglects quantum interferences that produce localization, and yield an exponential decrease of the conductance $\mathcal{G}(L_{\text{tube}}) = (h/2N_\perp e^2)\exp(\xi/L_{\text{tube}})$, as soon as $L_{\text{tube}} \geq \xi \sim N_\perp \ell_e$ (ξ: localization length).

In this section we address separately, the demonstration of suppression of backscattering in the energy window close to Fermi level, inferred from the particular symmetries of eigenstates. An analytical expression of the elastic mean free path is then derived within the Fermi golden rule and for diagonal Anderson-type disorder, an expression that is further extrapolated for a chemical disorder given by a concentration of impurities (such as boron or nitrogen). The effect of quantum interferences is finally addressed through the study of Aharonov-Bohm oscillations of the magnetoresistance.

6.4.3 Absence of Backscattering in Undoped Nanotubes

The symmetry of eigenstates of graphite or metallic nanotubes close to the Fermi level is very peculiar in the sense that under certain circumstances complete suppression of elastic backscattering is found. The original demonstration of this property for carbon nanotubes is due to Ando and coworkers [37]. First, one remembers that the eigenvalues at a $\boldsymbol{k}$ point in graphite or in carbon nanotubes, are written in a general way as $E(\boldsymbol{k}) = \pm\gamma_0\sqrt{3 + 2\cos(\boldsymbol{k}.\boldsymbol{a}_1) + 2\cos(\boldsymbol{k}.\boldsymbol{a}_2) + 2\cos(\boldsymbol{k}.(\boldsymbol{a}_1 - \boldsymbol{a}_2))}$. At the corners of the Brillouin zones, i.e. at the $\boldsymbol{K}$-points, one gets $E(\boldsymbol{K}) = 0$ with two degenerate eigenvectors (graphite or metallic tubes)

$$\Psi_{\boldsymbol{K},s}(\boldsymbol{r}) = \sum_{\boldsymbol{\ell}\ \text{all cells}} \frac{e^{i\boldsymbol{K}.\boldsymbol{\ell}}}{\sqrt{2}}(p_z(\boldsymbol{r} - \boldsymbol{r}_A) + p_z(\boldsymbol{r} - \boldsymbol{r}_B)) \quad \text{bonding state} \quad |\boldsymbol{K}_+\rangle$$

$$\Psi_{\boldsymbol{K},a}(\boldsymbol{r}) = \sum_{\boldsymbol{\ell}} \frac{e^{i\boldsymbol{K}.\boldsymbol{\ell}}}{\sqrt{2}}(p_z(\boldsymbol{r} - \boldsymbol{r}_A) - p_z(\boldsymbol{r} - \boldsymbol{r}_B)) \text{ antibonding state} \quad |\boldsymbol{K}_-\rangle$$

Exactly at these $\boldsymbol{K}$-points, one can estimate the amplitude of a scattering event from a state $|\boldsymbol{K}_+\rangle$ to a state $|\boldsymbol{K}_-\rangle$ as

$$\begin{aligned}\langle \boldsymbol{K}_+ \mid \hat{\mathcal{U}} \mid \boldsymbol{K}_- \rangle &= \int \mathrm{d}\boldsymbol{r}\mathrm{d}\boldsymbol{r}' \langle \boldsymbol{K}_+ \mid \boldsymbol{r}\rangle \mathcal{U}(\boldsymbol{r},\boldsymbol{r}')\langle \boldsymbol{r}' \mid \boldsymbol{K}_-\rangle \\ &= \int \mathrm{d}\boldsymbol{r}\mathrm{d}\boldsymbol{r}' \langle \boldsymbol{K}_+ \mid \boldsymbol{r}\rangle (u_A \delta(\boldsymbol{r}-\boldsymbol{r}_A) + u_B \delta(\boldsymbol{r}-\boldsymbol{r}_B))\langle \boldsymbol{r}' \mid \boldsymbol{K}_-\rangle \\ &= \frac{1}{2}\Big(u_A\{(p_z^{A^*} + p_z^{B^*})p_z^B\} + u_B\{(p_z^{A^*} + p_z^{B^*})(-p_z^B)\}\Big) \\ &= \frac{1}{2}(u_A - u_B)\,.\end{aligned}$$

From this calculation one sees that if the disorder potential is long-ranged with respect to the unit cell, i.e $u_A \simeq u_B$ (conservation of pseudospin symmetry), the term $\langle \boldsymbol{K}_+ \mid \mathcal{U} \mid \boldsymbol{K}_-\rangle = 0$, which means a disappearance of backscattering. One can extend this special property to the low-energy range by considering the eigenstates in the vicinity of $\boldsymbol{K}$-points. Around some $\boldsymbol{k}$ point, the wavefunction can be written as $\Psi(\boldsymbol{k},\boldsymbol{r}) = c_A(\boldsymbol{k})\tilde{p}_z^A(\boldsymbol{k},\boldsymbol{r}) + c_B(\boldsymbol{k})\tilde{p}_z^B(\boldsymbol{k},\boldsymbol{r})$ with

$$\tilde{p}_z^A(\boldsymbol{k},\boldsymbol{r}) = \frac{1}{\sqrt{N_{\text{cells}}}}\sum_{\boldsymbol{\ell}} \mathrm{e}^{\mathrm{i}\boldsymbol{k}.\boldsymbol{\ell}} p_z(\boldsymbol{r}-\boldsymbol{r}_A-\boldsymbol{\ell})$$

$$\tilde{p}_z^B(\boldsymbol{k},\boldsymbol{r}) = \frac{1}{\sqrt{N_{\text{cells}}}}\sum_{\boldsymbol{\ell}} \mathrm{e}^{\mathrm{i}\boldsymbol{k}.\boldsymbol{\ell}} p_z(\boldsymbol{r}-\boldsymbol{r}_B-\boldsymbol{\ell})$$

One then has to compute in particular the factors

$$\mathcal{H}_{AA}(\boldsymbol{k}) = \frac{1}{N_{\text{cells}}}\sum_{\boldsymbol{\ell},\boldsymbol{\ell}'} \mathrm{e}^{\mathrm{i}\boldsymbol{k}.(\boldsymbol{\ell}-\boldsymbol{\ell}')}\langle p_z^{A,\boldsymbol{\ell}} \mid \mathcal{H} \mid p_z^{A,\boldsymbol{\ell}'}\rangle$$

$$\mathcal{H}_{AB}(\boldsymbol{k}) = \frac{1}{N_{\text{cells}}}\sum_{\boldsymbol{\ell},\boldsymbol{\ell}'} \mathrm{e}^{\mathrm{i}\boldsymbol{k}.(\boldsymbol{\ell}-\boldsymbol{\ell}')}\langle p_z^{A,\boldsymbol{\ell}} \mid \mathcal{H} \mid p_z^{B,\boldsymbol{\ell}'}\rangle$$

It is readily shown that for instance (following the definitions of Fig. 6.25)

$$\begin{aligned}\mathcal{H}_{AB}(\boldsymbol{k}) &= \langle p_z^{A,0}|\mathcal{H}|p_z^{B,0}\rangle + \mathrm{e}^{-\mathrm{i}\boldsymbol{k}.\boldsymbol{a}_1}\langle p_z^{A,0}|\mathcal{H}|p_z^{B,-\boldsymbol{a}_1}\rangle + \mathrm{e}^{-\mathrm{i}\boldsymbol{k}.\boldsymbol{a}_2}\langle p_z^{A,0}|\mathcal{H}|p_z^{B,-\boldsymbol{a}_2}\rangle \\ &= -\gamma_0\alpha(\boldsymbol{k})\end{aligned}$$

in other terms

$$\begin{pmatrix} E(\boldsymbol{k}) & -\gamma_0\alpha(\boldsymbol{k}) \\ -\gamma_0\alpha(\boldsymbol{k}) & E(\boldsymbol{k})\end{pmatrix}\begin{pmatrix} b_1 \\ b_2\end{pmatrix} = 0$$

with $\alpha(\boldsymbol{k}) = 1 + \mathrm{e}^{-\mathrm{i}\boldsymbol{k}.\boldsymbol{a}_1} + \mathrm{e}^{-\mathrm{i}\boldsymbol{k}.\boldsymbol{a}_2}$ and $\boldsymbol{k} = \boldsymbol{K} + \delta\boldsymbol{k}$ ($\boldsymbol{K} = (4\pi/(3\sqrt{3}a_{cc}), 0)$). One obtains $\alpha(\boldsymbol{k}) = 1 + \mathrm{e}^{-2\mathrm{i}\pi/3}\mathrm{e}^{-\mathrm{i}\delta k_x a/2} + \mathrm{e}^{2\mathrm{i}\pi/3}\mathrm{e}^{-\mathrm{i}\delta k_y a/2}$ and the problem is recast to

$$\begin{pmatrix} E(\delta\boldsymbol{k}) & \frac{3\gamma_0 a_{cc}}{2}(\delta k_x + \mathrm{i}\delta k_y) \\ \frac{3\gamma_0 a_{cc}}{2}(\delta k_x - \mathrm{i}\delta k_y) & E(\delta\boldsymbol{k})\end{pmatrix}\begin{pmatrix} b_1 \\ b_2\end{pmatrix} = 0$$

Thus the expansion around the $\boldsymbol{K}$-points yields some particular linear dispersion relation given by $E(\delta k) = \pm\hbar v_{\mathrm{F}}|\delta\boldsymbol{k}|$, and since $b_1^2(\delta k_x - \mathrm{i}\delta k_y) = b_2^2(\delta k_x + \mathrm{i}\delta k_y)$, the corresponding eigenstates can be rewritten as

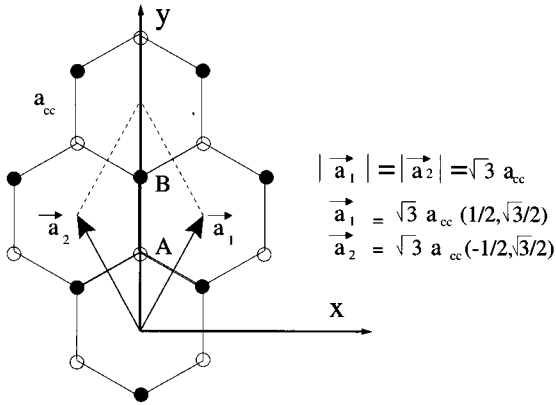

Fig. 6.25. Representation of graphite lattice vector basis

$$\Psi_{nsk}(\boldsymbol{r}) = \langle \boldsymbol{r} | n, s, \boldsymbol{k} \rangle = \frac{1}{\sqrt{2L_{\text{tube}}|\boldsymbol{C}_h|}} \begin{pmatrix} \mathrm{e}^{-\mathrm{i}\theta_k} \\ s \end{pmatrix} \mathrm{e}^{\mathrm{i}(\kappa(n)x + ky)} \tag{6.99}$$

taking $\delta k_x + \mathrm{i}\delta k_y = \kappa(n) + \mathrm{i}k = |\delta k| \mathrm{e}^{\mathrm{i}\theta_k}$ ($\theta_k = \arctan(\delta k_y / \delta k_x)$, $\kappa(n) = 2n\pi/|\boldsymbol{C}_h|$) and by setting the proper normalization factors (e.g. for a nanotube with length L_{tube} and helical vector $\boldsymbol{C}_h$). To finally estimate the intensity of backscattering in the vicinity of Fermi level, one needs to compute the scattering matrix $\langle n = 0, s, -k \mid \hat{T} \mid n = 0, s, +k \rangle$ with $\hat{T} = \hat{\mathcal{U}} + \hat{\mathcal{U}}\hat{\mathcal{G}}_0\hat{\mathcal{U}} + \hat{\mathcal{U}}\hat{\mathcal{G}}_0\hat{\mathcal{U}}\hat{\mathcal{G}}_0\hat{\mathcal{U}} + \ldots$

$$= \hat{\mathcal{U}} + \hat{\mathcal{U}}\frac{1}{E - \mathcal{H}_0}\hat{\mathcal{U}} + \hat{\mathcal{U}}\frac{1}{E - \mathcal{H}_0}\hat{\mathcal{U}}\frac{1}{E - \mathcal{H}_0}\hat{\mathcal{U}} + \ldots .$$

By virtue of

$$\begin{aligned} \frac{1}{E - \mathcal{H}_0 - \hat{\mathcal{U}}} &= \frac{1}{E - \mathcal{H}_0}\left(1 - \frac{\hat{\mathcal{U}}}{E - \mathcal{H}_0}\right)^{-1} \\ &= \mathcal{G}_0\left(1 + \frac{\hat{\mathcal{U}}}{E - \mathcal{H}_0} + \left(\frac{\hat{\mathcal{U}}}{E - \mathcal{H}_0}\right)^2 + \ldots\right) \end{aligned}$$

and by developing $\langle n, s, -k \mid \hat{T} \mid n, s, +k \rangle$ on the basis of eigenstates one is left with

$$\begin{aligned} \langle n', s', k' \mid \hat{\mathcal{U}} \mid n, s, k \rangle &= \frac{1}{\sqrt{2L_{\text{tube}}|\boldsymbol{C}_h|}}\ \mathcal{U}_{n-n'}(k - k')\left(\mathrm{e}^{\mathrm{i}\theta_k}, s\right)\begin{pmatrix} \mathrm{e}^{-\mathrm{i}\theta_{k'}} \\ s' \end{pmatrix} \\ &= \frac{1}{\sqrt{2L_{\text{tube}}|\boldsymbol{C}_h|}}\ \mathcal{U}_{n-n'}(k - k')(\mathrm{e}^{\mathrm{i}(\theta_k - \theta_{k'})} + ss') \,. \end{aligned} \tag{6.100}$$

If one considers the backscattering event for states on the same band close to Fermi energy ($E = E(\boldsymbol{k} = \boldsymbol{K}) = 0$), and further assuming that the disorder

potential is a sufficiently smooth function of space (long range potential that prohibits interband scattering), one thus gets

$$\langle 0, s, k \mid \hat{\mathcal{U}} \mid 0, s, -k \rangle = \mathcal{U}_0(2k)(\mathrm{e}^{\mathrm{i}(\theta_k - \theta_{-k})} + 1) = \mathcal{U}_0(2k)(\mathrm{e}^{\mathrm{i}\pi} + 1) = 0$$

This is also readily generalized to higher order terms, i.e. $\langle 0, s, -k \mid \hat{\mathcal{T}}(E)^p \mid 0, s, +k \rangle =$

$$\frac{1}{(\sqrt{2L_{\mathrm{tube}}C_h})^p} \sum_{s_1 k_1} \sum_{s_2 k_2} \cdots \sum_{s_p k_p} \frac{\mathcal{U}_0(-k - k_p)\mathcal{U}_0(k_p - k_{p-1}) \ldots \mathcal{U}_0(k_p - k)}{(E - \varepsilon_{s_p}(k_p))(E - \varepsilon_{s_{p-1}}(k_{p-1})) \ldots (E - \varepsilon_{s_1}(k_1))}$$

$$\times \langle s|\mathcal{R}[\theta_{-k}]\mathcal{R}^{-1}[\theta_{k_p}]|s_p\rangle \langle s_{p-1}|\mathcal{R}[\theta_{k_p}][\mathcal{R}^{-1}[\theta_{k_{p-1}}]|s_{p-1}\rangle \ldots \langle s_1|\mathcal{R}[\theta_{k_1}]\mathcal{R}^{-1}[\theta_k]|s\rangle$$

where the rotation matrix $\mathcal{R}[\theta_{k_p}]$ is defined as

$$\mathcal{R}[\theta_{k_p}] = \begin{pmatrix} \mathrm{e}^{\mathrm{i}\theta_{k_p}/2} & 0 \\ 0 & \mathrm{e}^{-\mathrm{i}\theta_{k_p}/2} \end{pmatrix}. \tag{6.101}$$

According to the symmetries of eigenstates, the product reduces to: $\langle s|\mathcal{R}[\theta_k]\mathcal{R}^{-1}[\theta_{-k}]|s\rangle = \cos(\frac{\theta_k - \theta_{-k}}{2}) = 0$. Thus to all orders the backscattering is suppressed in the low-energy range around the charge neutrality point for metallic nanotubes. The applicability of such result is, however, restricted to long-range disorder and for energy windows that shrink to zero around the charge neutrality point as the diameter of metallic tubes increases. For a more general and realistic description of disorder, a study of the mean free path within the Fermi golden rule, as described hereafter, is necessary.

6.4.4 Nature of Disorder and Defects

Disorder in carbon nanotubes can be classified into two main categories. First, topological defects that change the coordination number of a finite number of carbon atoms yield undoped disordered tubes. Vacancies have been widely studied [36,38,39], as well as heptagon-pentagon pair (or Stone-Wales) defects [40] that might additionally bridge nanotubes with different helicities [41]. If n_c is the density of such defects randomly distributed within the tube, it is expected that at small concentration, the mean free path would roughly scale as $\ell_e \sim 1/n_c$. Accounting for such defects in a tight-binding description requires a careful geometrical parametrization of the Hamiltonian energetics. Ab-initio calculations predict that the effect of a single vacancy, in a short metallic tube connected to reflectionless contacts, is likely to produce a dip in the conductance spectra roughly at $-0.4\,\mathrm{eV}$ away from the Fermi level (charge neutrality point). The second kind of defects are *substitutional impurities*. In particular, chemical substitutions of carbon atom by boron (B) or nitrogen (N) atoms have been demonstrated. These impurities introduce random scattering inside the nanotube but also produce charge transfer to

or from the tube, resulting in a shift of the position of Fermi level. Semiconducting tubes may thus become either p-doped (B) or n-doped (N), if their diameters are sufficiently large to allow small enough bandgaps.

To mimick a substitution of C by N, one can consider the defect strength as the energy difference between respective $p_\perp$-orbital. For instance $\Delta\varepsilon_{\rm CN} = \varepsilon_{p_\perp}({\rm Carbon}) - \varepsilon_{p_\perp}({\rm Nitrogen}) = -2.5\,{\rm eV}$ whereas $\Delta\varepsilon_{\rm CB} = 2.33\,{\rm eV}$.

Within a tight-binding implementation, one can establish a mapping between the parameters for the Anderson-type disorder and a more realistic description of substitutional impurities (characterized by their disorder strength and probability $\mathcal{P}$). Both disorder descriptions can be related through their distribution function defined through a common variance $\sigma_\varepsilon \sim \sqrt{\mathcal{P}(1-\mathcal{P})}|\Delta\varepsilon_{\rm CN}| = W/2\sqrt{3}$. This gives us a mapping between a random site-energy modulation of strength W and a disorder defined by a certain scattering strength ($\Delta\varepsilon_{\rm CN}$ or $\Delta\varepsilon_{\rm CB}$) and by a given density of chemical substitutions ($n_c \sim \mathcal{P}$).

6.4.5 Elastic Mean Free Path

Derivation Within the Fermi Golden Rule

Under the approximation of weak disorder, one can treat disorder effects perturbatively and write down the Fermi golden rule (FGR) for a qualitative estimation of the mean free path $\ell_{\rm e} = v_{\rm F}\tau$. First, one must derive the total density of states (TDOS) in the vicinity of Fermi level. Generally the TDOS writes $\rho(E) = {\rm Tr}[\delta(E-\mathcal{H})]$ where the trace has to be developed over a complete basis set. Assuming that the spectrum is structured by eigenstates $|\Psi_n(k)\rangle$ corresponding to eigenvalues $\varepsilon_n(k)$, one thus rewrites (note that the k_n are defined by $E - E(k_n) = 0$)

$$\rho(E) = \frac{2}{\Omega}\sum_n \int {\rm d}k \delta(E-\varepsilon_n(k)) = \frac{2}{\Omega}\sum_n \int {\rm d}k \delta(k-k_n) \times \left|\frac{\partial\varepsilon_n(k)}{\partial k}\right|^{-1}$$

with $\Omega = (8\pi^2/a^2\sqrt{3})/(2\pi|\mathcal{C}_h|^{-1}) = 4\pi|\mathcal{C}_h|/\sqrt{3}a^2$ is the volume of k-space per allowed value divided by the spacing between lines. The TDOS per carbon atom is finally expressed as [42]:

$$\rho(E_{\rm F}) = \frac{2\sqrt{3}a_{\rm cc}}{\pi\gamma_0|\mathcal{C}_h|}$$

Therefore, the application of the FGR yields

$$\frac{1}{2\tau_{\rm e}(E_{\rm F})} = \frac{2\pi}{\hbar}\left|\langle\Psi_{n1}(k_{\rm F})|\,\hat{\mathcal{U}}\,|\Psi_{n2}(-k_{\rm F})\rangle\right|^2 \rho(E_{\rm F}) \times N_{\rm c}N_{\rm Ring}$$

with $N_{\rm c}$ and $N_{\rm Ring}$, the respective number of pair atoms along the circumference and the total number of rings taken in the unit cell used for diagonalization. On the other hand, the eigenstates at the Fermi level can be written as

$$| \Psi_{n1,n2}(k_F)\rangle = \frac{1}{\sqrt{N_{\rm Ring}}} \sum_{m=1,N_{\rm Ring}} e^{imk_F} \mid \alpha_{n1,n2}(m)\rangle$$

and with

$$\begin{aligned} | \alpha_{n1}(m)\rangle &= \frac{1}{\sqrt{2N_c}} \sum_{n=1}^{N_c} e^{\frac{2i\pi n}{N_c}} \left(| p_\perp^A(mn)\rangle + | p_\perp^B(mn)\rangle \right) \\ | \alpha_{n2}(m)\rangle &= \frac{1}{\sqrt{2N_c}} \sum_{n=1}^{N_c} e^{\frac{2i\pi n}{N_c}} \left(| p_\perp^A(mn)\rangle - | p_\perp^B(mn)\rangle \right) \end{aligned} \qquad (6.102)$$

while the disorder considered here is an uncorrelated white noise distribution given by

$$\begin{aligned} \langle p_\perp^A(mn) \mid \hat{\mathcal{U}} \mid p_\perp^A(m'n')\rangle &= \varepsilon_A(\text{random}, m, n)\delta_{mm'}\delta_{nn'} \\ \langle p_\perp^B(mn) \mid \hat{\mathcal{U}} \mid p_\perp^b(m'n')\rangle &= \varepsilon_B(\text{random}, m, n)\delta_{mm'}\delta_{nn'} \\ \langle p_\perp^A(mn) \mid \hat{\mathcal{U}} \mid p_\perp^A(m'n')\rangle &= 0 \end{aligned} \qquad (6.103)$$

where $\varepsilon_B(\text{random}, m, n)$ and $\varepsilon_A(\text{random}, m, n)$ are the site energies of electron at atoms A and B in position (m, n), randomly distributed within the interval $[-W/2, W/2]$ following uniform distribution with probability $\mathcal{P} = 1/W$. By replacing such expressions of eigenstates in the previous form for elastic scattering time, one finds

$$\frac{1}{2\tau_e(E_F)} = \frac{2\pi}{\hbar}\frac{1}{4}\left(\frac{1}{\sqrt{N_c N_{\rm Ring}}} \sum_{N_c N_{\rm Ring}} \varepsilon_A^2 + \frac{1}{\sqrt{N_c N_{\rm Ring}}} \sum_{N_c N_{\rm Ring}} \varepsilon_B^2 \right) \rho(E_F)$$

Thus if the disorder is described by random fluctuations of site energies with uniform probability $1/W$, with W the disorder bandwidth, the mean free path can be finally analytically derived as [43,44]

$$\ell_e = \frac{18 a_{cc} \gamma_0^2}{W^2} \sqrt{n^2 + m^2 + nm} \qquad (6.104)$$

For a metallic nanotube ($N_T = 5, N_T = 5$), with $W = 0.2\gamma_0$ one finds $\ell_e \sim 560\,\text{nm}$ which is much more larger than the circumference length. As shown in Fig. 6.26, numerical studies confirm the scaling law of the mean free path with the nanotube diameter close to the charge neutrality point. For semiconducting bands, the $1/W^2$ is still satisfied, but mean free paths are seen to be much smaller and do not scale with diameter [45].

In the work of Liu et al. [46], the electronic transport of boron-doped nanotubes has been investigated experimentally. The concentration of boron atoms with respect to carbon atoms was evaluated to be $\simeq 1\%$ whereas the diameters of tubes were estimated in the range [17 nm, 27 nm] and mean free paths in the order of $\ell_e = 220 - 250\,\text{nm}$ were inferred from weak-localization theory. Applying (6.104) with the corresponding parameters, one finds a theoretical estimate of $\ell_e \simeq 274\,\text{nm}$ for the tube with diameter 17 nm, in agreement

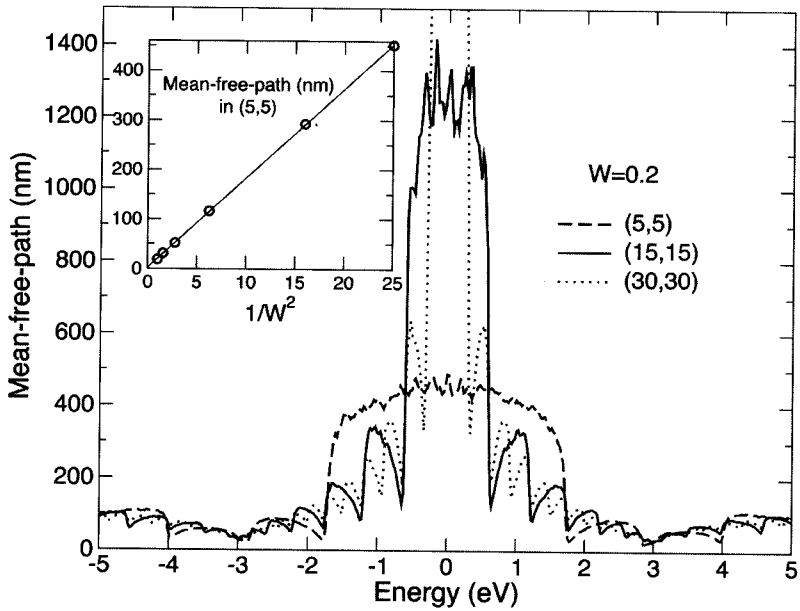

Fig. 6.26. Main frame: Energy dependent mean free path as a function of diameter. Inset: $1/W^2$-scaling in agreement with the Fermi golden rule. Adapted from [45]

with experimental estimates. Ab-initio calculations can be also very useful to address the quantitative effect of chemical impurities on both charge transfer and elastic scattering in long nanotubes. In Fig. 6.27, the mean free path for long metallic nanotubes doped with boron is reported as a function of doping level and diameters, at Fermi energy. The FGR and mean free path increase with tube diameter are correctly reproduced [39].

In low-dimensional systems, the relation between the mean free path and the localization length is an interesting problem. Thouless [56] was the first to derive a simple relation $\xi = 2\ell_e$ between both quantities in strictly 1D systems, further noticing that in quantum wires with higher number of conducting channels $N_\perp$, $\xi \sim N_\perp \ell_e$ [57]. In metallic carbon nanotubes at E_F, one thus expects to have a localization length given by $\xi = \frac{36 a_{cc} \gamma_0^2}{W^2} \sqrt{n^2 + m^2 + nm}$ that also scales linearly with the tube diameter for low disorder.

6.4.6 Quantum Interference Effects and Magnetotransport

Applying a magnetic field is a powerful tool to unveil quantum interferences effects as detailed in Sect. 6.2.4. In the presence of elastic disorder, the weak-localization scheme can be illustrated for metallic nanotube. The magnetoresistance depends on the probability $\mathcal{P}$ for an electronic wavepacket to go from one site $|P\rangle$ to another $|Q\rangle$, which can be written as

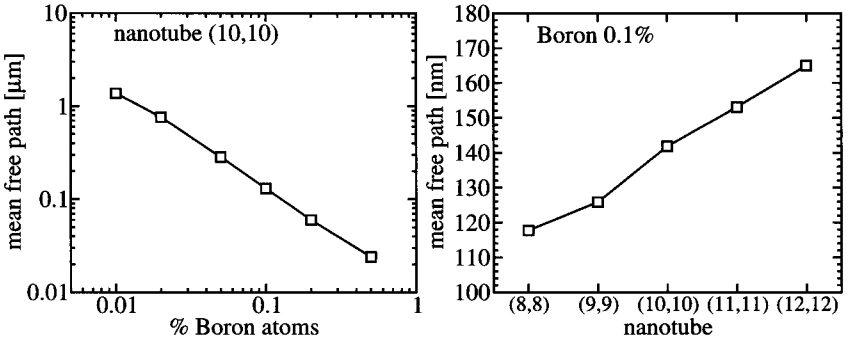

Fig. 6.27. Scaling of the mean free path at Fermi level, for a B-doped (n,n) nanotube. *Left*: in the case of a (10,10) nanotube with various boron concentrations, ℓ_e behaves like the inverse of the doping rate. *Right*: for a fixed concentration of B atoms, ℓ_e is a linear function of the nanotube's diameter

$$\mathcal{P}_{|P\rangle\to|Q\rangle} = \sum_i |\,\mathcal{A}_i\,|^2 + \sum_{i\neq j} \mathcal{A}_i\mathcal{A}_j e^{i(\alpha_i-\alpha_j)}$$

with $\mathcal{A}_i e^{i\alpha_i}$ the probability amplitude to go from $|P\rangle$ to $|Q\rangle$ via the i-path. Most of those terms, when averaged over disorder, vanish. In the special case of a cylinder or nanotube, two paths returning back to the origin yield a constructive contribution of quantum interferences, reducing the conductance (weak-localization correction). Switching on a magnetic field removes time-reversal symmetry of these paths, resulting in an increase of the conductance or decrease of resistance (negative magnetoresistance). The second effect of the magnetic field is to modulate the field-dependent resistance that becomes $\phi_0/2$-periodic. Indeed, since the phase factors can then be written as ($\boldsymbol{A}$ the vector potential)

$$\alpha_\pm = \pm\frac{e}{\hbar c}\oint \boldsymbol{A}.\mathrm{d}\boldsymbol{r} = \pm\frac{2\pi}{\phi_0}\oint \boldsymbol{A}.\mathrm{d}\boldsymbol{r}$$

the amplitude is then written $|\mathcal{A}|^2\,|1+e^{i(\alpha_+-\alpha_-)}|^2$ resulting in a $\cos(2\pi\phi/\phi_0)$ modulation factor. Below, the behaviors of field-dependent diffusion coefficients are shown for a (9,0) metallic nanotube, as a function of the mean free path evaluated following the analytical formula [104]. By using the Anderson-type disorder, the value of the mean free path can be tuned by the disorder strength W, so that several situations of interest can be explored. First the weak-localization regime [27] is analyzed under the condition $\ell_e < |\boldsymbol{C}_h| < L(\tau_\phi)$.

Figure 6.28 shows that the diffusivity increases at a low fields (negative magnetoresistance) and that the periodic Aharonov-Bohm oscillations are dominated by a $\phi_0/2$ period, that is

$$\mathcal{D}(\tau_\phi, \phi+\phi_0/2) = \mathcal{D}(\tau_\phi, \phi)$$

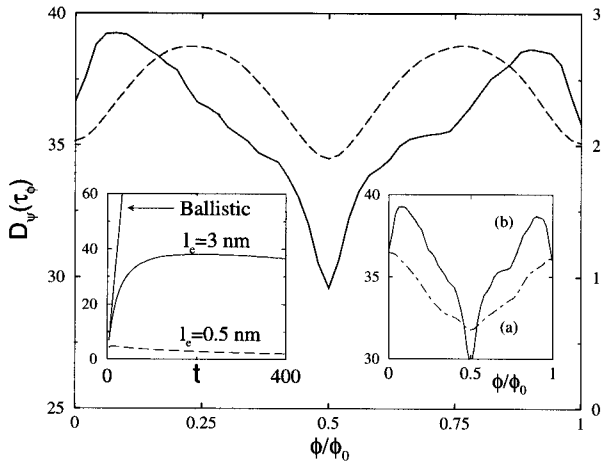

Fig. 6.28. *Main frame*: $\mathcal{D}(\tau_\phi, \phi/\phi_0)$ (in units $\text{Å}^2\gamma_0/\hbar$) for a metallic SWNT (9,0) evaluated at time $\tau_\phi \gg \tau_e$, for two disorder strengths, $W/\gamma_0 = 3$ and 1, such that the mean free path ($\ell e \sim 0.5$ and 3 nm, respectively) is either shorter (*dashed line*) or larger (*solid line*) than the nanotube circumference ($|\boldsymbol{C}_h| \sim 2.3$ nm). The right-hand y-axis is associated with the dashed line and the left-hand y-axis with the solid line. *Left inset*: Time dependent diffusion coefficients for the corresponding disorder values (ballistic motion is also shown for comparison with diffusive regimes). *Right inset*: $\mathcal{D}(\tau_\phi, \phi/\phi_0)$ for $\ell_e = 3$ nm and $L(\tau_\phi) < 2\ell_e$ (*dot-dashed*) or $L(\tau_\phi) > 2\ell_e$ (*solid line*). Adapted from [55]

in agreement with weak-localization predictions. In contrast, when $\ell_e > |\boldsymbol{C}_h|, L(\tau_\phi) < 2\ell_e$, the system is found to exhibit a *positive magnetoresistance* associated with

$$\mathcal{D}(\tau_\phi, \phi + \phi_0) = \mathcal{D}(\tau_\phi, \phi)$$

(ϕ_0 Aharonov-Bohm period). For the case $\ell_e > |\boldsymbol{C}_h|, L(\tau_\phi) > 2\ell_e$, a negative magnetoresistance and an Aharonov-Bohm period Φ_0 are obtained. To compare with the experiment of Bachtold et al. [28], we use the analytical formula for the mean free path (6.104) and with a reasonable value of the disorder parameter, we get $\ell_e \simeq 10^4 \times |\boldsymbol{C}_h|$ ($|\boldsymbol{C}_h|$ the circumference of the outer nanotube in the experiment). The apparent inconsistency between the value of the mean free path and the observation of $\phi_0/2$ Aharonov-Bohm oscillations point out that the interpretation of the experiments has to be elaborated with care, also because the precise position of the Fermi level and contribution of inner shells remain elusive.

6.4.7 Contribution of Intershell Coupling

Multiwalled nanotubes or bundles of single-walled nanotubes present additional geometrical complexity. Indeed, they are made from a few to tens of

shells with random helicities weakly coupled mainly through Van der Waals intershell interaction. The intershell coupling has also been expressed within a tight-binding scheme, which is believed to provide a good description of the electronic structure of multiwalled nanotubes. In the standard model, still one $p_\perp$-orbital per carbon atom is kept, with zero onsite energies, whereas constant nearest-neighbor hopping on each layer n, and hopping between neighboring layers are defined as [58–60]:

$$\mathcal{H} = \gamma_0 \left[\sum_{i,j} |p_\perp^j\rangle\langle p_\perp^i| \right] - \beta \left[\sum_{i,j} \cos(\theta_{ij}) \mathrm{e}^{-\frac{d_{ij}-a}{\delta}} |p_\perp^j\rangle\langle p_\perp^i| \right]$$

where θ_{ij} is the angle between the $p_\perp^i$ and $p_\perp^j$ orbitals, and d_{ij} denotes their relative distance. The parameters used here are: $\gamma_0 = 2.9\,\mathrm{eV}$, $a = 3.34$ Å, $\delta = 0.45$ Å [59]. The difference between SWNTs and MWNTs stems from the parameter β, and the limit $\beta = 0$ corresponds to uncoupled shells. An ab-initio estimate gives $\beta \simeq \gamma_0/8$ [60]. Besides, two kinds of multiwalled nanotubes can be distinguished. The first class corresponds to periodic objects as exemplified by the $(6,4)@(12,8)@(18,12)$ case (Fig. 6.29-Left). Consisting of two semiconducting shells enclosed by a metallic one, there exists a common unit cell for all shells, which is defined by a unique translational vector $|\boldsymbol{T}| \simeq 18.79$Å. In contrast, for the $(6,4)@(10,10)@(17,13)$ tube (Fig. 6.29-Right), the translational vectors along each shell are respectively $|\boldsymbol{T}_{(6,4)}| = 3\sqrt{19}a_{\mathrm{cc}}$, $|\boldsymbol{T}_{(10,10)}| = \sqrt{3}a_{\mathrm{cc}}$, $|\boldsymbol{T}_{(17,13)}| = 3\sqrt{1679}a_{\mathrm{cc}}$, which indicates that there is no unit cell, because of incommensurability (ratio of lengths of individual shell translational vectors are irrational numbers). These two cases illustrate the possibility of obtaining either translationally invariant intertube coupling or aperiodic coupling along the MWNT axis. The natural concern is to search for the related fundamental electronic (transport)-properties intrinsic to MWNTs.

Fig. 6.29. *Left*: Commensurate $(6,4)@(12,8)@(18,12)$ MWNT. *Right*: Incommensurate $(6,4)@(10,10)@(17,13)$ triple-wall nanotube

Commensurate Multiwalled Nanotubes

Commensurate MWNTs are periodic objects with a well-defined unit cell. Bloch theorem applies and the bandstructure can be easily computed. Given that shells only weakly interact, the conductance spectrum of the MWNT in the ballistic conduction regime should be given as the sum of all conducting channels at a given energy (as exemplified on Fig. 6.30). Consequently, one excepts a very small intrinsic resistance at E_F for a metallic MWNT. As discussed below, at certain energies, the intershell interaction might be at the origin of a stepwise reduction of conduction channels.

Let us consider the generic MWNT made of coaxial metallic shells with perfect commensurability, namely the armchair double-walled $(5,5)@(10,10)$ and triple-walled $(5,5)@(10,10)@(15,15)$ nanotubes. Such MWNTs have a fivefold common symmetry. Their respective orientation might also possess additional symmetry planes perpendicular to the tube axis. In that case, interwall interaction does not modify the overall spectrum, which is a superposition of independent spectra. For instance, at the charge neutrality point the conductance for the triple-walled will be $\mathcal{G} = 6\mathcal{G}_0$ (see Fig. 6.30). If, however, the symmetry is lowered by misorienting (rotationally and translationally) one nanotube with respect to another, then splitting of the degeneracy occurs, and pseudogaps are formed [60, 61]. The presence of pseudogaps in the density of states has direct consequences on the total number of conduction channels available at a given energy. As shown by Tomanék and coworkers [62], the conductance in the ballistic regime might then be reduced in the vicinity of Fermi level. Such modifications of the conductance in the ballistic regime

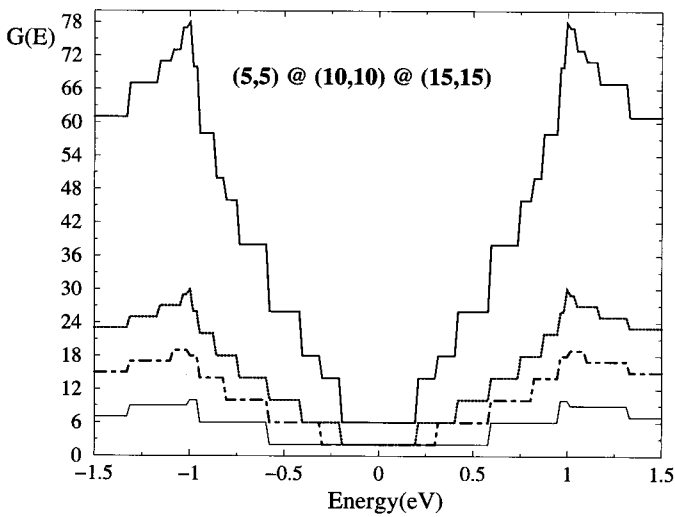

Fig. 6.30. Conductance patterns of the $(5,5)@(10,10)@(15,15)$ MWNT and its constitutive shells

are singular to shell-conformation of multiwalled tubes. Associated with the pseudogaps, charge redistribution can also be investigated [61]. One notes, however, that such a strong effect of intershell interaction is specific to unsymmetrical orientations of neighboring shells, but that is absent for other commensurate walls such as $(6,6)@(11,11)$ with no C_{5h} symmetry.

Incommensurate Multiwalled Nanotubes

The case of incommensurate shells is even more complicated to consider, since no Bloch theorem applies in the strict sense. It is thus more difficult to anticipate the consequences of intershell coupling, e.g. in terms of pseudogaps, on the conductance of such aperiodic MWNT objects. It turns out that the conduction mechanism in MWNTs is quite sensitive to the value of β and to the position of the Fermi energy. To illustrate specific patterns of electronic motion in incommensurate tubes, it is instructive to follow the time dependent evolution of an electronic wavepacket initially localized in the outer shell.

In a commensurate system, assuming a wavepacket initially localized on the outer shell of the MWNT, a rapid redistribution of the weight of the wavefunction on each shell is found to be given by a time scale $\tau_{ll} \sim \hbar\gamma_0/\beta^2$, following the corresponding Fermi golden rule. By increasing the amplitude of β in the range $[\gamma_0/8, \gamma_0]$, the expected scaling form of τ_{ll} is checked numerically [55]. For two electrodes separated by 1μm and assuming ballistic transport with a Fermi velocity of 10^6 ms^{-1}, the corresponding time flight between electrodes is $\sim$4500 $\hbar/\gamma_0$. This is two orders of magnitude larger than τ_{ll} (for $\beta = \gamma_0/8$), and points towards an important contribution of interwall coupling in experiments [63]. In contrast to commensurate MWNTs, the redistribution phenomenon in incommensurate tubes is found much slower with a higher redistributed weight from the outer to inner shells [55]. Such efficient wave redistribution to inner shells seems consistent with the fact that incommensurate systems are intermediate between periodic and disordered systems. The behavior of the diffusion coefficient further allows to unveil that the carrier motion might strongly depart from ballistic motion because of multiple-scattering effects that develop along the conduction pathway. The conduction is found to be *non-ballistic*, with $\sqrt{\mathcal{D}(t) \times t} \sim \mathcal{A}t^{\eta}$ [45,55].

The coefficient η is found to decrease from 1 to $\sim 1/2$ by increasing either β or the number of coupled incommensurate shells [55]. On Fig. 6.31, the conduction mechanism is followed at specific Fermi energies, through the time dependence of the diffusion coefficients, for the incommensurate $(6,4)@(17,0)@(15,15)$ and commensurate $(5,5)@(10,10)@(15,15)$ MWNTs [45]. Whatever the Fermi energy of wavepackets, the conduction mode remains ballistic in the defect-free commensurate MWNT. In contrast for incommensurate systems, depending on the considered energy of charge carriers, the resulting strength of hybridization between states lying on separate layers may strongly fluctuate, with the occurrence of power-law behavior of $\mathcal{D}(t)$.

This anomalous diffusion has subsequent effects on the length scaling of conductance as shown on Fig. 6.31 (right frame). At the charge neutrality point, wavepackets essentially remain confined onto the outer shell as they spread in time, carrier motion is ballistic and a quantized conductance $\mathcal{G} = 4e^2/h$ follows. In contrast, at the energy $E = 1.5\,\mathrm{eV}$, $\mathcal{G}(L) \sim (2e^2/h)(L/L_0)^{\frac{\eta-1}{\eta}}$, with L_0 (or η) an energy dependent length (or exponent). Recent experiments on boron-doped MWNTs have reported on anomalous scaling of the conductance [64]. They found $\eta \sim 1/2$, which points towards a diffusive regime. Similarly, an intershell resistance of $\sim$10 k$\Omega\mu$m has been experimentally estimated in [65].

6.4.8 Role of Electrode-Nanotube Contacts

Two different kinds of metal/nanotube junctions can be defined, namely a *metal-metallic nanotube-metal* or a *metal-semiconducting nanotube-metal* junctions. The latter ones are often subjected to Schottky barriers that forbid electronic transmission at zero or low bias voltage, whereas the former present several atomic-scale properties. Indeed, let us take $|k_m\rangle = \sum_p \mathrm{e}^{\mathrm{i}k_m p}|\varphi_m\rangle$ (or $|k_\mathrm{F}\rangle = \sum_p \mathrm{e}^{\mathrm{i}k_\mathrm{F} p}|\varphi_\mathrm{NT}\rangle$) as the propagating states with k_m (k_F) the wavector in the metal (or nanotube). We take $|\varphi_\mathrm{NT}\rangle$ the localized basis vectors, that will have nonzero overlap with $|\varphi_m\rangle$ only for a few unit cells (p) defining the contact area. The scattering rate between the metal and the nanotube can be

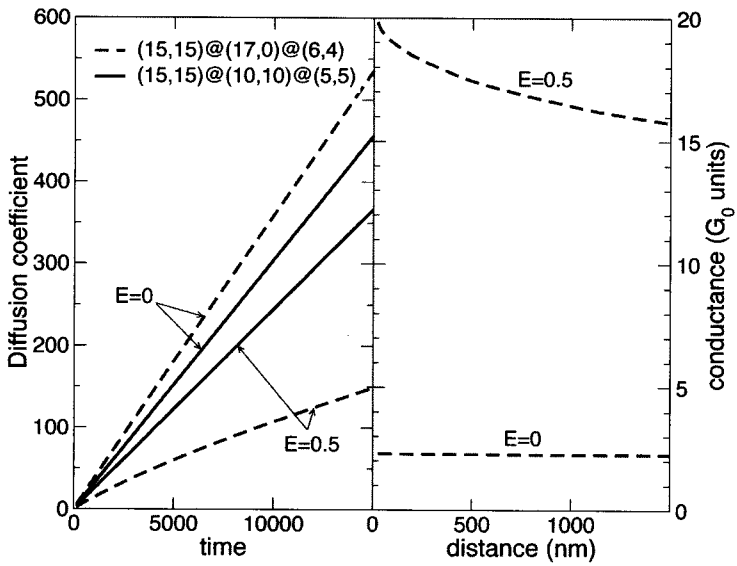

Fig. 6.31. *Left*: time dependent diffusion coefficient for incommensurate/commensurate disorder-free MWNTs (with $\beta = \gamma_0/8$). *Right*: length dependence of conductance for two Fermi energies for $(6,4)@(17,0)@(15,15)$. Adapted from [45]

written following the Fermi golden rule and will be related to

$$\langle k_m|\mathcal{H}_{\text{contact}}|k_{\text{F}}\rangle \sim \gamma'\langle\varphi_{\text{NT}} \mid \varphi_m\rangle \sum_p \mathrm{e}^{\mathrm{i}(k_m-k_{\text{F}})p}$$

with $\mathcal{H}_{\text{contact}}$ the coupling operator between the tube and electrodes. From such an estimate various physical aspects can be outlined: first the factor γ' is related to the chemical nature of interface bonding (covalent, ionic,...). In the most favorable case of a covalent coupling, one expects an ohmic contact resistance given by $R_c = h/2e^2$, whereas ionic bonding would mostly favor a tunneling contact with resistance $R_c \sim h/(e^2|\gamma'|^2)$. The factor $\langle\varphi_{\text{NT}}|\varphi_m\rangle$ is related with the geometry and contact configuration between the nanotube and electrodes: end or side contacts, length of the contact area (see Fig. 6.32). The last term is obviously maximized whenever wavevector conservation is best satisfied, i.e. $\sim \delta(k_m - k_{\text{F}})$. For instance, in the case of metallic armchair tubes, larger coupling will be achieved for $k_m \simeq 2\pi/3\sqrt{3}a_{cc}$. Much smaller metallic wavector will yield small coupling rate. The tunneling rate from the metal to the nanotube is given by

$$\frac{1}{\tau} \sim \frac{2\pi}{\hbar}|\langle k_m|\mathcal{H}_{\text{contact}}|k_{\text{F}}\rangle|^2\rho_{\text{NT}}(E_{\text{F}})\rho_m(E_{\text{F}})$$

with $\rho_{\text{NT}}(E_{\text{F}})$ ($\rho_m(E_{\text{F}})$) the density of states of the nanotube (metal) at Fermi level. Note that these considerations are derived for a low-bias regime. For higher bias voltage between voltage probes, the modifications of bands along the tube axis might produce additional backscattering due to the perturbed profile of available states [66]. Detailed ab-initio studies have recently revealed that titanium contacts would achieve better transmission to metallic tubes than silver or gold contacts [67].

6.4.9 Inelastic Mean Free Path

Electronic transport is also sensitive to inelastic effects either stemming from electron-phonon scattering or weak electron-electron collisions. Again, the special electronic structure of carbon nanotubes leads to unconventional behavior

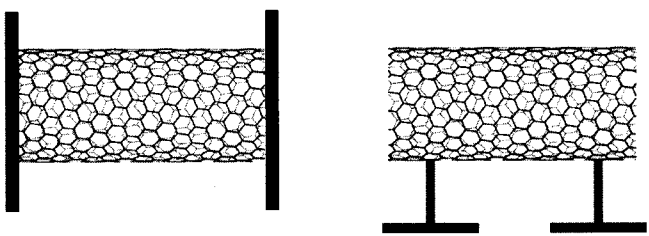

Fig. 6.32. Different contact configuration – end contacts (*left*), side contacts (*right*) – between nanotube and electrodes

as for instance observed in the temperature dependence of resistivity. Balents and Fisher [47] demonstrate for instance that Umklapp scattering due to electron-electron interactions yield a resistivity linear in temperature. Concerning electron-phonon scattering, three important phonon modes yield contributions to inelastic backscattering. As depicted in Fig. 6.33, a first process is driven by acoustic phonons with low energy and small momentum. Within the FGR, the scattering rate (with phonon emission) $\tau_{el-ph}^{-1}(\boldsymbol{q})$ writes

$$\frac{2\pi}{\Omega\hbar}\sum_{k}|\langle \boldsymbol{k}+\boldsymbol{q}, n_q+1|\hat{\mathcal{U}}_{el-ph}|\boldsymbol{k}, n_q\rangle|^2\delta(\varepsilon_{k-q}-\varepsilon_k-\hbar\omega_q)(1+n_q)(1-f(\varepsilon_{k-q}))f(\varepsilon_k)$$

with Ω the surface of the tube, $\hat{\mathcal{U}}_{el-ph}$ the electron-phonon scattering operator, while n_q and $f(\varepsilon_k)$ give the phonon and electron distributions respectively. In metallic tubes, the acoustic torsional mode (twisting mode or twiston) is made of pure circumference-directional deformation, while its velocity is equal to that of the TA mode of the graphene sheet ($\omega(\boldsymbol{q}) = v_{twist}|\boldsymbol{q}|$). A crude estimation due to such inelastic scattering gives $\tau_{el-ph}^{-1} \sim 4\pi/\hbar \times \Xi^2(k_B T/2\rho_M v_{twist}^2)/hv_F$ with ρ_M the mass density, and Ξ the deformation potential. It has to be noted that different from ordinary metals, the linear temperature dependence of the electronic resistivity persists to well below the Debye temperature, essentially because these phonon modes are heavily thermally populated [48]. Now, with reasonable parameters, an inelastic acoustic scattering time is found to be $\simeq 3.10^{-12}$s, with a subsequent inelastic mean free path $\ell_{el-ph} = v_F\tau_{el-ph} \simeq 2.4\mu$m for a 1.8 nm nanotube [49, 50]. A theoretical derivation has also predicted some helical-dependent contribution of

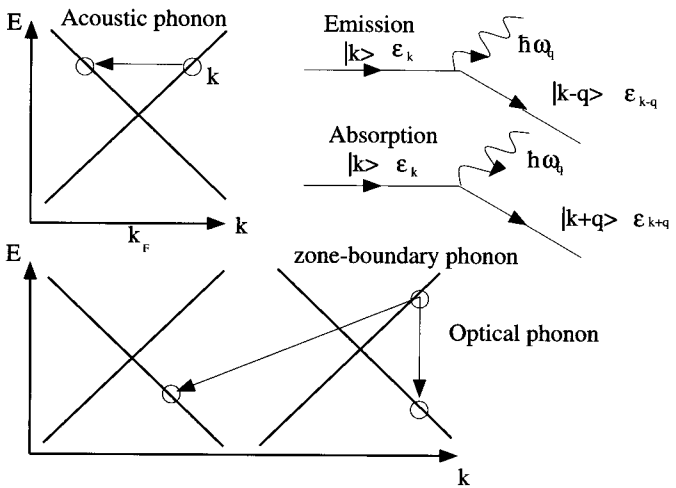

Fig. 6.33. Schematic representation of main phonon contributions to backscattering (acoustic, optical and zone-boundary modes)

electron-phonon backscattering and resistance value in the high-temperature regime [51].

Optical as well as zone-boundary phonon modes also bring some important contributions to backscattering, especially for nanotubes studied in the high-bias regime. For single-walled tubes, recent experiments [50] have inferred typical values of the electron-phonon mean free path in the order of 180 nm for optical phonons, whereas zone-boundary modes yield $\ell_{el-ph} \sim 30$–40 nm. Note that all these inelastic scattering length scales are expected to increase with the nanotube diameter [44].

Perebeinos, Tersoff and Avouris [52] recently proposed to investigate the effect of inelastic scattering on conductance by following the semiclassical Bloch-Boltzmann treatment of transport theory. The authors derive a phenomenological law for the zero-field charge-carrier mobility $\mu(T, d_{\text{tube}}) = \tilde{\mu}(300\text{K}/T).(d_{\text{tube}}/1\text{nm})^{\alpha}$, exhibiting some specific temperature and diameter dependences (here $\tilde{\mu} = 12000\,\text{cm}^2/\text{Vs}$, and $\alpha \sim 2.25$).

In contrast, other theoretical works have investigated the influence of structural lattice fluctuations on the elastic electron transport [53,54]. The superimposed contribution of phonon vibrations has been shown to yield quantum dephasing [53]. For the case of optical phonon modes, the resulting conductance scaling spectrum shows pronounced modifications, making the use of the semi-classical Fermi Golden Rule inapplicable for a rigorous description of charge transport. Clearly, additional work is required to understand how electron-phonon coupling and electrostatic effects jointly contribute to modulate the properties of nanotubes-based field effect transistors.

6.4.10 Electron-Electron Interactions

Carbon nanotubes have provided new possibilities to search for deviations from the Fermi-liquid theory in low-dimensional systems. As discussed in Sect. 6.1.2, strongly repulsive Coulomb interactions likely restrict the range of applicability of the Fermi liquid approximation in describing transport properties. The theoretical possibility for Luttinger-liquid in metallic SWNTs has been proposed when electronic transport through the nanotube-based device is dominated by tunneling through a contact of low transparency. Additionally, the energy of charge carriers should be close to the charge neutrality point, where electronic bands are linearly dispersed. In this case, the interaction parameter g uniquely determines the power-law temperature-dependent (for $eV \ll k_{\text{B}}T$) and voltage-dependent (for $eV \gg k_{\text{B}}T$) tunneling conductances. The generic form $(1 + \frac{2U_0}{\Delta})^{-1/2}$ (U_0 the charging energy, Δ the single particle level spacing) of g is, in this framework, directly related to the power-law exponents (α_m or α_e depending on measurement configuration), see Sect. 6.1.2. Notwithstanding, while the single-particle level spacing is unequivocally given by $\hbar v_{\text{F}}/2L_{\text{tube}}$, the charging energy follows from the capacitive properties of metal-nanotube junction as well as from the electronic structure. In some

approximation [68], it can be derived from simple electrostatics, and the interaction parameter will follow

$$g = \left(1 + \frac{8e^2}{\pi\kappa\hbar v_{\mathrm{F}}} \ln \frac{L_{\mathrm{tube}}}{R_{\mathrm{tube}}}\right)^{-\frac{1}{2}} \tag{6.105}$$

with κ the dielectric constant, and R_{tube} the tube radius. Taking $L_{\mathrm{tube}}/R_{\mathrm{tube}}$ $\sim 10^3$, one finds that the theoretical interaction parameter for a metallic armchair nanotube is $g \simeq 0.28$. Subsequently the bulk-tunneling and end-tunneling exponents are respectively given by $\alpha_m \simeq 0.24$ and $\alpha_{\mathrm{e}} \simeq 0.65$ [68]. Some experiments have reported on similar behaviors and exponent values [69]. Interestingly, one notes that in the case of MWNTs composed of N metallic armchair shells, a certain screening of interactions occur since the exponents are renormalized by a factor $1/N$ (α_m/N and α_{e}/N) which is equivalent to an increase of g that tends to 1 in the limit $N \to \infty$ (Fermi-liquid regime) [70]. This also underscores the consequences on the transport properties with the change of dimensionality from the SWNT to the MWNT case.

Following theoretical predictions by Eggert [71], recent STM experiments have provided strong evidence for non-Fermi-liquid properties of metallic nanotubes [72]. In this work, the tunneling properties of electrons from a metallic tip to a metallic tube deposited on a gold substrate have evidenced that the Coulomb interactions are strong enough to induce charge-spin separation, although screening by the metallic substrate also results in some reduction of the predicted interaction strength.

This is illustrated in Fig. 6.34, where a tight-binding calculation shows the two standing waves with different wavelengths caused by separate spin and charge bosonic excitations. The slopes calculated near the **K**-points ± 8.8 cm^{-1} and ± 11.9 cm^{-1} correspond to larger charge mode group velocity of $\sim v_{\mathrm{F}}/0.55$, whereas the spin-mode velocity remains similar to the Fermi velocity v_{F} obtained for non-interacting electrons.

The deduced values for the g-parameter is thus ~ 0.55, much smaller than the predicted value given by the unscreened coulomb potential ($g \sim 3$). This clearly evidences the screening phenomenon caused by the underlying metallic substrate, and that can be substantiated by replacing in (6.105) L_{tube} by a screened length (found to be $\sim 1.4 R_{\mathrm{tube}}$ in experiments [72]).

6.5 Measurement Techniques

A measurement of the electrical properties of an object, as diverse as it seems (with temperature, magnetic field, gate voltage, etc), always reduces to our ability to measure simultaneously the injected electron flow (current) and the resulting potential drop (voltage) in the sample. The simplest measurement that can be done is that of the classical electric resistivity of a material. This

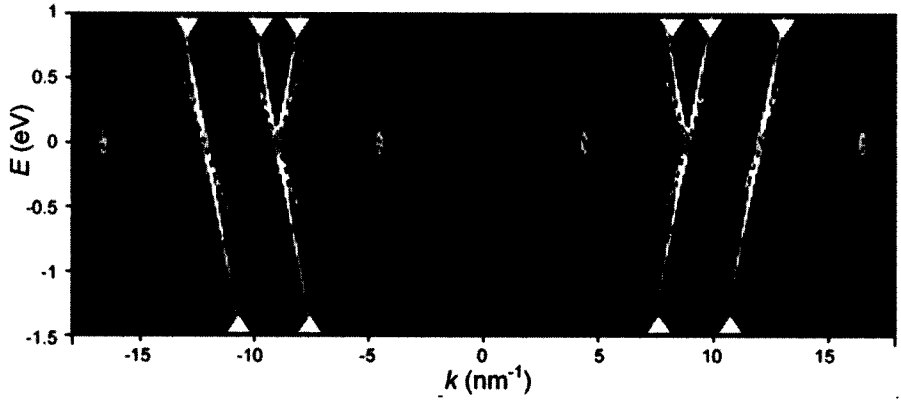

Fig. 6.34. Fourier transformed mas of $\mathrm{d}I/\mathrm{d}V$ (density of states) as a function of electron momentum k, and sample bias V. Ovals near the Fermi levels indicate the corners of the brillouin zone nearest (*green*) or second nearest (*orange*) to the Γ-point. Red curves give the energy dispersions of the (19,7) tube by tight-binding, whereas superimposed color lines indicate the Luttinger-liquid result. Adapted from [72] by courtesy of S. Eggert

requires to measure the resistance $R = U/I$ and to know the exact geometry of the sample used. As we will see later, the second point is not as trivial as it seems.

6.5.1 Classical (Macroscopic) Approach

Two-Probe Measurement

On a macroscopic sample, the so-called 2-probe resistance measurement is still often performed. The injected current and the voltage drop are measured using the same lead on a versatile apparatus (ohm-meter) (Fig. 6.35a). Knowledge of the sample size allows straightforward calculation of the resistivity with the hypothesis of a uniform voltage drop across the sample. However, the main draw-back of this set-up is that the voltage drop in the lead is included in the total voltage drop, so the sample resistance is over-estimated. Of course, low-resistance leads can bring these effects to extremely small values. However, another effect can appear: a poor contact between the lead and the sample. Poor (or bad) contact can simply result from surface oxidation. In the two-probe configuration the voltage drop at the contact is also included in the whole measurement.

Four-Probe Measurement

To avoid this problem, physicists use the 4-probe measurement technique. Two independent circuits are considered: one to inject the current, the second

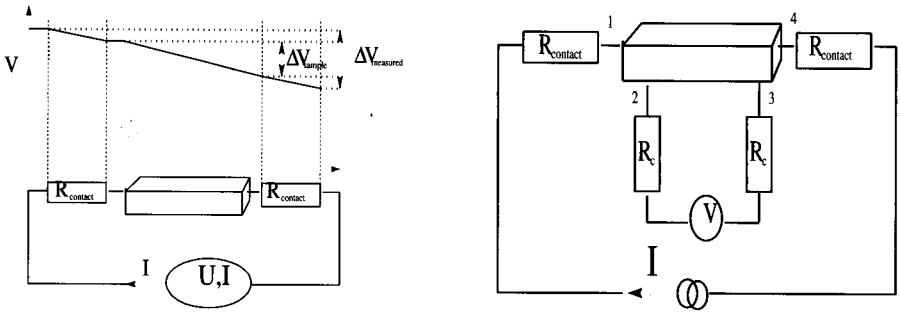

Fig. 6.35. *Left*: Two-probe measurement overestimating of the resistance drop in the sample. *Right*: Four-probe measurement configuration (current through voltmeter is negligible)

to measure the voltage drop (usually between the current-injection leads) Fig. 6.35-Right. The only practical condition is to have a high impedance voltmeter (high compared to the sample resistance). In this set-up, as no (or very little) current is passing through the voltmeter circuit, the injected current is, to a great accuracy, the current that flows through the sample, regardless of the lead and contact resistance. The measured voltage drop is the genuine voltage drop across the points 2 and 3 of the sample (contact and lead resistance effects are negligible because the current through the voltmeter is minute). Calculation of the sample resistivity is now also simple, provided that the distance between lead 2 and 3 is accurately known.

Importance of the Contact Size

The contact size of the lead that is injecting the current is irrelevant provided the contacts have a sufficient distance from one another, i.e. the electron flow is uniform in all the sample by the time it reaches the inner contacts (Fig. 6.36-Left). However, in the case of a strongly anisotropic material (as graphite or MWNT), this condition might not be automatically reached (Fig. 6.36-Right).

In contrast, the size of the voltage probe contact must be as small as possible: large contact area can induce errors in the resistivity calculation if the metal used for the contact pad has a lower conductivity than the sample. Figure 6.37 depicts, in an exaggerated fashion, such an effect. Getting a contact area negligible compared to the distance between probes is easy to achieve on a macroscopic sample (20 μm gold wire for the probe, 5 to 10 mm, between the two probes), however, as we will see, mesoscopic samples are much prone to such problems.

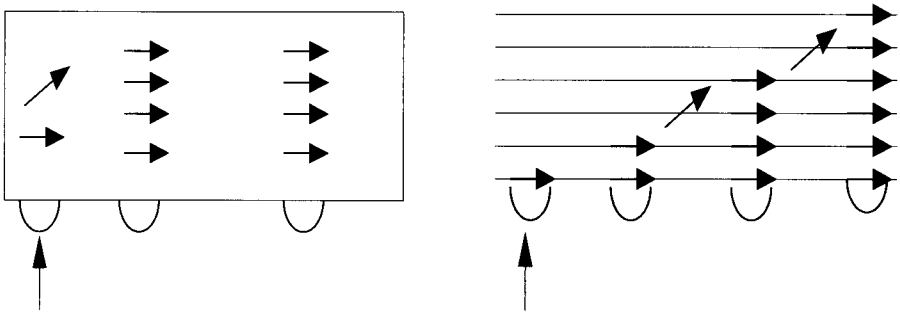

Fig. 6.36. *Left*: Isotropic material, current flow is homogenous on the sample even if injected from a single entry. *Right*: For anisotropic material, non-homogeneity in current flow can extented far from the injection point

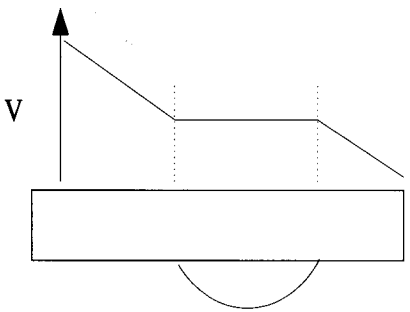

Fig. 6.37. Voltage probe with low resistivity on highly resistive sample. The potential drop is no longer uniform along the sample

6.5.2 Experimental Problems on Mesoscopic Samples

Choice of the Contact Type and Realization

The sample we are now looking at is of micrometer dimensions. First, we have to compare the size of the available electrode to the sample size: if our sample is smaller than the electrode width technically available in the laboratory, there are only two-probe measurements to consider. We will first have a short tour of the actual techniques, from the most crude (and cheap) to the most refined (and expensive). The objective is not to explain technical details but to give an overview of what can be made, how difficult it is and what the advantages are.

Direct Evaporation

The simplest way to realize a metallic contact is to evaporate a metal film (usually gold, but other choices are possible [67]) over the sample after part of it has been shielded from the evaporator. This technique has been successfully

used by de Pablo et al. [73] on MWNT. They used 4 μm tungsten wires for a mask. As a result, both end of the MWNT were buried in metal and a two-probe transport measurement was achieved (Fig. 6.38).

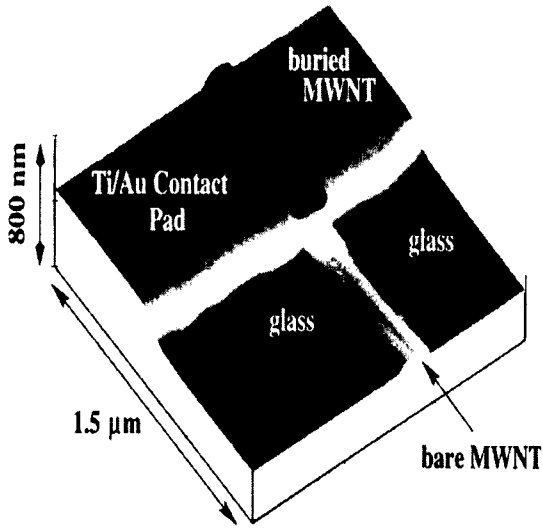

Fig. 6.38. Result of a direct evaporation on a MWNT deposited on a glass substrate. The central part of the MWNT has been protected by a 4 μm tungsten wire

This technique is inexpensive (tungsten wire of 4 μm diameter costs about 2 Euros/10 cm, while an evaporator can be home made). The problem is that only large samples can be processed in that way as 4 μm is the limit of what can be manipulated with tweezers on a table top.

Lithographic Processes

In a lab equipped with lithographic facilities, sub-micron electrodes can be processed. The width is limited by optical diffraction. Depending on the facilities, a width of 300 nm can be obtained with the desired pattern. If a specific mask has to be made, the cost can increase substantially. Electron beam lithography allows even lower widths to be processed [74], see Fig. 6.39. The cost for the mask can easily reach a thousand Euros depending on complexity. In the case of the electrode on top approach (see next section), the experimenter must make sure that the lithographic process (resin, exposure, dissolution, etc) does not alter the sample.

Focus Ion Beam (FIB)

In this set-up, a metallic ion beam is extracted from a metallic source, focused and deposited in a controlled way on the substrate. Widths are in the 10 nm

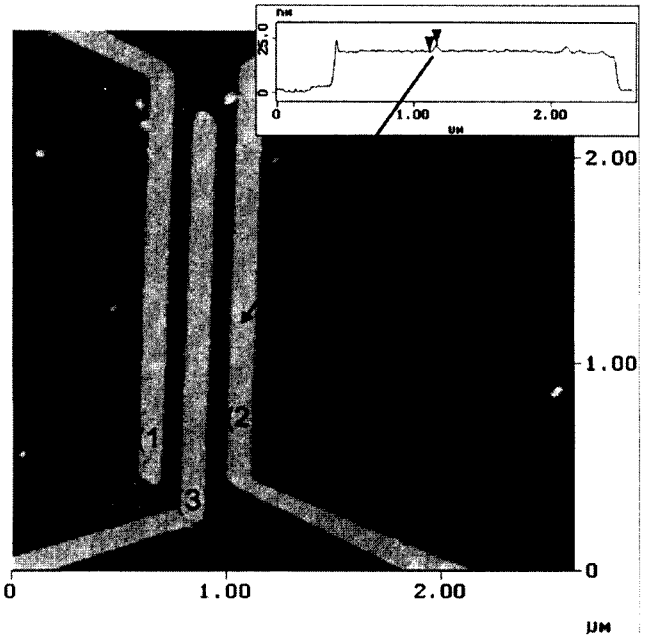

Fig. 6.39. Three 100 nm wide electrodes on top of a SWNT bundle (electron beam lithography). Note the relative width between the probes and the sample

range (16 nm with gallium in the FEI Dual Beam System 620). This setup can be implemented on an existing scanning electron microscope. The cost is heavy: about 400 000 Euros for a complete FIB installation (example on Fig. 6.40).

Sample on Top Versus Electrode on Top

As sub-micrometer patterns are always made on top of an insulating flat surface, two routes are possible: the sample can be deposited first, located and the electrode further deposited on top, or the electrode pattern can be made (or bought) before and the sample deposited afterwards. In the case of a rigid sample, the two methods should be essentially equivalent. However, in the case of soft and deformable samples, the electrode pattern can induce distortions that alter the sample transport properties (see Bezryadin [76]).

The sample-on-top configuration has the strong advantage that one can buy ready-to-use patterned substrate with the required electrode spacing. The problem is usually to obtain intimate contact between the sample and the electrodes as only Van der Waals forces are playing a role. Spot-welding techniques have been used to increase the contact quality in some cases [77]. The electrode-on-top configuration seems better in several aspects. First, there is no or little distortions of the sample when the contacts are deposited. Second,

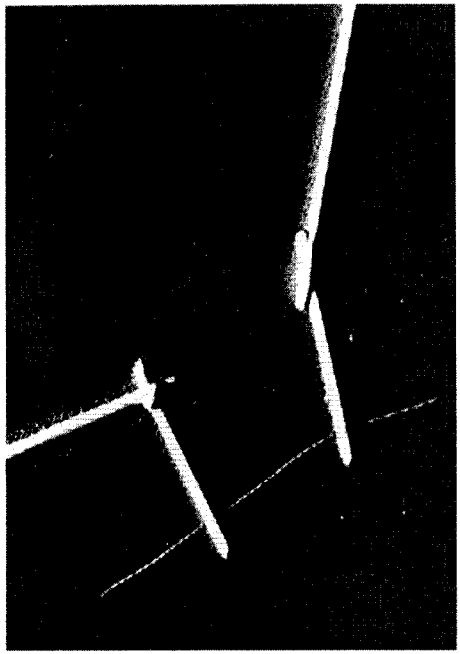

Fig. 6.40. Nanotube contacted with tungsten lead made by FIB lithography [75]

the contact is essentially of better quality (that of course depends on the sample preparation). In both techniques, the ability to position and/or locate the sample with required accuracy is a compulsory step. This stage is crucial in several aspects: one of them is the inherent risk of sample damaging during the process. First, risk occurs when the samples are produced in large quantity and must be dispersed over the surface. Dispersions are often achieved through combined chemical (surfactant) and mechanical (sonication) action. For carbon nanotubes, which are chemically and mechanically extremely stable samples, it has been demonstrated that surfactants can substantially affect the transport properties [63] and that sonication is a convenient tool to cut them into pieces [78]. In that respect, however strong the sample seems, tests must be carried out to check that theses processes are reversible (surfactant can be washed away) and non-destructive for the sample. Second, risk appears when the sample is manipulated to be positioned onto a specific place after deposition [79]. Once again, potential damaging of the sample must be considered.

Measurement of the Voltage and Current

Now that our sample is contacted, some amount of current can be injected and a measurement of the voltage drop can be achieved. We will discuss the

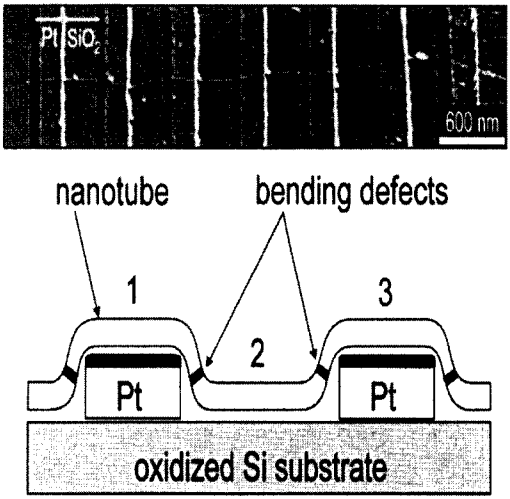

Fig. 6.41. Long SWNT deposited on top of Pt electrodes (*top*). Occurrence of bending defect near the electrodes (*bottom*). Adapted from [82]

(almost ideal) case where the sample is long enough to be used in a four-probe configuration, with the electrodes on top of the sample and assuming that the contacts are fairly good. It seems now that the resistance of our object is simply the ratio of the measured voltage drop to the measured current. Unfortunately, several problems can occur. First, as was said at the beginning, the width of the electrodes that pick-up the voltages must be small compared to their distance. This might be difficult, if not impossible (see Fig. 6.40). Solutions to this problem consist of assuming that the measured voltage drop occurs between the end of the first electrode and the beginning of the second. Secondly, it has been known since 1898 [80] that when two metals of different work functions are put into contact, a contact potential appears between them. This effect is well known in semi conductors (p-n junction). The same effect holds for metal/semi conductor junction (better known as Mott or Schottky Barrier). Between metals, the depletion width is negligible, so this barrier is usually considered to be completely transparent to the electrons. i.e. a metal electrode will eventually inject electrons in a metallic sample, even if their work functions did not match. But what happens to the conduction electron of the mesoscopic sample if a large metal electrode disturbs its band structure as in Fig. 6.39.

Krstic et al. [74] have observed the effect of an electrode laid on top of a nanotube bundle on its transport properties and concluded that the mere presence of this electrode disturbs the transport. A proposed solution is to use for the electrode a metal with a work function that matches the studied sample [81]. Despite its advantages, it seems that the four-probe method is not well suited for mesoscopic samples. The coupling between the sample and the

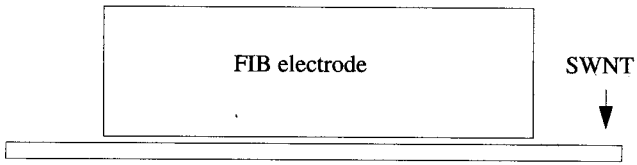

Fig. 6.42. Drawn at the same scale, the narrowest metal electrode that can actually be made with FIB (about 10 nm width) on top of a SWNT (1.4 nm diameter). Work function difference can disturb the band structure over non-negligible distance and alter transport properties

electrode is not as simple as it seems, since differences in work function will locally alter the band structure with important consequences for extremely sensitive systems (such as one dimensional transport). For a more detailed discussion, see Datta [4]. Then how to process it? Two alternative approaches have been envisioned, both based on the two-probe configuration.

The first alternative is to use local probe-techniques such as electrostatic force microscope (EFM). While current is driven through the sample, a tip probes the potential drop along the sample [82]. Influence on the transport properties seems minute and can be controlled by approaching the probe while monitoring the effects on the two point transport. The measured potential drop can be linked to the resistance. The second approach consists of using several samples of identical cross-sections and different lengths with the same contact method or to vary the distance between electrodes on the same sample (one side is usually fixed) [63, 83, 84]. If the contact contribution is the same, the only change can be attributed to the intrinsic sample resistance. The major challenge resides in the difficulty to realize reproducible (and comparable) contacts.

Reproducibility of the Measurements

The point of this section is not to look for a resistance variation on a single sample (which we expect to be stable, except for variation of temperature, humidity, magnetic field, etc), but from the sample to sample reproducibility.

As discussed previously, measuring several samples of different length in a two-probe configuration might be an alternative to the four-probe method. From a theoretical point of view, identical nanoscopic objects, contacted in an identical manner, should have identical behavior. Identical is not experimental, objects are produced with defects and some dispersion in size. To illustrate this point, we will study the very simple case of the gold break-junction experiment: Two clean pieces of gold in contact are pulled apart. A thin short-lived gold wire is created. The width is so small that transport quantification is obtained. This experiment is well documented [85] and transport quantization is known to occur in this mesocopic system. However, if we observe a single event (Fig. 6.43 right), nothing special is usually observed. In

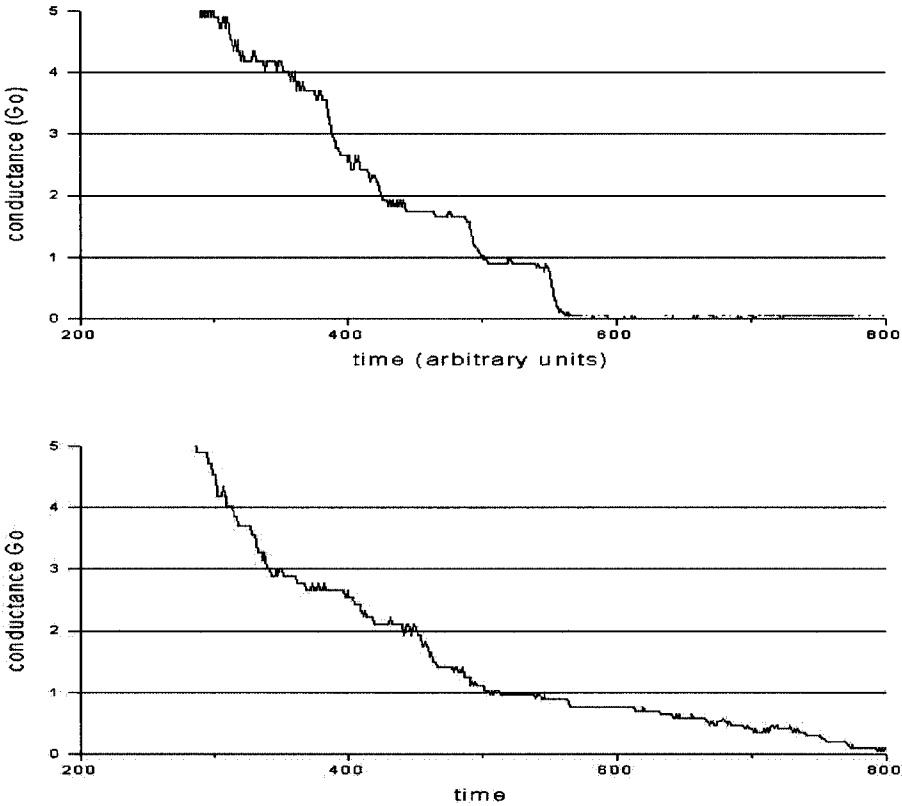

Fig. 6.43. Two traces of gold break junction, plotted on the same time scale. The first one (*upper part*) exhibits two clear plateaus while no clear quantification is visible in the second one

other cases, clear plateaus, that coincide with quantized transport, are roughly observed (Fig. 6.43 left). So in one experiment quantization is observed, but not in the other. What to conclude? Simply that observations based on a single event might not be representative. Only statistical approaches (repeated experiments on several samples) have a physical meaning.

In the above case, the object was clearly defined: a pure, well contacted, gold wire. Fluctuations were mainly due to the geometry of the sample and some random scattering (contact, crystallographic defects in the wire, etc). Now imagine what could happen if the object itself is not well defined (defect densities, shapes, size), prepared through different processing (surfactant, sonication, AFM-manipulation, spot welding on contact, etc) and measured with various methods. Of course one can expect the results to be different (see [86] as an example of how the result vary).

Calculation of the Resistivity

If eventually we succeed in pulling some numbers out of these tricky experiments, can we compute the resistivity? What was simple for a macroscopic object is no longer easy. First let us take a large semiconducting mesoscopic sample: a regular line 80 nm wide, and 5 nm thick, distance between electrode 2 μm. Assuming that we have extracted the value of 10 kΩ for its 'resistance', what about its resistivity? If the above numbers are correct, then ρ is 2 μΩm. Unfortunately the above mentioned numbers are only known to a limited accuracy. Even in the best case: height measured with AFM ($\Delta h = 0.1$ Å), width and length by high resolution Scanning Electron Microscope ($\Delta x = 1$ nm), lead to a 3% error (2.03 μmΩ.m to 1.97 μmΩ.m). Things get worse for smaller objects like nanotubes given that their cross-section is not well defined. The diameter of a SWNT is typically 1.4 nm, but its wall thickness can be estimated from 3.4 Å (from interlayer distance in HOPG) down to 0.66 Å (carbon atomic radius). Here differences can reach a factor 5 (for resistivity, but also for current density).

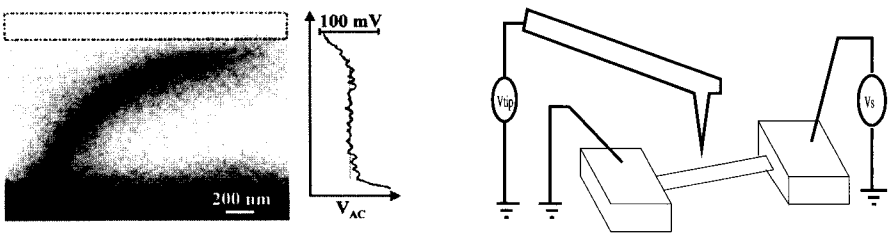

Fig. 6.44. *Left*: EFM record of the potential drop along a SWNt bundle. *Right*: Experimental setup. Adapted from [87]

6.6 The Case of Carbon Nanotube

6.6.1 Study of Some Experimental Measurements

As we have seen, four-probe experiments are maybe not always the best suited approach for mesoscopic objects. In the case of carbon nanotubes, it is noteworthy to remark that four-probe experiments have usually failed to point out the extremely long electronic mean free path that occurs in these systems.

Measuring the Voltage Drop Using EFM Techniques

In the experiment by Bachtold et al. [87], the electrostatic potential is measured along a SWNT bundle connected on its two extremities while a voltage

drop is applied. The recorded voltage drop leads to a bundle resistance per unit length ρ_l below 1.5 kΩ/μm. This gives a mean free path longer than 1 μm at room temperature providing there is only two conducting nanotubes (in this 2.5 nm high, 2 μm long bundle). Note also that, using the same experimental setup, the authors found individual MWNT to be a dissipative conductor (voltage drop is linear along the nanotube).

Extracting the Intrinsic Resistivity by Reducing the Inter-Electrode Gap

Individual MWNT were used in these setups [63]. One side of the nanotube is connected to a conductive fiber, while the other side is dipped into liquid metal. The resistance is monitored while the distance between contact is continuously reduced.

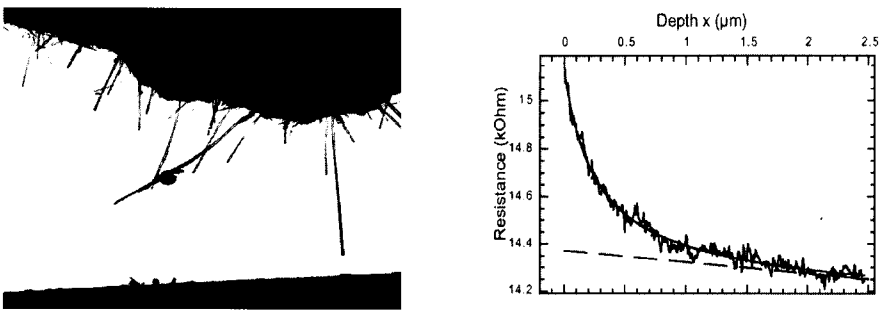

Fig. 6.45. *Left*: TEM picture of a measured individual MWNT. *Right*: Measured two-probe resistance versus depth. From a simple model, one can the extract contact resistance (14 kΩ) and the intrinsic nanotube resistance ($\rho_l = 14$,Ω/μm)

An analysis of one simple trace led to the conclusion of a mean free path longer than the system ($\rho_l \gg 14\,\Omega/\mu m$, see [63] for detailed calculation). However, on a single measurement, one cannot distinguish between an highly conductive nanotube and a classical contact resistance (about 14 kΩ at the fiber side) or a small contact resistance and a reduced transmission in the nanotube due to conductance quantification (transport quantification within the nanotube). To discriminate, the experiment has been repeated over 40 to 50 different nanotubes (i.e. different diameter and fiber-connected length). The contact resistance always turns out to be in a 13–15 kΩ range, unexpectedly stable in regard to the studied variety of MWNT (only from diameter, the contact resistance should have changed from a factor 2 to 3). This statistical result let the author consider that this 'contact resistance' is intrinsic to the nanotube and is actually a signature of the transport quantification within the nanotube.

6.7 Experimental Studies of Transport in Nanotubes and Electronic Devices

6.7.1 Introduction

Nanotubes and other nanostructures form new classes of materials with remarkable and unique properties for electronics and optoelectronics applications. Their electrical properties are often distinct from those of their bulk counterparts, due to the confinement of the electronic states and the surface contributions. The nanostructures are often made by self-assembly, which is compatible with large-scale production, and they present dimensions covering a length scale that is not easily achievable by the conventional top-down approaches. The first comprehensive electrical studies on carbon nanotubes were performed in 1997 [88,89].

This section presents a selection of experimental studies and aims to review some of the important electrical properties of metallic and semiconducting carbon nanotubes. First, we will discuss the scattering mechanisms in metallic carbon nanotubes. Second, we present the recent results on the field-effect transistor based on individual SWNT. Last, we review the general properties of the 1D Schottky barrier at the metal-nanotube junctions and describe the operation of a nanotube Schottky-barrier transistor (SB-CNFET).

6.7.2 Electrical Transport in Metallic Carbon Nanotubes

The unperturbed transport in metallic carbon nanotubes takes place through a limited number of sub-bands close to the charge neutrality point. In this region, the 1D dispersion relation for the nanotube can be approximated by $E(k) = E_F \pm \hbar \cdot \nu_F (k - k_F)$, where $k_F = \pm(2/3) \cdot \pi/a$ is the Fermi wavevector for armchair nanotubes and the lattice constant $a = 2.46$Å. The situation around E_F is schematically illustrated in Fig. 6.46.

In total, four sub-bands contribute to the conductance of the nanotube with both positive and negative slopes at $-k_F$ and $+k_F$. This 1D nanotube band structure limits the various scattering events at finite temperature. That is, the 1D confinement allows electron motion in only two specific directions along the length of the nanotube. This constraint along with the requirements for energy and momentum conservation severely reduces the phase space for scattering.

As illustrated in Fig. 6.46, only few processes are possible. These are essentially mediated by impurity, electron-phonon scattering or electron-electron (e-e) collisions. The impurity scattering is an elastic event while electron-phonon and electron-electron scattering are inelastic by their nature. Moreover, inter-band scattering involving higher-energy sub-bands can also take place, but the probability of this process is very weak since the energy separation with the other sub-bands is large (of the order of the electron volt).

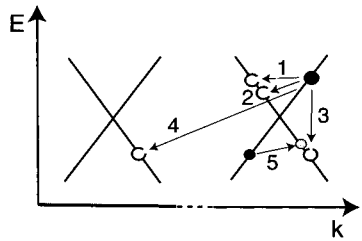

Fig. 6.46. Band-structure diagram showing elastic (**1**) and inelastic (**2**–**4**) backscattering in a carbon nanotube satisfying energy and momentum conservation. Process (**1**) is for impurity scattering and (**2**) involves the emission of an acoustic phonon with small energy and momentum transfer. Processes (**3**) and (**4**) show the emission of an optical phonon for low and high momentum transfer, respectively. Process (**5**) is an e-e scattering process as described in the text

The number of scattering events in a carbon nanotube segment of length L is therefore limited. They can be probed by two-terminal resistance measurements as a function of temperature according to:

$$R_{2t} = R_0 + \frac{dR}{dT} \cdot T = \frac{h}{4e^2} L \left(\frac{1}{L_0} + \frac{1}{L_{e-ph}} + \frac{1}{L_{e-e}} \right) \tag{6.106}$$

L_0, L_{e-ph} and L_{e-e} are the mean free paths for impurity, electron-phonon and electron-electron scattering respectively. In absence of collisions, i.e. in the ballistic regime, we expect conductance quantization and no temperature dependance. In that case, (6.106) is reduced to : $R_{2t} = h/4e^2$.

The intrinsic properties of a single carbon nanotube are difficult to measure because of the 1D nature of the nanotube and the strong perturbation introduced by the contact leads. This point is discussed below. In principle, it is possible to discriminate between the different scattering mechanisms using a careful analysis of R vs. T curves.

Impurity Scattering

The scattering of an electron by an impurity involves another state that is at the same energy but of opposite momentum direction (see process **1** in Fig. 6.46). This is backscattering and it leads to a residual resistance that is higher than the resistance of a pristine nanotube.

Phonon Scattering

Scattering with phonons, such as in processes **2**–**4** in Fig. 6.46, is an inelastic event where backscattering occurs with the emission (or the excitation) of a phonon of energy $E_{ph} = \hbar c_{ph} k_{ph}$, where c_{ph} is the phonon velocity. Here, E_{ph} depends on the available phonon modes in the nanotube. For example, acoustic phonons have a broad energy spectrum for scattering at low energy

while optical phonon scattering can be neglected for energy transfer of less than 100 meV [90, 91].

Electron-Electron Scattering

This scattering has typically little impact on the resistance of a conductor, but it is expected to be more pronounced for 1D conductors. The case of carbon nanotubes is special because of the linear dispersion around E_F. The modes are crossing at E_F and backscattering as in process **2** in Fig. 6.46 can also be promoted by e-e scattering, although its probability remains weak. Electron-electron collision can also take place with its counterpart being scattered in the reverse position as in the process **5** (Fig. 6.46). In this case, the total momentum and energy is conserved.

Temperature Effects

While impurity scattering has no (or very little) temperature dependence, the total initial and final states for e-e collisions increase with temperature (or with electric excess energy, i.e. bias). As a result, the electron-electron scattering time increases linearly with temperature (i.e. $\tau_{ee} \propto T^{-1}$) [92]. The temperature dependence of the electron-phonon scattering rate follows the same trend, i.e. $\tau_{e-ph} \propto T^{-1}$ [93]. As a result, the R vs. T curves for a SWNT is expected to be linear for both electron-electron and electron-phonon backscattering according to $L_{e-x} = v_F \tau_{e-x}$ and (6.106). Therefore, the basic scattering mechanisms can hardly be discriminated on the basis of the trend seen in the R vs. T plots. However, it is reasonable to assume that electron-phonon scattering dominates at room temperature. The arguments are discussed in [48, 92–96]. Complementary investigations of the resistivity using bias voltage dependence provide further details on the relative contributions. As it is today, there are still unanswered questions about the backscattering mechanisms observed in carbon nanotubes. To illustrate the current status in this area, three important examples are given below.

Experimental Evidences of Electron-phonon Scattering

There is strong evidence that the elastic mean free path in SWNT reaches several microns in length at room temperature [98–101]. This conclusion comes from cumulated evidence acquired on rope and on individual SWNTs from both laser-ablation and CVD growth techniques. In fact, the measurement of the scattering length is difficult because the contact electrodes introduce significant barriers along the current path (invasive probes). In general, R vs. T curves show a resistance that increases with decreasing temperature, a behavior that is not expected for scattering with either impurity, electron or phonon. It is therefore important that we understand the impact of the contacts and find ways to optimize the contact configuration. An example

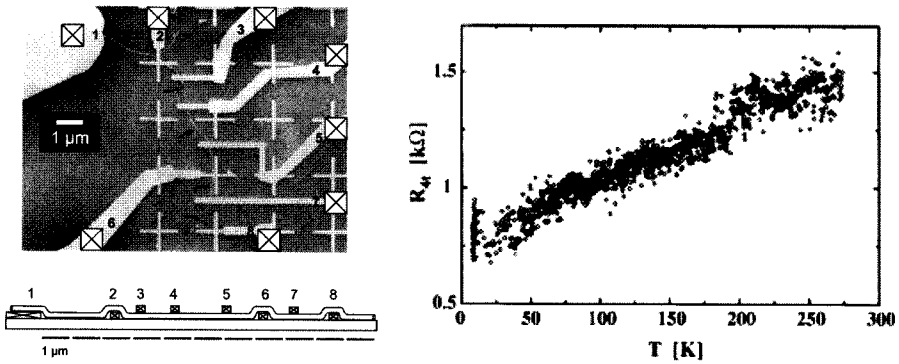

Fig. 6.47. *Left*: SEM image of a single-wall carbon nanotube rope attached with a combination of top and bottom gold contacts. *Right*: Four-terminal resistance with temperature obtained with bottom contacts for current drive and top contacts for voltage probe. Adapted from [101]

of unperturbed R vs. T curve with the expected linear response is shown in Fig. 6.47.

It was obtained using a special four-terminal measurement [101]. Here, the contact electrodes are connected to a nanotube rope. The current probes are directly in contact with the bottom of the rope while the voltage probes make contact to the top-most nanotubes of the rope. Thus, the current bias is applied to the bottom nanotubes and the weak tube-tube interaction forces the current to pass only at the bottom of the rope [101]. In this configuration, the voltage probes do not perturb the bottom nanotubes and allow to measure the voltage drop across the current carrying nanotubes without introducing backscattering. The measurement gives a weak linear dependence of the resistance with temperature and a positive slope $d\rho/dT$ of 2.4 $\times$ 10^6 Ωm/K. This result presents a clear signature of weak electron-phonon scattering in the nanotubes [101]. The characteristic length for electron-phonon scattering from this experiment is $L_{\mathrm{e-ph}} \times N = 11\,\mu\mathrm{m}$, where N is the number of metallic nanotubes directly contacted by the bottom electrodes. N is estimated to be between 1 and 3 nanotubes, which gives an elastic mean free path between 3 and 11 µm at room temperature.

Yao et al. have shown that the scattering length in SWNTs depends on the electron excess energy, eV, which is given by the applied voltage across the carbon nanotube [96]. At high bias (up to 5 V), they observed that the current saturates at about 20 mA (Fig. 6.48) and the whole IV curve can be fit by a simple function: $R = R_0 + V/I_0$, where R_0 is the low-bias resistance of the device and I_0 is the extrapolated saturation current.

Two possible candidates can be invoked to explain this behavior: electron-electron and electron-phonon collisions. However, scattering with optical or zone-boundary phonons is theoretically more likely to lead to the current saturation at I_0 [96]. The key point here is that the electron is first accelerated

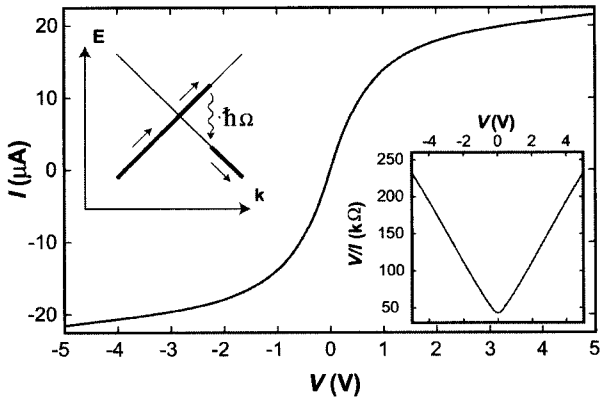

Fig. 6.48. High-bias $I - V$ characteristics of a metallic single-walled carbon nanotube. The right inset re-plots the data as V/I versus V, while the left inset shows the schematic of the phonon emission model. Adapted from [96]

under the applied field inside the nanotube because of the weak scattering with acoustic phonons. Then, it backscatters as soon as it reaches enough energy to emit an optical or zone-boundary phonon. This situation is illustrated in the inset of Fig. 6.48. In the steady state, the forward moving electrons travels across the nanotube with an excess energy E_{opt} above that of backward moving ones. With this, the saturation current I_0 is given by

$$I_0 = \frac{4e^2}{h}\left(\frac{e}{E_{\text{opt}}}\right) \tag{6.107}$$

Under these conditions, the mean free path L_{e-ph} for backscattered phonons is the distance an electron must travel in the electric field to gain an excess energy that is equal to the phonon energy:

$$L_{\text{opt}} = \frac{e}{E_{\text{opt}}}\frac{L}{V} \tag{6.108}$$

where L/V is the electric field along the SWNT. The dominant scattering mechanism at high bias has therefore a mean free path that scales inversely with applied voltage. A substitution of (6.108) into (6.106) leads to a relation that grasps the physics of scattering at large bias

$$R_{2t} = \frac{h}{4e^2 L_0}L + \frac{h}{4eE_{\text{opt}}}V \tag{6.109}$$

Here the acoustic phonon scattering is neglected for the obvious reasons explained below. In this model, an optical phonon of $E_{\text{opt}} = 0.16\,\text{eV}$ leads to the saturation of current at 25 mA. This value is consistent with the onset estimated for the optical phonons in SWNTs [96]. Other experiments [97] performed on nanotubes-based field effect transistors, and showing ballistic

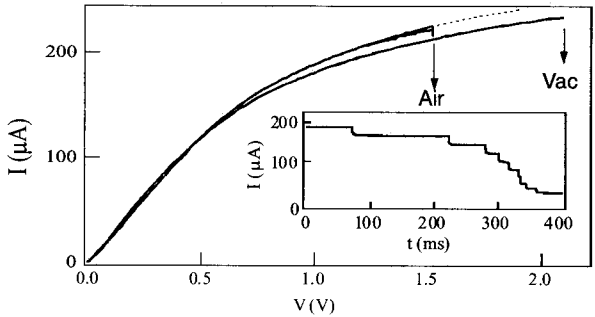

Fig. 6.49. Four-probe $I - V$ and time resolved I curves for two segments of a MWNT. Segment A is electrically broken in high vacuum, while segment B is broken in air. Before failure, both segments have nearly identical $I - V$ characteristics in vacuum (segment B in vacuum shown as dashed line). Vacuum breakdown occurs in segment A at 2.2 V and 235 mA. At this high power, the breakdown proceeds to completion in less than 1 ms. In air, segment B exhibits a much slower breakdown initiated at a lower power. Adapted from [102]

conductance at low bias, have reported values of the inelastic mean free path in the range of 10 nm for high voltage situations.

Current Saturation and Breakdown

Carbon nanotubes can withstand remarkable current densities, exceeding 10^9 A/cm^2, in part due to their strong carbon-carbon bonding and the relatively weak electron-phonon scattering. However, at high enough currents nanotubes ultimately fail. The breakdown of the nanotube can occur because significant dissipation takes place at high field through the optical phonon and inter-band scattering. Figure 6.49 presents such a dramatic event observed with two segments of the same MWNT (14 nm diameter) in air and in vacuum [102]. In both cases, the IV curves saturate at a current I_0 that is much larger that the saturation values for SWNTs. In fact, I_0 for MWNTs is sample dependent and the breakdown is never below the point of inflection in the IVs. This observation suggests that the onset of saturation and the eventual breakdown process are linked to a common dissipative process, most likely involving the excitation of high energy optical or zone boundary phonons [102]. Moreover, the threshold power for breakdown in air is lower, probably due to the rapid oxidation of the outermost carbon shell. AFM images indicate that MWNT breakdown usually occurs midway between two electrodes, which is precisely where dissipative self-heating will produce a peak temperature.

More detail of the failure process is shown in the inset of Fig. 6.49. The current vs. time plot shows abrupt drops of current indicating that the MWNT thinning occurs with the loss of individual carbon shells. This also suggests that the steps in $I(t)$ are due to shell-by-shell failure of the MWNT. Similar

thinning has been seen by in-situ transmission electron microscopy [103]. The value of each step is somehow close to the current saturation (25 mA) observed in individual SWNTs and does not change much as the process goes on. The origin of the steps is therefore linked to the saturation current observed with individual SWNTs. Therefore, the current saturation seen before breakdown in MWNTs involves several shells carrying a maximum of current I_0. In addition, as discussed by Yao and coworkers [96], the scattering with the optical phonons seems to be the origin of the overall behavior presented in Fig. 6.49.

6.7.3 Nanotube-Based Transistors

Prototype field-effect transistor devices with carbon nanotubes (CNTFET) have recently shown performance exceeding that of the best silicon-based metal-oxide-semiconductor FET (MOSFET) [104, 105]. This surprising result has also been confirmed by other groups [106, 107]. Then, why a CNFET is able to outperform the best silicon MOSFET? Early experiments [108] on SWNT FETs demonstrated that they behave much like conventional MOSFETs. However, there are some important differences: (i) the carbon nanotube is 1D and the scattering probability is weak. As a result, CNFETs of less than a micron in length are likely to operate in the ballistic regime, which is not the case for silicon MOSFETs even for 10 nm devices. (ii) The nanotubes are made of chemically satisfied carbon atoms and no dangling bond is present at the surface. Therefore, there is no need for careful passivation of the interface between the nanotube channel and the gate dielectric, i.e. there is no equivalent of the silicon/silicon dioxide interface. These properties make the one-dimensional transistor action in nanotubes unique and interesting. Last, doping, as used in microelectronics, is not yet an option for the optimization of CNFETs. As a result, a Schottky barrier is often present at the nanotube-metal contacts. Therefore, most of the CNFETs are Schottky barrier transistors [109].

Top-Gate Nanotube-Based Transistors

Early nanotube FETs used a non-local back-gate with the nanotube being contacted by noble metal electrodes. This arrangement gave large contact resistances and poor characteristics [108, 110, 111] . Since then, significant improvements in the performance of CNFETs have been achieved [105, 106]. New structures are now built with top-gate geometry and they resemble, in many respects, to conventional silicon MOSFETs. An example of the characteristics of a top-gated CNFET is shown in Fig. 6.50. This CNFET is contacted with titanium electrodes and the gate is made of Al separated by 15 nm of gate oxide (SiO_2) [105]. First, a very large improvement was observed compared to the early nanotube devices. This is mainly due to the scaling of the dimensions (mostly the gate oxide thickness) and the adoption of a better device geometry. A comparison of key parameters has been made and suggests that the performance of CNFETs exceed the best conventional Si MOSFET [104–106].

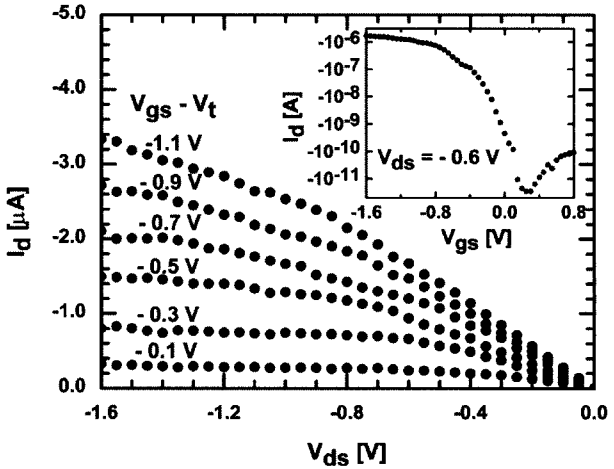

Fig. 6.50. Output characteristics of a high performance carbon nanotube field-effect transistor. The gate is placed on top of the nanotube and separated by 15 nm oxide thickness. The inset shows the sub-threshold characteristics of the transistor highlighting the 6 orders of magnitude ON-OFF ratio. Adapted from [105]

Nanotube-Metal Schottky Barrier

The CNFETs measured in air, as in Fig. 6.50, are usually p-type, i.e. the tubes conduct holes upon applying a negative gate voltage and they show no evidence of electron conduction even at very large positive gate voltage. In addition, the ON state of CNFETs in air show ohmic *IV*s at small source-drain voltage. This is a clear indication that the metal-nanotube contact has no (or only little) effect on the injection. This situation changes when the devices are annealed in vacuum. This step removes the adsorbed oxygen and yields to a reversible transformation of the CNFETs from p- to n-type. An example of such a transformation is presented in Fig. 6.51.

Initially, a p-type CNFET (**1**) is annealed in vacuum and transformed into a n-type device (**2**). Then, oxygen is slowly introduced into the chamber and IVs are acquired at intermediate stages of the transformation [112]. The intermediate stages (e.g. curve **3** in Fig. 6.51) are ambipolar, i.e. the tube can conduct both electrons and holes. This transformation can be easily rationalized by considering the presence of barriers at the contacts. Each situation is presented in Fig. 6.51. In air, the Fermi level at the metal-nanotube junction is closer to the valence band of the nanotube. This leads to hole conduction and p-type behavior. The annealing step changes the line-up of the bands at the junction and lowers of the barrier for electron injection. This modification at the contacts also introduces an increase of the barrier height for hole injection, leading to an n-type CNFET. The intermediate stage, however, simply occurs when the contact Fermi level is around mid-gap. This special situation

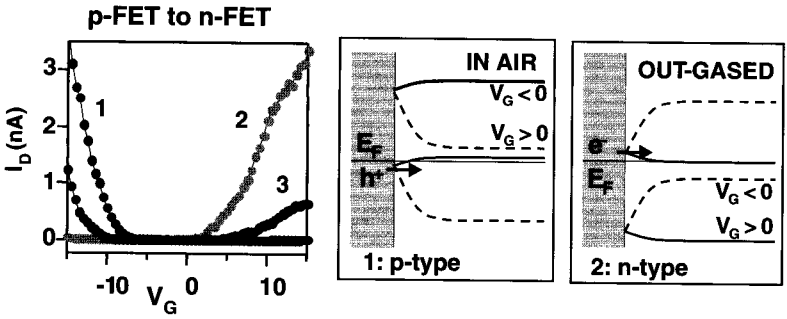

Fig. 6.51. Inter-conversion between p- and n-type CNTFETs using vacuum annealing and oxygen exposure and the related band diagrams. n-type CNTFET are obtained by annealing a p-type CNTFET in vacuum at 700 K for 10 minutes. The gradual convertion of a n-FET (**2**) back into a p-FET (**1**) is done by oxygen exposure. Adapted from [112]

gives similar barrier height (i.e. half of the bandgap, E_g) for electron and hole injection and the device is ambipolar.

6.7.4 Ambipolar Carbon Nanotube Transistors

The ambipolar CNFET is particularly interesting in that it allows us to explore in depth the properties of one-dimensional (1D) metal-nanotube junctions. The contact situation for the ambipolar device is perhaps the worst since it involves a mid-gap alignment of the Fermi level and therefore the barriers for electron and hole injection are the highest ($E_g/2 \sim 300\,\text{meV}$). Surprisingly, the IVs at room temperature are ohmic (see Fig. 6.52) as if there was no (or little) barrier at the metal-nanotube junction [113].

This behavior is unique and not seen in Schottky barriers at 3D metal-semiconductor junctions. The temperature dependence of the IV curves for the ambipolar device in the hole accumulation region are presented on the right panel of Fig. 6.52. The results are essentially the same for the electron accumulation region. The data for both electron and hole injection gives very small barrier heights using a conventional thermal activation plot (Arrhenius plot) [114]. The number is at least 20 times lower than expected ($\sim$15 meV instead of $\sim$300 meV) barrier height, which is obviously wrong. Therefore, the injection process across the Schottky barrier involves another mechanism which is more likely to be due to tunneling across the barrier. In fact, the barrier in 1D is so thin that the junction is quasi-transparent for carrier tunneling, i.e. there is a very efficient injection through the barrier. The shape of the barrier is triangular with some non-uniformity at the bottom. Moreover, it strongly depends on the gate field (see an example of calculation in Fig. 6.53) [115]. As a result, the injection of carriers may become very asymmetrical depending on the conditions at the contact.

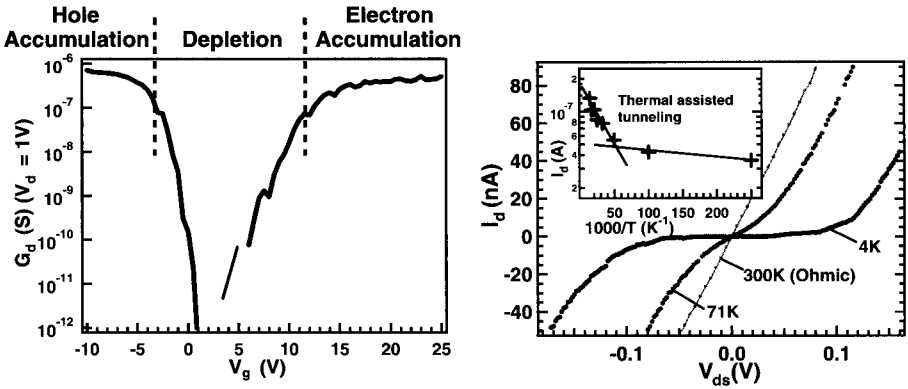

Fig. 6.52. *Left*: Sub-threshold characteristics of an ambipolar nanotube field-effect transistor. *Right*: Characterization of the Schottky barrier for the ambipolar transistor ($L = 800$ nm) as a function of temperature. The IV curves in the hole accumulation are ohmic at room temperature, which is consistent with only small barrier. This is surprising since the barrier is estimated to be around 300 meV, i.e. much higher than k_BT. Adapted from [113]

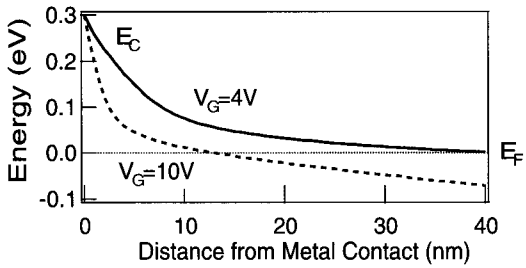

Fig. 6.53. Calculation of the Schottky barrier near the metal-nanotube contacts. Conduction-band energy plot near the contact shows a thin triangular shape barrier for gate voltage of 4 and 10 V. Tunneling current is modulated by the change of the barrier shape under the gate field. Adapted from [115]

The properties of the metal-nanotube Schottky barrier are useful and interesting. In particular, they allow the simultaneous injection of electrons and holes when large drain bias are applied to an ambipolar CNFET (the current is balanced at $2V_d = V_g$). This effect results in polarized infrared emission peaking at the bandgap of the carbon nanotube [116]. The ambipolar CNFETs are currently the smallest electrically driven optical source ever made.

Schottky Nanotube Transistor: Operating Mode

The nanotube transistor characteristics resemble those of the conventional MOSFET, but the underlying physics of operation is very different. The

Schottky barrier at the contact is hard to eliminate and there is no good scheme to dope locally the nanotube in the contact region. Moreover, the presence of a contact barrier is hard to identify from the IV curves. In fact, the transistor action for CNFETs is usually limited by the injection process at nanotube-metal contact. They have been shown to be Schottky barrier transistors (SB-CNFETs) [109].

The main question is why the characteristics of the SB-CNFET resemble those of a regular MOSFET? To answer this, we need to consider in detail the band evolution under the influence of the gate and the drain fields. The output characteristics of a SB-CNFET is schematically illustrated in Fig. 6.54.

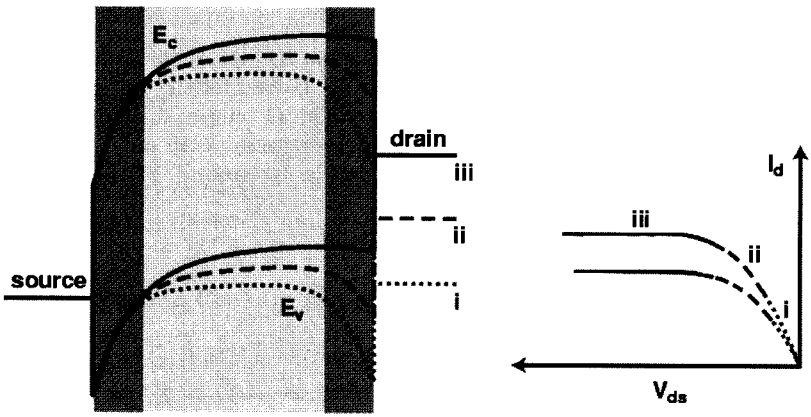

Fig. 6.54. *Left*: qualitative band diagram describing the operation a Schottky barrier nanotube field-effect transistor in the ON state. *Right*: the corresponding output characteristics for two arbitrary gate voltage. Adapted from [117]

The dark gray regions highlight the band close to the metal contact. The Fermi level at the contact is somewhere inside the bandgap of the nanotube. Here we assume that no scattering takes place in the nanotube. The ON state operation of a p-type SB-CNFET goes as following: *region i*: I_d (current at the drain) changes linearly with V_d (drain bias) since the tunneling barrier is thin on the source side. That is, the gate field is strong on the source side (the device is ON) and determines the shape of the barrier. *Region ii*: I_d becomes non-linear because the situation on the drain side approaches the flat band condition. This is because the drain voltage is getting close to the gate voltage and the drain to gate field is gradually vanishing. *Region iii*: I_d saturates when the barrier in the drain region vanishes. This saturation is NOT the pinch off of the channel as usually observed in conventional MOSFET [118]. A change of the gate bias will have the effect of shifting the current up or down because it has a direct effect on the thickness of the source contact barrier. As a result, the current in all three regions is affected by the gate. Last, in this

band scheme, the bulk of the nanotube channel has no effect on the IVs. Thus, the nanotube channel is not limiting the current of the SB-CNFET. This implies that the intrinsic properties of the nanotube are NOT probed by the SB-CNFETs unless the contact barrier is eliminated.

6.8 Transport in Nanotube Based Composites

6.8.1 Introduction

As shown in previous sections, their electronic properties lead at a nanoscopic level to fascinating phenomena such as quantum box effects, Coulomb blockade, ballistic transport, and so on. On the other hand, it is also possible to take advantage of these properties at the macroscopic scale, by embedding the nanotubes into a matrix, i.e. by building a composite. Here we focus on the transport properties of composites where the matrix is a polymer and the nanotubes act as loading particles or fillers. These composites are sometimes referred to as extrinsic conducting polymers. The fillers which are commonly used are carbon blacks, metallic nanoparticles, organic needles. Indeed the mechanical properties of CNT make them even more interesting than the conventional fillers. Potential applications of these heterogeneous materials are transport layers in organic devices such as LED or solar cells, electrostatic shields, electromagnetic shields.

We first introduce some basic concepts relevant for the transport properties of heterogeneous systems, followed by a short survey of the published works regarding CNT based composites. Section 6.8.2 is devoted to the transport mechanisms. The last two sections are concerned with non-linear transport and magnetotransport. Since very few works on CNT based composites is published, their properties applied to CNT mats (buckypaper, pressed pellets, etc.) are briefly discussed.

6.8.2 Transport in a Heterogeneous Medium

Basic Percolation Theory and Effective Medium Approach

We consider the situation in which a volume fraction p of conducting particles with conductivity σ_0 are embedded into an insulating matrix. Indeed, when $p = 0$ the composite is an insulator while it is conducting if $p = 1$ with conductivity σ_0. In between, a finite conductivity ($0 < \sigma(p) < \sigma_0$) is obtained when a continuous conduction path connects both sides of the sample. Assuming that the particle-to-particle contact is electrically transparent and that the fillers are randomly dispersed into the matrix, the transition between the insulating to the conducting state occurs above a threshold fraction p_c. This topologically driven transition is referred to as the percolation transition. Percolation theory has a broad range of applications. A comprehensive introduction is

given in [119,120]. This phase transition is second order and as such, critical behavior is expected close to the percolation threshold p_c. Within this theory, above and close to p_c, the conductivity of the composite obeys the power law:

$$\sigma = \sigma_0[(p - p_c)/(1 - p_c)]^{\beta} \tag{6.110}$$

The conductivity exponent β depends only on the dimensionality of the system ($\beta \sim 2.0$ in 3D) while p_c also depends on the network coordination. In 3D and for randomly dispersed conducting spheres, $p_c \sim 0.16\%$. Smaller thresholds are obtained when the fillers are non-spherical. In this case, it was suggested that the excluded volume has to be considered instead of the actual volume of the fillers [121]. This results in a percolation threshold following $\Phi \times p$ a constante, and $\Phi = L/r$ being the aspect ratio of the filler. Alternative models can be used to describe the electrical properties of composites [120]. Far from p_c and close to 1, it has been shown that the effective medium theory which gives $\sigma \propto p$ nicely describes the evolution of the conductivity [122].

Application to Nanotube-Based Composites

Several groups have reported on CNT-polymer composites (SWNT [123,124] or MWNT [125]). Quite generally, a percolation-like transition is observed with reported thresholds that vary from 0.02% to 10%. This broad range of p_c values originates from the sample preparation but p_c also depends on the experimental setup used for conductivity measurements. Because of the very high aspect ratio of CNT, transverse or sandwich geometry leads to finite size effects that lower p_c.

In PMMA/SWNT composite films, typical values give $p_c \sim 0.3\%$ and $\beta \sim 2.1$, whereas $\sigma_0 \sim 83$ S/cm [124]. Using the excluded volume concept, this small p_c may be explained by an aspect ratio of $\Phi \sim 100$ while the exponent β is in agreement with transport in 3D. When p tends to 10%, effective medium theory applies, and gives a room temperature conductivity of the SWNT mat of the order of σ_0. Measurements on a pressed pellet (i.e. a $p = 1$ composite) gives the same order of magnitude.

6.8.3 Transport Mechanism

Very few reports have been published regarding the transport mechanism in CNT based composites. Here, we summarize what is usually discussed in extrinsic conducting polymers.

6.8.4 Localization and Hopping

In most cases, the charge carriers are localized on the fillers with a localization length ξ. For SWNT fillers, the carriers originate from metallic tubes, and transport occurs via tunneling or hopping (phonon assisted tunneling) from

one filler to another. At the microscopic scale and low temperatures, hopping is described by a transition rate Γ between two sites given by:

$$\Gamma = \nu_0 \exp\left(-\frac{2r}{\xi} - \frac{\Delta}{k_B T}\right) \tag{6.111}$$

r is the distance between the two sites, and Δ is related to their energy difference. Pure tunneling obeys (6.111) without the $\Delta/k_B T$ contribution. The macroscopic conductivity is obtained by optimizing all Γ that defines a temperature dependent conduction path. Without interactions between the carriers and assuming a constant density of states $\rho(E_F)$ at the Fermi level, optimization leads to Mott's variable range hopping (VRH) [126]. The VRH conductivity follows:

$$\sigma \propto \exp\left[-\left(\frac{T_0}{T}\right)^{1/(d+1)}\right] \tag{6.112}$$

where d is the dimensionality and $T_0 \propto 1/\rho(E_F)\xi^d$. This temperature dependence is widely observed in buckypapers or SWNT mats (with $d = 3$) [124,127]. The VRH model gives ξ in the order of a few tens of nanometers, if one considers the metallic SWNT $\rho(E_F)$.

6.8.5 Coulomb Interactions and Coulomb Gap

Charging a metallic particle requires one to overcome the Coulomb charging energy E_c which scales with $1/s$ where s is the typical particle size. The charging effect is important when the fillers are nanoscopic such as in cermets [128]. It is quite similar to the case of VRH in presence of Coulomb interactions where a soft Coulomb gap Δ_{CG} digs at the Fermi level during the transport process [129]($\Delta_{CG} = e^3\sqrt{(\rho(E_F)/(\varepsilon_{PMMA} + 4\pi\rho(E_F)\xi^2)^3}$, ε_{PMMA} the PMMA dielectric constant). This process leads to $\sigma \propto \exp[-(T_0/T)^{1/2}]$ where T_0 is related to Δ_{CG} (respectively to E_c) and to ξ (or s). Such a temperature dependence in PMMA/SWNT composites has been observed below 50 K [124], and was attributed to the digging of a Coulomb gap of magnitude $\Delta_{CG} \sim$ 10 meV. Loading the composite more and more leads to a partial (mutual) screening of the charging energy, and thus to a disappearance of the charging effects in $p = 1$ sample. Mott's VRH is thus recovered at high p fraction.

When E_c is small, as for example in carbon blacks (CB) or carbon fibers loaded composites, Sheng et al. [130] have proposed that transport occurs via direct tunneling between adjacent fillers. However, the tunneling probability is modified by the thermal noise which induces fluctuations of the tunneling barrier. This fluctuation induced tunneling model gives $\sigma \propto e^{-T_0/(T+T_1)}$ which has also been used to describe the conductivity of SWNT mats [131].

6.8.6 Percolation Network

The percolation pathway depends on temperature as does the hopping/tunneling process. A special case has been invoked in CB loaded composites

where it is believed that localization occurs at the scale of the incipient infinite cluster of the percolation theory. This kind of localization is referred as superlocalization and leads to VRH with a non fractional exponent of the conductivity [132].

6.8.7 High-Electric-Field Effects

High electric field E also influences the transition rates which results in non-ohmic behavior. Here we just discuss the mechanisms involving tunneling or hopping which are invoked in CNT based materials.

A high electric field may cause emission across a tunnel barrier. This Fowler-Nordheim emission process is at the origin of the field-emission properties of CNT (see Chap. 4). At high field, it is found that the current density J increases as $J \propto E^2 \mathrm{e}^{-a/E}$. When fluctuation induced tunneling is relevant, $J \propto \mathrm{e}^{-a(E/E_0-1)^2}$ [130]. Such a field dependence was invoked in SWNT buckypaper [131].

Several processes have been proposed when VRH occurs. They depend on the field magnitude and on the details of the material. In a weak field and with a small DOS at the Fermi level, 'heating' of the electron gas due to the potential energy gain may occur (not to be confused with Joule effect). The energy distribution of the carriers is disturbed and an 'electric temperature' T_{el} can be introduced at $T = 0$ K:

$$k_{\mathrm{B}} T_{\mathrm{el}} = \gamma e E \xi \tag{6.113}$$

where γ is a numerical factor close to 1. This model was used by Fuhrer and coworkers in SWNT buckypaper [129]. When the thermal temperature is finite, VRH transport occurs in the same way as it does at zero field but at the price of replacing the real temperature by an effective one $T_{\mathrm{eff}} = T + T_{\mathrm{el}}$ [133].

The field dependence observed in PMMA/SWNT composite seems in agreement with this picture [124]. Using the effective temperature concept allows one to build master curves which unify the ohmic temperature dependence and the electric field dependencies for all investigated p fractions. It suggests that localization is intrinsic in this system.

Increasing the field also changes the transport pathway. In very high fields, VRH is lost and simple tunneling occurs [126].

6.8.8 Magnetoresistance

Two kinds of magnetoresistance effects may be considered. The spin dependent contribution is weak in CNTs as long as magnetic particles are absent. Still, the presence of catalysts may contribute to a negative magnetoresistance (MR) in weak field. In CNT based materials, the main contribution is orbital in nature.

In a weak field, application of a magnetic field H partly destroys the quantum interferences which appear along the transport path [134]. A negative magnetoresistance is found quadratic (or linear) in field. This effect is the strong localization counterpart of the weak localization negative MR discussed in Sect. 6.8.2. Indeed MR saturates as soon as the magnetic flux through the hopping area scales with the flux quantum Φ_0.

$$H(R_{\rm hop}^3.\xi)^{1/2} = \Phi_0 \tag{6.114}$$

where $R_{\rm hop} \propto \xi(T_0/T)^{\alpha}$ is the hopping length. In the left panel of Fig. 6.55, we show such a behavior in $p = 8$ % PMMA/SWNT composite. Below 20 K, the MR is linear and the saturation field corresponds to $\xi \sim 7$ nm. Above 20 K, a quadratic MR is observed without saturation effects in the field range. The same behavior was also observed in SWNT mat [129].

In high fields ($\Phi > \Phi_0$), shrinkage of the wavefunctions occurs which reduces the transfer between adjacent sites. A positive magnetoresistance is found:

$$\ln(R(H)/R(0)) \propto H^2\xi^4(T_0/T)^{3/2} \tag{6.115}$$

here in the presence of Coulomb interactions [129]. This positive MR has been observed at low temperatures ($T < 8$ K) as shown in Fig. 6.55. Once again, a localization length $\xi \sim 7$ nm is deduced.

6.9 Thermal Transport in Carbon Nanotubes

6.9.1 Introduction

Some forms of carbons are the best known heat conductors at room temperature (Table 6.1) and it was easy to figure out soon after the discovery of carbon nanotubes (NT) that they should exhibit a very large thermal conductivity.

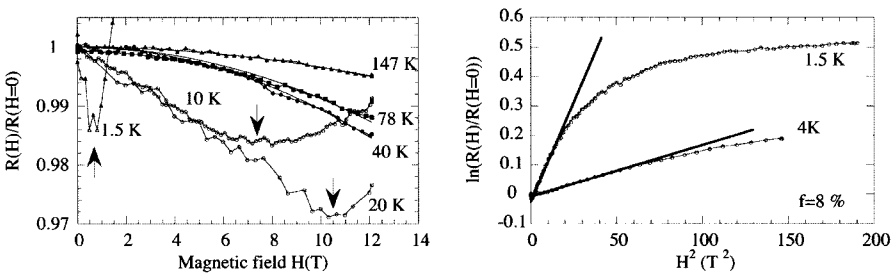

Fig. 6.55. *Left*: Negative MR due to quantum interferences in a SWNT/PMMA composite with $p = 8\%$. The arrows show the saturation field of (6.114). At $T = 1.5$K, the saturation comes from scattering with catalytic particles. *Right*: Positive MR due to orbit shrinkage (see (6.115)) in the same sample at low temperature. In both cases, $\xi \sim 7$ nm is found

This should lead, as for the case of some carbon fibers heat treated at high temperatures, to interesting applications as 'hyperconductors' of heat in the form of composites [135]. However, due to the difficulty of measurements (cf. below 6.9.4), preliminary experimental results were only available recently to confirm this view. Indeed, in order to interpret correctly the experimental results by comparing them to theoretical predictions, measurements need to be performed on individual nanotubes. This is a very delicate experiment to perform which was only realized recently on a MWNT by Kim et al. [136] using sophisticated nanolithographic techniques. The first thermal conductivity measurements on NT, which were performed on bundles [137], did not lead to a straightforward interpretation, since measurements pertained to an average taken over a group of different nanotubes. Moreover, for the case of bundles, to the thermal resistance of the individual nanotubes should be added that of the contacts between them, and contact resistances are always difficult to evaluate. This is not the case for the specific heat where contact resistances do not play a direct role. On Table 6.1, we have listed the orders of magnitude of the thermal conductivity of carbons and graphites at room temperature. We have also shown for comparison the room-temperature value for copper and the range of conductivities for most polymeric materials.

Table 6.1. Thermal conductivity of carbons and graphites at room temperature

Material	Conductivity ($Wm^{-1}K^{-1}$)	Heat Treatment
Nanotubes	$>10^3$	
Diamond	10^3	
HOPG	10^3	>3000°C
Vapor deposited Fibers	10^3	<3000°C
Pitch Fibers	10^2–10^3	2000–3000°C
Pure Copper	5×10^2	
PAN Fibers	10	
Polymeric Materials	10^{-1}	

The phonon spectrum of graphite is highly anisotropic and may be considered as quasi-2D for frequencies above a few THz. This anisotropy is naturally reflected in the lattice thermal conductivity which is the dominant heat transport mechanism, except at very low temperatures. In-plane we find the highest room-temperature thermal conductivities, comparable to that of diamond, which is the best known heat conductor (Table 6.1). Normal to the graphene layers, the thermal conductivity is two orders of magnitude lower at 300 K (Fig. 6.56). This anisotropy is reduced as the temperature is lowered. Owing to their reduced dimensions, the phonon spectrum of NT may be quantized at low temperatures, as is the case for the charge carriers. This quantization should be reflected in the specific heat and thermal conductivity.

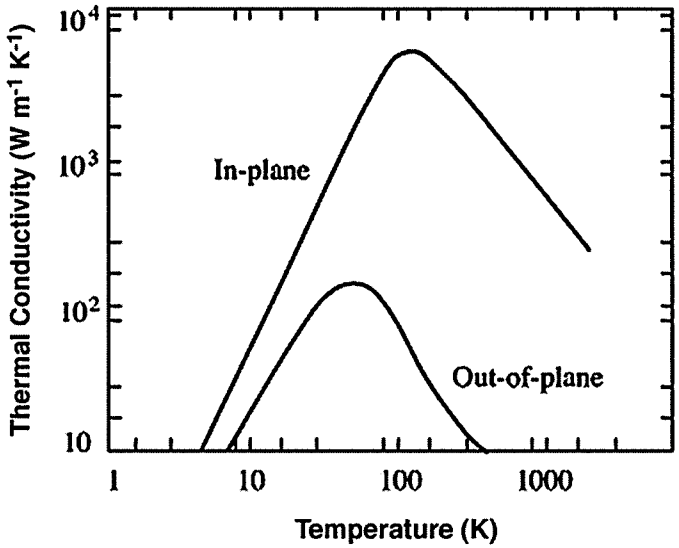

Fig. 6.56. Schematic representation of the temperature variation of the thermal conductivity of HOPG in-plane and out-of-plane showing the strong anistropy in the higher temperature range. This anisotropy is reduced as the temperature is lowered

We will now discuss the thermal conductivity (Sect. 6.9.2) and the thermoelectric power (Sect. 6.9.3) data available on carbon nanotubes (NT) and then briefly comment on the problems encountered when performing their measurement (Sect. 6.9.4). Emphasis will be placed on the recent results obtained on an individual MWNT [136], since they may be compared to theoretical estimations. We will lean heavily on the knowledge accumulated through the study of other forms of carbons [138].

6.9.2 Thermal Conductivity

In Chap. 1 of this volume [138], we introduced some basic principles concerning the thermal conductivity of solids in general, and gave an overview over the main features of this property for carbons and graphites. We refer to this chapter and to other recent review papers [135, 139, 140] for an introduction of this property in carbonaceous materials. We have seen that the lattice thermal conductivity results of graphites may be discussed using the Debye relation:

$$\kappa_g = \frac{1}{3} C v \ell_e \tag{6.116}$$

in the dominant phonon-approximation. This means that instead of considering the entire phonon spectrum, we introduce an average phonon frequency

which is proportional to the absolute temperature, and to which is associated an appropriate mean free path ℓ_e. C is the lattice specific heat per unit volume and v is an average phonon velocity, the velocity of sound. Despite its simplicity, relation [135] is useful for the discussion of most thermal conductivity results. For different samples of a given crystalline solid, since the specific heats and the phonon velocities are the same, the thermal conductivity is directly proportional to the phonon mean free path. This phonon mean free path depends essentially on the lattice perfection of the sample at low temperatures [135, 138].

Specific-heat measurements are now available for CNs. Hone et al. [141] reported on the results of measurements performed on SWNT ropes in the temperature range $2 < T < 300\,\mathrm{K}$. Later on, Lasjaunias et al. [142] presented experimental data pertaining to the low-temperature specific heat of SWNT bundles. These results extended for the first time the specific heat data to ultra-low temperatures (down to about 100 mK) showing clearly a T^3 dependence in the lowest temperature range. This temperature dependence, characteristic of a three-dimensional system, which was ascribed to inter-tube interaction, does not reflect the behavior expected from an individual one-dimensional SWNT.

At the lowest temperatures, when phonon-phonon umklapp processes are frozen out due to the decrease in phonon density and phonon wave number, crystallite or the sample boundaries are the main phonon scatterers and the phonon mean free path should then be temperature insensitive. So is the velocity of sound which is almost temperature insensitive at all temperatures. At low temperatures, the temperature dependence of the thermal conductivity should then follow that of the specific heat. Thus, the larger the crystallites or the sample-size the higher the thermal conductivity. Above the thermal conductivity maximum (Fig. 6.56 and Fig. 6.57), phonon scattering is mainly due to an intrinsic mechanism, phonon-phonon umklapp processes, and the thermal conductivity should thus be the same for different well-ordered samples of the same material. At intermediate temperatures, i.e. around the thermal conductivity maximum, scattering of phonons by point defects (small scale defects) is the dominant scattering process. The position and the magnitude of the thermal-conductivity maximum will thus depend on the competition between the various scattering processes (boundary, point defect, phonon, etc). So, for different samples of the same material, the position and magnitude of the maximum will depend on the point defects and the in-plane coherence length, L_a, since phonon-phonon interactions are assumed to be the same [135]. This will have an important bearing on the discussion of the experimental results, as discussed below.

Since the main mechanism responsible for heat flow in carbons, including MWNTs, is via the lattice waves, we should expect the same general trends in these materials. Indeed, while for different carbons the electronic structure might be quite different leading to various types of electronic conductions, metallic, semimetallic or semiconducting, this is not the case for

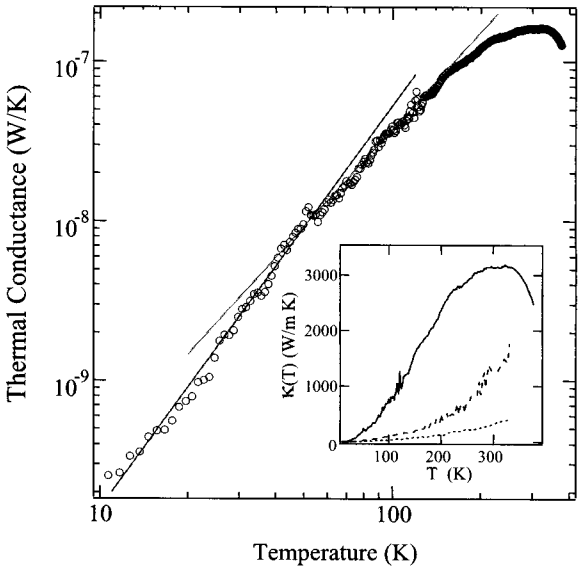

Fig. 6.57. Log-log representation of the temperature variation of the thermal conductance of an individual MWNT of diameter 14 nm. The *solid lines* represent the linear fits with slopes 2.5 and 2.0 respectively for different temperature range. Inset: Temperature variation of the thermal conductivity of an individual MWNT (*solid curve*), and a bundle of diameters 80 nm (*broken curve*) and 200 nm (*dotted curve*) respectively. Adapted from [136] (by courtesy of P. Kim)

phonon transport. If we exclude phonon quantization in nanosystems, the phonon spectrum should not differ widely from one carbon sample to another provided that they remain in the crystalline state. It is only the phonon mean free path which will differ since it is very sensitive to lattice defects [135,138].

The first thermal-conductivity data reported for nanotubes were performed by Hone et al. [137] on as-grown NT bundles. They estimated a room temperature thermal conductivity around $35\,\mathrm{W\,m^{-1}K^{-1}}$. This low value is not unexpected for their samples since it includes contact resistances between nanotubes of undefined crystal perfection. Indeed, subsequent calculations by Berber et al. [143] predicted much higher values for an ideal individual SWNT, of the order of a few $10^4\,\mathrm{W\,m^{-1}K^{-1}}$ around 100 K with a room temperature value close to $7000\,\mathrm{W\,m^{-1}K^{-1}}$. These values, which are superior to those of diamond and in-plane graphite (see Table 6.1) are more realistic, since they are close to that which might be expected from a perfect graphene sheet. As will be shown below, further experimental data have confirmed these views.

Since they were realized on an individual MWNT, the measurements performed by Kim et al. [136], though still subject to certain experimental uncertainties, lend themselves to the first reliable analysis allowing comparison with theoretical predictions. Using nanolithographic techniques, Kim et al.

designed a submicronic sample holder enabling the measurement of the thermal conductivity and thermoelectric power (cf. Sect. 6.9.3) of an individual MWNT of 14 nm diameter and a few micrometers in length. The temperature range $8\,\mathrm{K} < T < 370\,\mathrm{K}$ was investigated. The results are shown in Fig. 6.57. One may see from Fig. 6.57 that the estimated room temperature thermal conductivity lies around $3000\,\mathrm{W\,m^{-1}K^{-1}}$, with a peak around 320 K. Moreover, Kim et al. estimated from their data a phonon mean free path of the order of 500 nm, at low temperatures.

Although the high thermal-conductivity values obtained by Kim et al. [136] are not surprising, they are not consistent with the position of the maximum observed if we compare their data to those relative to other graphitic systems. In these systems, a low-temperature mean free path around 500 nm, due to boundary scattering, would indeed lead to a thermal conductivity maximum around room temperature, but with a value 3 to 4 times lower than that observed for the MWNT investigated [135]. This discrepancy could be attributed to a different thermal behavior of NTs with respect to bulk graphitic systems. While this is probably true for SWNTs, it is not likely that MWNTs would exhibit a different qualitative behavior from bulk graphitic systems. If this is indeed the case, one should then ascribe the discrepancy to some experimental uncertainties discussed by Kim et al. or, possibly, to the presence of heat losses which are not explicitly addressed in their paper [136]. Also, for the same boundary scattering length, a sample free of point defects might exhibit higher values around the maximum. Finally, the quasi-ballistic motion of phonons invoked by the authors and ascribed to the short length of the sample might lead to a qualitatively different behavior when compared to a sample of infinite length. Further experimental work will be needed to determine the reason for this apparent discrepancy.

6.9.3 Thermoelectric Power

Contrary to the case of the thermal conductivity, the interpretation of the thermoelectric power (TEP) results for most known solids is a rather delicate task. Indeed, except for the case of typical semiconductors such as germanium or silicon, the interpretation of this property for most solids is hardly convincing. This is particularly true for the case of carbons and graphites [135].

The TEP or Seebeck coefficient, S, is the potential difference generated by an applied unit temperature difference across an electrical conductor. The diffusion thermoelectric power is due to the diffusion of charge carriers from hot to cold caused by the redistribution of their energies caused by the temperature gradient. The charge carriers accumulating at the cold end of the sample give rise to the thermoelectric voltage. This potential difference tends to counterbalance the flow of diffusing carriers until a steady state is reached. Another mechanism, known as the phonon-drag thermoelectric power, consists in a transfer of momentum from the out-of-balance phonon system to the electron system under certain conditions (cf. below). This results in a

drag on the charge carriers which causes an additional electronic drift. An electric field is generated to counterbalance this extra electronic motion. For a given group of charge carriers, the general expression for the diffusion TEP is given by the Mott formula

$$S_d = \frac{\pi^2 k_B^2}{3q} T \left[\frac{\partial \ln \sigma}{\partial \varepsilon} \right]_{E_F}$$

where E_F is the Fermi energy and σ the electrical conductivity. The derivatives is taken at the Fermi level. When, as is the case for HOPG, there is more than one type of carrier, the total thermoelectric power is obtained by considering the different groups of carriers with partial thermoelectric powers that contribute to the total thermoelectric power as electromotive forces in parallel [135, 138].

Hone et al. [144] have reported on the temperature variation of the TEP of SWNTs bundles in the temperature range 4.2 K $< T <$ 300 K. They have also measured the electrical resistivity of these bundles in the same temperature range. The three samples investigated, two pristine and one sintered, exhibited the same qualitative behavior and almost the same values (Fig. 6.58). The thermoelectric power was found to be positive in the whole temperature range investigated. As may be seen from Fig. 6.58, it increases first linearly at low temperature then tends to saturate around 100 K to increase slowly again with temperature around 200 K. The room-temperature values, around 50 μV/K, are considerably higher than those observed for metallic samples (a few μV/K), but are comparable to those observed in semimetals. Oddly

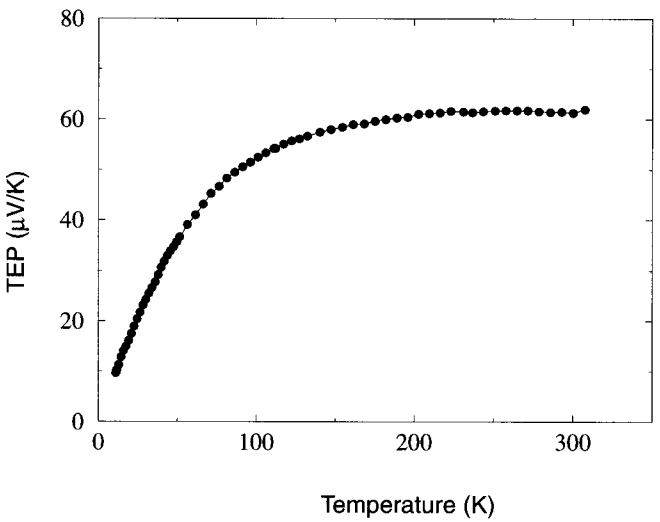

Fig. 6.58. Temperature variation of the TEP of a SWNT bundle. Adapted from [144] (by courtesy of J. Hone)

enough, the temperature variation looks more like that observed in graphite intercalation compounds (see for example [145]) than in the pristine material, though the room temperature value measured in SWNTs is about twice that reported for GICs.

In the case of SWNTs the earlier results of Hone et al. [144] have shown that the data are not consistent with those calculated from the known band structure which predicts much smaller values than those actually observed. Hone et al. suggest from their data that the predicted electron-hole symmetry of metallic nanotubes is broken when they are assembled into the form of ropes. Kim et al. [136] have also measured the temperature dependence of the TEP of the individual MWNT, whose thermal conductivity is reported in Fig. 6.57, from liquid helium temperatures up to room temperature (Fig. 6.59). At first sight, since the TEP is positive in the entire temperature range, one may deduce that it is generated by a majority of holes. The temperature variation is roughly linear and the high room temperature value observed ($80\,\mu V/K$) indicates that the Fermi energies are small, akin to what is observed for semimetallic systems. However, for a sound interpretation of the results, one needs to know at least the electronic band structure of the investigated sample. To illustrate the complexity of TEP analysis one should note that, if we exclude magnetic systems, there are two types of mechanisms for TEP generation: diffusion and phonon-drag. Besides, although the TEP is essentially sensitive to the Fermi energies, it is also dependent on the dominant scattering mechanism, but not on the magnitude of the scattering time. For the diffusion case, this means that it depends on the way the relaxation time depends on energy, i.e. the scattering parameter. It is worth noting too that

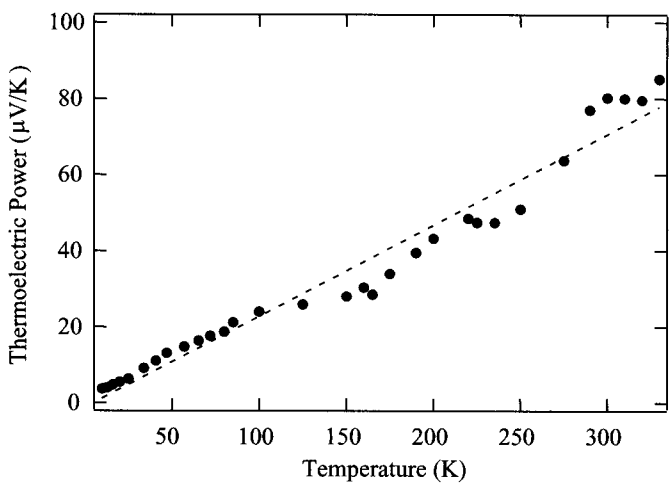

Fig. 6.59. Temperature variation of the thermoelectric power of the single MWNT which thermal conductivity is presented in Fig. 6.57. Adapted from [136] (by courtesy of P. Kim)

normal and umklapp electron-phonon scattering leads to TEPs of opposite signs. However, in most cases, electron-phonon umklapp scattering is unlikely to dominate the scene.

One important point to note is that, contrary to 3D systems, where the phonon-drag contribution generally shows up at low temperatures, in low-dimensional systems, whether 2D or 1D, this contribution might be dominant at all temperatures. Cantrell and Butcher [146, 147] have shown that this is the case for a 2D electron gas coupled to 3D phonons. Piraux et al. [148] have suggested independently that for first stages graphite acceptor intercalation compounds, which are typical 2D hole gases, the thermoelectric power is most probably dominated by a phonon-drag contribution up to room temperature with a negligible diffusion contribution [145]. More recently, Vavro et al. [149] have adapted the Cantrell-Butcher 2D model to a 1D electron gas interacting with 1D phonons to the case of p-doped SWNT and attributed the unusual behavior of the thermoelectric power they observed to 1D phonon-drag.

More generally, the phonon-drag contributions invoked from time to time can be justified using a naive physical picture. Phonon-drag shows up when the phonons which are allowed to interact with electrons, the drag phonons as opposed to the thermal phonons [145], have larger relaxation times for all other interactions, i.e. phonon-phonon, phonon-defects, etc. Note that the drag phonons are not necessarily those which dominate the scene at a given temperature and which carry most of the heat, i.e. those we call here the thermal phonons. The drag phonons are, in the case of semimetals and semiconductors, restricted to lower energies determined by energy and momentum conservation requirements [145]. For semimetallic systems with tiny Fermi surfaces like HOPG, we have pointed out [150] that the phonon-phonon interactions are very weak, even around room temperature, leading to unusually large phonon-phonon relaxation times. Moreover, because of the low energies of the drag phonons they are hardly scattered effectively by point defects (Raleigh scattering). This means that the probability for phonons to interact with electrons is larger than that of interacting with other phonons or point defects. Thus, in the absence of large-scale defects, we are in an ideal situation to observe large phonon-drag effects at all temperatures in semimetallic systems such as HOPG and MWNTs.

All this shows clearly that, contrary to the thermal conductivity, the interpretation of thermoelectric effects involves the knowledge of many physical parameters that are not always at hand. Also, since it is dependent on the details of the electronic structure and on the phonon spectrum, one expects that the TEP of SWNTs and MWNTs should differ since their electronic structures are quite different.

6.9.4 Measurement Techniques

There are specific problems associated with the measurement of the transport properties of macroscopic samples of large ratios of length to cross-section,

such as carbon fibers with diameters of the order of 10 μm, which are not encountered in bulk materials. It is obvious that these problems should be even more pronounced for the measurements on individual nanotubes where samples are of submicron size and are quite difficult to handle. The case of electrical resistivity has been discussed in previous sections, and we shall briefly consider here the additional difficulties encountered when heat flow has to be controlled such as in thermal transport measurements. Since heat flows are more difficult to control than electrical currents, thermal conductivity measurements are time consuming and very delicate to perform. This was found to be particularly true for the case of carbon fibers [151] because of their small diameters ($\sim 10^{-5}$ m). The main reason is that it is difficult to make sure that the heat losses in the measuring system do not far exceed the thermal conductance of the samples measured; the thermal conductance being defined as the heat flow through the sample per unit temperature difference. Moreover, in order to be able to get an insight into the mechanisms of the thermal conductivity of the sample investigated, it is necessary to measure the temperature variation of this property over a wide temperature range on a single well-characterized material, as was done for a vapor deposited fiber [152]. These problems are exacerbated for the case of single CNs [136].

Also, the determination of the sample cross-section may introduce large uncertainties in the estimation of the absolute values of the conductivities. The data obtained are thus more accurate with regard to temperature variation than with regard to absolute magnitudes. Fortunately, for the physical interpretation of the experimental results it is more important to know the temperature variation than the absolute values. These problems are not met in thermoelectric power measurements, since the knowledge of the samples cross-sections is not needed to calculate this transport coefficient. The measurement of samples of submicronic sizes requires a miniaturization of the experimental system, which may in some instances attain a high degree of sophistication. This is particularly true for the case of single CNs, where one has to deal with samples of a few nanometer diameter and about a micrometer length [153]. One has first to detect the sample, then apply to it contacts, which means, in a four-probe measurement, four metallic conductors, two for the injected heat current and two for measuring the resulting temperature difference. This requires the use of nanolithographic techniques [136,153]. Besides, one has to characterize the CN sample which is measured in order to determine its diameter and helicity if its electronic properties are to be known. This is particularly important for the case of the TEP, as mentioned above.

References

1. N. Ashcroft and D. Mermin: *Solid State Physics* (Saunders College, Philadelphia 1976)
2. A.A. Abrikosov: *Fundamentals of the theory of metals* (North-Holland, Amsterdam 1988)

3. Y. Imry: *Introduction to mesoscopic physics* (Oxford University Press, Oxford 2002)
4. S. Datta: *Electronic transport in mesoscopic systems* (Cambridge University Press, Cambridge 1997)
5. C.W.J. Beenakker and H. van Houten: *Solid State Physics* **44**, 1 (1991)
6. C.W.J. Beenakker: Rev. Mod. Phys. **69**, 731 (1997)
7. Ya.M. Blanter and M. Büttiker: Phys. Rep. **336**, 1 (2000)
8. B.L Altshuler and A.G. Aronov: In *Electron-electron interactions in disordered systems*, ed by A.L. Efros and M. Pollak (North-Holland, Amsterdam 1985)
9. H. Grabert and M.H. Devoret: *Single Charge Tunneling* (Plenum Press, New York 1992)
10. L.D. Landau and E.M. Lifshitz: *Statistical Physics, Part 2* (Pergamon Press, Oxford 1980)
11. V.J. Emery: *Highly conducting one-dimensional solids*, ed by J.T. Devreese, R.P. Evrard, V.E. van Doren (Plenum, New York 1979)
12. H.J. Schulz, G. Cuniberti, P. Pieri: In *Field theories for low-dimensional condensed matter systems*, ed by G. Morandi, P. Sodano, A. Tagliacozzo, and V. Tognetti (Springer, Berlin 2000)
13. T. Martin, G. Montambaux, J. Trân Thanh Vân (eds): *Correlated fermions and transport in mesoscopic systems* (Editions Frontières, Gif-sur-Yvette 1996)
14. I. Safi: Ann. Phys. Fr. **22**, 463 (1997)
15. M. Büttiker: J. Low Temp. Phys. **118**, 519 (2000)
16. C.L. Kane, and M.P.A. Fisher: Phys. Rev. B **46**, 15233 (1992)
17. C. Glattli, M. Sanquer, J. Trân Thanh Vân (eds): *Quantum physics at mesoscopic scale* (EDP Sciences, Les Ulis 2000)
18. E. Akkermans and G. Montambaux: *Physique Mésoscopique des électrons et des photons* (EDP Sciences/CNRS-Interéditions, Les Ulis 2004)
19. E. Abrahams, P.W. Anderson, D.C. Licciardello, T.V. Ramakrishnan: Phys. Rev. Lett. **42**, 673 (1979)
20. G. Montambaux: *Quantum Fluctuations, Proceedings of the Les Houches Summer School, Session LXIII*, ed by E. Giacobino et al. (Elsevier, Amsterdam 1996)
21. R.P. Feynman and A.R. Hibbs: *Quantum mechanics and path integrals* (McGraw-Hill, New-York 1965)
22. D.E. Khmelnitskii: Physica **126B**, 235 (1984)
23. S. Chakravarty and A. Schmid: Phys. Rep. **140**, 193 (1986)
24. P.A. Lee and T.V. Ramakrishnan: Rev. Mod. Phys. **57**, 287 (1985)
25. G. Bergmann: Phys. Rep. **107**, 1 (1984)
26. D.Y. Sharvin and Y.V. Sharvin: JETP Lett. **34**, 272 (1981)
27. A.G. Aronov and Y.V. Sharvin: Rev. Mod. Phys. **59**, 755 (1987)
28. A. Bachtold et al.: Nature **397**, 673 (1999). C. Schönenberger, A. Bachtold, C. Strunk, J.P. Salvetat: Appl. Phys. A **69**, 283 (1999)
29. P.A. Lee, D. Stone, H. Fukuyama: Phys. Rev. B **35**, 1039 (1987)
30. B. Altshuler and B. Shklovskiĭ: Sov. Phys. JETP **64**, 127 (1986)
31. D. Mailly and M. Sanquer: Journal de physique I France **2**, 357 (1992)
32. Ya.M. Blanter and A.D. Mirlin: Phys. Rev. E **55**, 6514 (1997)
33. R. Saito, G. Dresselhaus, M.S. Dresselhaus: *Physical Properties of Carbon Nanotubes* (Imperial College Press, London 1998)
34. S. Roche and R. Saito: Phys. Rev. Lett. **87**, 246803 (2001)

35. F. Triozon, Ph. Lambin, S. Roche: Nanotechnology **16**, 230 (2005)
36. L. Chico, L.X. Benedict, S.G. Louie, M.L. Cohen: Phys. Rev. B **54**, 2600 (1996)
37. T. Ando, T. Nakanishi: J. Phys. Soc. of Japan **67**, 1704 (1998). T. Ando, T. Nakanishi, R. Saito: J. Phys. Soc. of Japan **67**, 2857 (1998)
38. H.J. Choi, J. Ihm, S.G. Louie, M.L. Cohen: Phys. Rev. Lett. **84**, 2917 (2000)
39. S. Latil, S. Roche, D. Mayou, J.C. Charlier: Phys. Rev. Lett. **92**, 256805 (2004)
40. J.C. Charlier, T.W. Ebbesen, Ph. Lambin: Phys. Rev. B. **53** 11108 (1996). V.H. Crespi, M.L. Cohen, A. Rubio: Phys. Rev. Lett. **79**, 2093 (1997)
41. L. Chico, V.H. Crespi, L.X. Benedict et al: Phys. Rev. Lett. **76**, 971 (1996). Ph. Lambin and V. Meunier: Appl. Phys. A **68**, 263 (1999)
42. J.W. Mintmire and C.T. White: Phys. Rev. Lett. **81**, 2506 (1998)
43. C.T. White and T.N. Todorov: Nature **393**, 240 (1998)
44. S. Roche, G. Dresselhaus, M.S. Dresselhaus, R. Saito: Phys. Rev. B. **62**, 16092 (2000)
45. F. Triozon, S. Roche, A. Rubio, D. Mayou: Phys. Rev. B **69**, 121410 (2004)
46. K. Liu, Ph. Avouris, R. Martel, W.K. Su: Phys. Rev. B **63**, 161404 (2002)
47. L. Balents and M.P.A. Fisher: Phys. Rev. B **55**, 11973 (1997)
48. C.L. Kane, E.J. Mele, R.S. Lee et al: Europhys. Lett. **41**, 683 (1998)
49. L. Yang and J. Han: Phys. Rev. Lett. **85**, 154 (2000)
50. Ji-Yong Park, S. Rosenblatt, Y. Yaish et al: Nano Letters **4**, 517 (2004)
51. H. Suzuura and T. Ando: Phys. Rev. B **65**, 235412 (2002)
52. V. Perebeinos, J. Tersoff and Ph. Avouris: Phys. Rev. Lett. **94**, 086802 (2005)
53. S. Roche, J. Jiang, F. Triozon, R. Saito: Phys. Rev. Lett. **95**, 076803 (2005)
54. M. Georghe, R. Gutierrez, A. Pecchia, A. di Carlo, G. Cuniberti: Europhys. Lett. **71**, 438 (2005). S. Roche, J. Jiang, F. Triozon, R. Saito: Phys. Rev. B **72**, 113410 (2005)
55. S. Roche, F. Triozon, A. Rubio, D. Mayou: Phys. Rev. B **64**, 121401 (2001); Phys. Lett. A. **285**, 94 (2001)
56. D.J. Thouless: J. Phys. C **6**, 249 (1973)
57. D.J. Thouless: Phys. Rev. Lett. **39**, 1167 (1977)
58. J.C. Charlier and J.P. Michenaud: Phys. Rev. Lett. **70** 1858 (1993). Ph. Lambin, J.C. Charlier, J.P. Michenaud: *Progress in fullerene research*, ed by H. Kuzmany, J. Fink, M. Mehring, S. Roth (World Scientific, Singapore 1994), pp 130
59. R. Saito, G. Dresselhaus, M.S. Dresselhaus: J. Appl. Phys. **73**, 494 (1993)
60. Ph. Lambin, V. Meunier, A. Rubio: Phys. Rev. B **62**, 5129 (2000)
61. Y-K. Kwon and D. Tománek: Phys. Rev. B **58**, 16001 (1998). Y. Miyamoto, S. Saito, D. Tománek: Phys. Rev. B **65**, 041402 (2001)
62. S. Sanvito, Y.K. Kwon, D. Tománek, C.J. Lambert: Phys. Rev. Lett. **84** 1974 (2000)
63. S. Frank, P. Poncharal, Z.L. Wang, W.A. de Heer: Science **280**, 1744 (1998). P. Poncharal, C. Berger, Z.L. Wang, W.A. de Heer: J. Phys. Chem. **106**, 12104 (2002). A. Urbina, I. Echeverría, A. Perez-Garrido et al: Phys. Rev. Lett. **90**, 106603 (2003)
64. V. Krstic, S. Blumentritt, J. Muster et al: Phys. Rev. B **67**, 041401 (2003)
65. B. Bourlon et al: Phys. Rev. Lett. **93**, 176806 (2004)
66. M.P. Anantram: Phys. Rev. B **62**, 4837 (2000)
67. J.J. Palacios, J. Pérez-Jiménez, E. Louis et al: Phys. Rev. Lett. **90**, 106801 (2003)

68. C.L. Kane, L. Balents, M.P.A. Fisher: Phys. Rev. Lett. **79**, 5086 (1997). R. Egger, A.O. Gogolin: Phys. Rev. Lett. **79**, 5082 (1997); Eur.Phys. J. B **3**, 281 (1998)
69. M. Bockrath, D.H. Cobden, J. Lu et al: Nature **397**, 598 (1999)
70. R. Egger: Phys. Rev. Lett. **83**, 5547 (1999)
71. S. Eggert: Phys. Rev. Lett. **84**, 4413 (2000).
72. J. Lee et al: Phys. Rev. Lett. **83**, 166403 (2004)
73. P.J. de Pablo et al: Appl. Phys. Lett. **74**, 323 (1999)
74. V. Krstic, S. Roth, M. Burghard: Phys. Rev. B **62**, 16353 (2000)
75. B.Q. Wei, R. Vajtai, P.M. Ajayan: Appl. Phys. Lett. **79**, 1172 (2001)
76. A. Bezryadin, A.R. Verschueren, S.J. Tans, C. Dekker: Phys. Rev. Lett. **80**, 4036 (1998)
77. H. Hirayama, Y. Kawamoto, Y. Ohshima, K. Takayanagi: Appl. Phys. Lett. **79**, 1169 (2001)
78. K.B. Shelimov et al: Chem. Phys. Lett. **282**, 429 (1998)
79. L. Roschier et al: Appl. Phys. Lett. **75**, 728 (1999)
80. L. Kelvin: Phil. Mag. **46**, 82 (1898)
81. J. Tersoff: Appl. Phys. Lett. **74**, 2122 (1999)
82. S.B. Arnason, A. Rinzler, A.F. Hudspeth, A.F. Hebard: Appl. Phys. Lett. **75**, 2842 (1999)
83. M. Freitag, M. Radasavljevic, W. Clauss, A.T Johnson: Phys. Rev. B **62**, R2307 (2000)
84. P.J. de Pablo et al: Appl. Phys. Lett. **80**, 1462 (2002)
85. M. Brandbyge, J. Schiotz, M.R. Sorensen et al: Phys. Rev. B **52**, 8499 (1995)
86. T.W. Ebbesen et al: Nature **382**, 54 (1996)
87. A. Bachtold, M.S. Fuhrer, S. Plyasunovet et al: Phys. Rev. Lett. **84**, 6082 (2000)
88. M. Bockrath, D.H. Cobden, P. McEuen et al: Science **275**, 1922 (1997)
89. S.J. Tans, M.H. Devoret, H. Dai et al: Nature **386**, 474 (1997)
90. R.A. Jishi, M.S. Dresselhaus, G. Dresselhaus: Phys. Rev. B **48**, 11385 (1993)
91. M.S. Dresselhaus, G. Dresselhaus, P.C. Eklund: *Science of Fullerenes and Carbon Nanotubes* (Academic, San Diego 1996)
92. L. Balent and M.P.A. Fisher: Phys. Rev. B **55**, R11973 (1997)
93. This is the case in 1D systems at temperature below the Debye temperature as discussed by J. Appenzeller, E. Joselevich, W. Honlein: *Nanoelectronics and Information Technology – Advanced Electronic Materials and Novel Devices*, vol 19, ed by R. Waser (Wiley-VCH, 2003)
94. E. Fischer, H. Dai, A. Thess et al: Phys. Rev. B **55**, R4921 (1997)
95. R.S. Lee, H.J. Kim, J.E. Fischer et al: Phys. Rev. B **61**, 4526 (2000)
96. Z. Yao, C.L. Kane, C. Dekker: Phys. Rev. Lett. **84**, 2941 (2000)
97. A. Javey, J. Guo, M. Paulsson et al: Phys. Rev. Lett. **92**, 106804 (2004)
98. P.L. McEuen, M. Bockrath, D.H. Cobden et al: Phys. Rev. Lett. **83**, 5098 (1999)
99. L. Wenjie, M. Bockrath, D. Bozovic et al: Nature **411**, 665 (2001)
100. J. Kong, E. Yenilmez, T.W. Tombler et al: Phys. Rev. Lett. **87**, 106 801 (2001)
101. J. Appenzeller, R. Martel, Ph. Avouris et al: Appl. Phys. Lett. **78**, 3313 (2001)
102. P.G. Collins, M. Hersam, M. Arnold et al: Phys. Rev. Lett. **86** 3128 (2001)
103. J. Cumings, P.G. Collins, A. Zettl: Nature **406**, 586 (2000)
104. R. Martel, H.-S. Wong, K. Chan, Ph. Avouris: IEDM Tech. Dig., 320 (2001)

105. S. Wind, J. Appenzeller, R. Martel, et al: Appl. Phys. Lett. **80**, 3817 (2002)
106. A. Javey, H. Kim, M. Brink et al: Nature Materials **1**, 241 (2002)
107. A. Javey, J. Guo, Q. Wang et al: Nature **424**, 654 (2003)
108. R. Martel, T. Schmidt, H.R. Shea et al: Appl. Phys. Lett. **73**, 2447 (1998)
109. J. Appenzeller, J. Knoch, V. Derycke et al: Phys. Rev. Lett. **89**, 126801 (2002)
110. S.J. Tans, A. Verschueren, C. Dekker: Nature (London) **393**, 49 (1998)
111. H.T. Soh et al: Appl. Phys. Lett. **75**, 627 (1999)
112. V. Derycke, R. Martel, J. Appenzeller, Ph. Avouris: Appl. Phys. Lett. **80**, 2773 (2002)
113. R. Martel, V. Derycke, C. Lavoie et al: Phys. Rev. Lett. **87**, 256805 (2001)
114. In 1D, the thermal emission over the barrier is reduced to a simple Arrhenius expression with temperature. This is in contrast with the typical expression of thermionic emission over 3D barriers discussed in [118]
115. S. Heinze, J. Tersoff, R. Martel et al: Phys. Rev. Lett. **89**, 106801 (2002)
116. J. Misewich, R. Martel, J. Tsang, Ph. Avouris: Science **300**, 783 (2003)
117. J. Appenzeller, J. Knoch, R. Martel et al: IEEE Transactions on nanotechnology **1**, 184 (2002)
118. S.M. Sze: *Physics of Semiconductor Devices* (Wiley, New York 1981)
119. D. Stauffer and A. Aharony: *Introduction to percolation theory*, 2nd edn (Taylor and Francis, London 1994)
120. J.P. Clerc et al: Annales de Physique **8**, 1 (1983)
121. I. Balberg, N. Binebaum, N. Wagner: Phys. Rev. Lett. **52**, 1465 (1984)
122. S. Kirkpatrick: Rev. Mod. Phys. **45**, 574 (1973)
123. C.A. Grimes et al: Chem. Phys. Lett. **319**, 460 (2000). E. Kymakis et al: Synth Met **127**, 59 (2002). B.E. Kilbride et al: J. Appl. Phys. **92**, 4024 (2002)
124. J.M. Benoit et al: Synth. Met. **121**, 1215 (2001). J.M. Benoit, B. Corraze and O. Chauvet: Phys. Rev. B **65**, 241405(R) (2002)
125. J.N. Coleman et al: Phys Rev B **58**, R7492 (1998). J. Sandler et al: Polymer **40**, 5967 (1999); C. Stephan et al: J. Mater. Res **17**, 396 (2002)
126. N.F. Mott and E.A. Davis: *Electronic processes in non crystalline materials* (Clarendon Press, Oxford, 1979)
127. Y. Yosida and I. Oguro: J. Appl. Phys. **86**, 999 (1999). M.S. Fuhrer et al: Synth. Met. **103**, 2529 (1999). R. Gaal et al: Phys. Rev. B **61**, 7320 (2000)
128. P. Sheng, B. Abeles, Y. Arie: Phys. Rev. Lett. **31**, 44 (1973)
129. B. Shklovskiĭ and A.L. Efros: *Electronic properties of doped semiconductors* (Springer Verlag, Berlin 1984)
130. P. Sheng, E.K. Sichel, J.L. Gittleman: Phys. Rev. Lett **40**, 1197 (1978)
131. A.B. Kaiser et al: Synth Met **103**, 2547 (1999). G.T. Kim et al: Synth Met **117**, 123 (2001)
132. D. Van der Putten et al: Phys. Rev. Lett. **69**, 494 (1992) and references therein
133. S. Marianer and B. Shklovskiĭ: Phys. Rev. B **46**, 13100 (1992) and references therein
134. V.L. Nguyen, B.Z. Spivak, B. Shklovskiĭ: Sov. Phys. JETP **62**, 1021 (1985). U. Sivan, O. Entin Wohlman, Y. Imry: Phys. Rev. Lett. **60**, 1566 (1988)
135. J-P. Issi and B. Nysten: *Electrical and thermal transport properties in carbon fibers in Carbon Fibers*, ed by J-B. Donnet, S. Rebouillat, T. K. Wang, J. C. M. Peng (Marcel Dekker Inc., New-York 1998)
136. P. Kim, L. Shi, A. Majumdar, P.L. McEuen: Phys. Rev. Lett. **87**, 215502 (2001)
137. J. Hone, M. Whitney, C. Piskotti, A. Zettl: Phys. Rev. B **59**, R2514 (1999)

138. P. Delhaes, J-P. Issi, S. Bonnamy, P. Launois: Chapter 1, *Polymorphism and Structures of Carbons*, this volume
139. B.T. Kelly: *Physics of Graphite* (Applied Science Publishers, London 1981)
140. M.S. Dresselhaus, G. Dresselhaus, K. Sugihara et al: *Graphite Fibers and Filaments*, Springer Series in Materials Science 5 (Springer-Verlag, Berlin 1988)
141. J. Hone, B. Batlogg, Z. Benes et al: Science **289**, 1730 (2000)
142. J.C. Lasjaunias, K. Biljakovic, Z. Benes et al: Phys. Rev. B **65**, 113409 (2002)
143. S. Berber, Y-K. Kwon, D. Tomànek: Phys. Rev. Lett. **84**, 4613 (2000)
144. J. Hone, I. Ellwood, M. Muno et al: Phys. Rev. Lett. **80**, 1042 (1998)
145. J-P. Issi, Transport properies of metal chloride acceptor graphite intercalation compounds, *Graphite Intercalation Compounds II*, vol. 18, ed by H. Zabel and S.A. Solin (Springer Series in Materials Science, Springer Verlag, Berlin 1992)
146. D.G. Cantrell and P.N. Butcher: J. Phys. C **20**, 1985 (1987)
147. D.G. Cantrell and P.N. Butcher: J. Phys. C **20**, 1993 (1987)
148. L. Piraux, M. Kinany-Alaoui, J-P. Issi et al: Phys. Rev. B **38**, 4329 (1988)
149. J. Vavro, M.C. Llaguno, J.E. Fischer: Phys. Rev. Lett. **91**, 065503 (2003)
150. J-P. Issi: In *World of Carbon*, ed by P. Delhaes (Gordon and Breach, London 2001)
151. L. Piraux, J-P. Issi, P. Coopmans: Measurement **5**, 2 (1987)
152. L. Piraux, B. Nysten, A. Haquenne et al: Solid State Commun. **50**, 69 (1984)
153. J-P. Issi and J-C. Charlier: in *Science and technology of carbon nanotubes*, ed by K. Tanaka (Elsevier, London 1998)